Controlling the Electronic Interface Properties in Polymer-Fullerene Bulk-Heterojunction Solar Cells

Der Technischen Fakultät

der Friedrich-Alexander-Universität

Erlangen-Nürnberg

zur

Erlangung des Doktorgrades Dr. Ing.

vorgelegt von

Dipl.-Phys. Tobias STUBHAN

aus Ehingen (Donau)

Als Dissertation genehmigt
von der Technischen Fakultät
der Friedrich-Alexander-Universität Erlangen-Nürnberg
Tag der mündlichen Prüfung: 22.01.2014

Vorsitzende des Promotionsorgans: Prof. Dr. Marion MERKLEIN
1.Gutachter: Prof. Dr. Christoph J. BRABEC
2.Gutachter: Prof. Dr. Neal R. ARMSTRONG

"Make everything as simple as possible, but not simpler."

Albert Einstein

Zusammenfassung

Steuerung der elektronischen Kontakteigenschaften in organischen Polymer- Fulleren Solarzellen

Weltweit werden mehrere Dutzend Terawatt Elektrizität konsumiert. Wenn Solarenergie einen bedeutenden Teil zur Energieerzeugung der Zukunft beitragen soll, muss die Fabrikation von Solarmodulen von der heutigen Einzelfertigung im Gigawatt-Bereich auf Prozesse umgestellt werden, die Terawatt erlauben. Großflächiger, Rolle-zu-Rolle (R2R) Druck ermöglicht Solarzellenfertigung im Terawatt-Bereich.

Organische Photovoltaik ist eine der sehr vielversprechenden Technologien für die Produktion in Druckverfahren. Die 10 % Hürde wurde nach großen Fortschritten in der Effizienzsteigerung in den letzen Jahren genommen. Jetzt stehen hauptsächlich die Lösung von großtechnischen Produktions- und Haltbarkeitsproblemen im Fokus der Wissenschaft. Die Entwicklung der Zwischenschichten organischer Solarzellen, die sich zwischen aktiver Schicht und Elektrode befinden, ist von zentraler Bedeutung um diese Herausforderungen zu lösen. Die Zwischenschichten werden dazu genutzt die Effizienz zu maximieren, die Polarität der Bauteile zu definieren und um die Lebensdauer zu erhöhen. Abgesehen von ihrer Funktionalität, sollen die Zwischenschichten auch die Anforderung für die großflächige Produktion im Druckverfahren erfüllen. Metalloxide sind sehr vielversprechende Kandidaten um die Funktionalitäten bei den geforderten Prozessierungsbedingungen zu gewährleisten.

Diese Arbeit konzentriert sich auf Zinkoxid (ZnO) und dotiertes Zinkoxid als elektronenselektive Schicht. Die relativ niedrige Leitfähigkeit von intrinsischem Zinkoxid begrenzt die Schichtdicke auf einige wenige Dutzend Nanometer. Durch elektrische Simulationen konnte eine Leitfähigkeit in der Größenordnung von 10^{-3} S/cm abgeschätzt werden, die es ermöglicht Zwischenschichten von über 1 μm Dicke zu realisieren. Somit würden alle gewünschten Freiheiten in der Festlegung dieses Parameters erfüllt. Diese Leitfähigkeit kann durch die Dotierung von Zinkoxid mit Aluminium (Al) erreicht werden. In der vorliegenden Arbeit wird Al-dotiertes Zinkoxid (AZO) als Zwischenschicht aus einer Präkursorenlösung mit vergleichbarer Leistung wie intrinsisches Zinkoxid in dünnen Schichten eingeführt. Im Gegensatz zu ZnO, kann die Schichtdicke des AZO‘s erhöht werden, ohne die

Effizienz des Bauteils zu reduzieren.
Ein weiterer Teil der Arbeit umfasste die Verbesserung der Abscheidungsparameter, im Speziellen die Ausheiztemperatur des AZO's. Durch systematische Entwicklung der Präkursorenlösung konnte die Ausheiztemperatur auf unter 150 °C gesenkt werden. Dies ist entscheidend für die technologische Relevanz des Materials, da diese Temperaturen das Arbeiten mit günstigen Plastiksubstraten erlauben. Für diesen Präkursorenansatz konnten vollständig funktionale Zwischenschichten mit bis zu 680 nm Dicke erreicht werden. Dies verifiziert die Relevanz der simulierten Resultate. Dicke Zwischenschichten könnten sich ausser dem erweiterten, stabileren Prozessfenster auch positiv auf die Lebensdauer auswirken. Solche Lebensdauertests werden mit diesem vorgestellten Material ermöglicht.
Die Oberfläche einer elektronenselektiven Schicht spielt eine entscheidende Rolle bei der Kontaktformierung zur aktiven Schicht. Die Oberfläche einer AZO-Schicht wurde mit Hilfe von selbstorganisierenden Monoschichten (engl.: self-assembled monolayer (SAM)) manipuliert um deren Einfluss auf die Bauteileffizienz zu untersuchen. Die Leistung der resultierenden Bauteile variierte in Abhängigkeit der verwendeten SAM von 13 % bis 115 % der unmodifizierten Referenzsolarzelle. Dies demonstriert die Schlüsselrolle der Oberfläche von metalloxidischen Zwischenschichten.
Desweiteren wurden die entwickelten Elektronentransportschichten zusammen mit lösungsprozessierten Elektroden getestet. Die zum jetzigen Zeitpunkt bevorzugte transparente Elektrode Indiumzinnoxid (engl.: indium-tin-oxide (ITO)) ist teuer und brüchig. Beide Eigenschaften machen ITO für die zukünftige R2R Produktion auf flexiblen Substraten uninteressant. Silbernanodrähte sind aussichtsreiche Kandidaten als Ersatz für ITO. Die Silbernanodrähte (engl.: silver nanowire (AgNW)) sind lösungsprozessierbar, benötigen nur niedrige Temperaturen und sind zudem flexibel. AgNW's formieren ein Netzwerk mit einer recht rauhen Morphologie und müssen daher mit einer Zwischenschicht gefüllt und geglättet werden. Die entwickelten Zwischenschichten, ZnO und AZO, konnten hierzu erfolgreich eingesetzt werden. Es wurden vollständig funktionale Solarzellen mit 2,7 % Effizienz und über 60 % Füllfaktor demonstriert. Besonders der hohe Füllfaktor ist Ausdruck der exzellenten elektrischen Funktionalität der lösungsprozessierten, transparenten Kathode. Dieser Teil der Arbeit war ein erster Schritt zu vollständig lösungsprozessierten und halbtransparenten Solarzellen, die später in der Arbeitsgruppe realisiert wurden [1, 2].
Für Solarzellen in normaler Architektur werden für gewöhnlich instabile Metalle

mit niedriger Austrittsarbeit als Kathode eingesetzt. Dies limitiert die Lebensdauer der Bauelemente. Ein Ansatz hin zu stabilieren Solarzellen ist der Einsatz von Metalloxiden zusammen mit stabilen Metallen mit hoher Austrittsarbeit als Kathode. Die im vorherigen untersuchten Präkursoren für AZO zeigten keine Funktionalität, wenn sie auf der aktiven Schicht in der normalen Architektur eingesetzt wurden. Daher wurde eine AZO Nanopartikeldispersion entwickelt, deren Schichten vergleichbare elektrische Parameter zu den vorherigen Präkursoren bei nur 80 °C Ausheiztemperatur erreichen. Die Nanopartikeldispersion ermöglicht den Einsatz von AZO Elektronentransportschichten sogar auf vorher abgeschiedenen aktiven Schichten ohne die Morphologie zu verändern oder die sensitiven Materialien zu beschädigen. AZO Nanopartikel (NP) sind zusammen mit stabilem Silber ein vergleichbarer Ersatz zu instabilem Kalzium als Kathode.

Auf der Seite der Lochtransportschichten wird typischerweise das organische PEDOT:PSS eingesetzt. Dieses Material ist jedoch hygroskopisch und sauer, wodurch es als Quelle für die Degradation der Bauteile identifiziert wurde. Übergangsmetalloxide werden in dieser Arbeit als Kandidaten mit intrinsisch höherer Stabilität für den Ersatz von PEDOT:PSS untersucht.

Zu Beginn wurde Molybdänoxid aus einer Nanopartikeldispersion als Lochtransportschicht (engl.: hole transport layer (HTL)) in organischen Solarzellen eingebaut. Die Bauteile zeigten vergleichbare Effizienz zu den PEDOT:PSS Referenzen. Zudem konnte ein erhöhter Parallelwiderstand erreicht werden. Jedoch mussten die Molybdänoxidschichten mit einem Sauerstoffplasma behandelt werden, um funktionale Filme zu erhalten.

Die Erfahrungswerte aus der Arbeit mit Molybdänoxid wurden danach eingesetzt, um einen verbesserten Ansatz zu entwickeln. Auf Basis von Wolframoxid wurde eine Nanopartikeldispersion in einem alkohol-basierten Lösungsmittelsystem entwickelt. Die verwendeten Wolframoxid NP konnten sehr klein und mit sehr enger Größenverteilung synthetisiert werden. Dies ermöglichte glatte Filme, die nur 80 °C Ausheiztemperatur und kein Sauerstoffplasma für funktionale Filme benötigten. Diese Dispersion kann selbst in der invertierten Struktur auf der aktiven Schicht eingesetzt werden.

Auf diesem Weg konnten invertierte Solarzellen nur mit metalloxidischen Zwischenschichten mit einem kommerziellen aktiven Material mit hoher Effizienz von 6 % realisiert werden. Dieses Bauteil enthält somit nur intrinsisch stabile Materialien als Elektroden, die zudem einen Großteil der Anforderungen für die Herstellung von Solarzellen durch großflächige Druckverfahren erfüllen. Interessante,

vielversprechende Lebensdauerstudien mit den in dieser Arbeit entwickelten und untersuchten Metalloxiden sind somit möglich.

Publications

2013

- **T. Stubhan**, I. Litzov, N. Li, M. Salinas, M. Steidl, G. Sauer, K. Forberich, G. J. Matt, M. Halik and C. J. Brabec, "Overcoming interface losses in organic solar cells by applying low temperature, solution processed aluminum-doped zinc oxide electron extraction layers", J. Mater. Chem. A 1 (2013), 6004-6009.

- J. Min, H. Zhang, **T. Stubhan**, Y. Luponosov, M. Kraft, S. Ponomarenko, T. Ameri, U. Scherf, C. J. Brabec, "Combination of Al-doped ZnO and a conjugated polyelectrolyte interlayers for small molecule solution-processed solar cells with inverted structure", J. Mater. Chem. A 1 (2013), 11306-11311.

- P. Kubis, N. Li, **T. Stubhan**, F. Machui, G. J. Matt, M. M. Voigt, C. J. Brabec, "Patterning of organic photovoltaic modules by ultrafast laser", Prog. Photovolt: Res. Appl. (2013), DOI: 10.1002/pip.2421.

- F. Guo, X. Zhu, K. Forberich, J. Krantz, **T. Stubhan**, M. Salinas, M. Halik, S. Spallek, B. Butz, E. Spiecker, T. Ameri, N. Li, P. Kubis, D. M. Guldi, G. J. Matt, C. J. Brabec, "ITO-Free and fully solution-processed semitransparent organic solar cells with high fill factors", Adv. Ener. Mater. 3 (2013), 1062-1067.

2012

- **T. Stubhan**, N. Li, N. A. Luechinger, S. C. Halim, G. J. Matt and C. J. Brabec, "High fill factor polymer solar cells comprising a low temperature solution processed WO3 hole extraction layer", Adv. Energy Mater. 2 (2012), 1433-1438.

- **T. Stubhan**, J. Krantz, N. Li, F. Guo, I. Litzov, M. Steidl, M. Richter, G. J. Matt, C. J. Brabec, "High fill factor polymer solar cells comprising a transparent, low temperature solution processed doped metal oxide/metal nanowire composite electrode", Sol. Energy Mater. and Sol. Cells 107 (2012), 248-251.

- **T. Stubhan**, M. Salinas, A. Ebel, F. C. Krebs, A. Hirsch, M. Halik, and C. J. Brabec, "Increasing the fill factor of inverted P3HT:PCBM solar cells through surface modification of Al-doped ZnO via phosphonic acid-anchored C60 SAMs", Adv. Energy Mater. 2 (2012), 532535.

- H.-Q. Wang, **T. Stubhan**, Andres Osvet, I. Litzov, C. J. Brabec, "Up-conversion semiconducting MoO3:Yb/Er nanocomposites as buffer layer in organic solar cells", Sol. Energy Mater. Sol. Cells 105 (2012), 196201.

- N. Li, **T. Stubhan**, D. Baran, J. Min, H. Wang, T. Ameri, C. J. Brabec, "Design of the solution-processed intermediate layer by engineering for inverted organic multi junction solar cells", Adv. Energy Mater. 3 (2012), 301-307.

- J. Krantz, **T. Stubhan**, M. Richter, S. Spallek, I. Litzov, G. J. Matt, E. Spiecker, C. J. Brabec, "Spray-coated silver nanowires as top electrode layer in semitransparent P3HT:PCBM-based organic solar cell devices", Adv. Funct. Mater. 23 (2012), 1711-1717.

- N. Li, **T. Stubhan**, N. A. Luechinger, S. C. Halim, G. J. Matt, T. Ameri, C. J. Brabec, "Inverted structure organic photovoltaic devices employing a low temperature solution processed WO3 anode buffer layer", Org. Electron. 13 (2012), 2479-2484.

- D. Baran, A. Balan, **T. Stubhan**, T. Ameri, L. Toppare, C. J. Brabec, "Photovoltaic properties of benzotriazole containing alternating donoracceptor copolymers: Effect of alkyl chain length", Synthetic Metals 162 (2012), 2047-2051.

2011

- **T. Stubhan**, H. Oh, L. Pinna, J. Krantz, I. Litzov, C. J. Brabec, "Inverted organic solar cells using a solution processed aluminum-doped zinc oxide buffer layer", Org. Electron. 12 (2011), 15391543.

- **T. Stubhan**, T. Ameri, M. Salinas, J. Krantz, F. Machui, M. Halik and C. J. Brabec, "High shunt resistance in polymer solar cells comprising a MoO3 hole extraction layer processed from nanoparticle suspension", Appl. Phys. Lett. 98 (2011), 253308.

- H. Oh, J. Krantz, I. Litzov, **T. Stubhan**, L. Pinna, C. J. Brabec, "Comparison of various solgel derived metal oxide layers for inverted organic solar cells", Sol. Energy Mater. and Sol. Cells 95 (2011), 2194-2199.

- U. Hoyer, L. Pinna, T. Swonke, R. Auer, C. J. Brabec, **T. Stubhan**, N. Li, "Comparison of electroluminescence intensity and photocurrent of polymer based solar cells", Adv. Energy Mater. 1 (2011), 1097-1100.

Presentations

2013

- Invited oral presentation, EMN Spring Meeting, Orlando, USA, April, "Low temperature, solution processed n-type metal oxide interfaces for organic solar cells".
- Poster presentation, MRS Spring Meeting, San Francisco, USA, April, "Solution processed n-type metal oxide interfaces forming stable electrodes for normal and inverted organic solar cells".

2012

- Oral presentation, SPIE Optics+Photonics, San Diego, USA, August, "Low temperature solution-processed metal oxide buffer layers fulfilling large area production requirements".
- Oral presentation, DFG Workshop, W*ü*rzburg, September, "Low temperature, solution processed metal oxide buffer layers fulfilling large area production requirements".

2011

- Oral presentation, MRS Fall Meeting, Boston, USA, December, "Controlling the electronic interface properties in polymer solar cells".
- Oral presentation, DFG Summer School, W*ü*rzburg, June, "Controlling the electronic interface properties in polymer-fullerene bulk-heterojunction solar cells".

Acknowledgements - Danksagung

I would like to thank my supervisor Prof. Christoph J. Brabec and my co-supervisor Prof. Neal R. Armstrong for their great support and the creation of so many opportunities during my thesis. Special thanks for enabling my marvellous research stay at the University of Arizona.

I would like to thank all my colleagues and friends at I-MEET and ZAE for the great cooperation and atmosphere. A special "thank you" goes to Ning, Corina and Flo for making devices for me while i wasn't able to do it myself when I had a broken finger. Thank you Derya, Sena and Peter for organizing the group trips to Turkey and Slovakia (with car repair).

I wish to thank all the members of the Armstrong group at the University of Arizona for having and helping me during my research stay. Special thanks go to Clayton - it was good fun to hang out and work with you!

I thank Prof. Halik and Michael from the OMD group at the Institute of Polymer Materials (University of Erlangen-Nuremberg), Prof. Hirsch from the Institute for Organic Chemistry II (University of Erlangen-Nuremberg), Prof. Krebs from RisøNational Laboratory for Sustainable Energy (Technical University of Denmark) and Prof. Ratcliff from the Department of Chemistry and Biochemistry (University of Arizona) for the good and fruitful cooperation. Furthermore, I would like to thank Dr. K. Murakami from the Chair of Electron Devices (University of Erlangen-Nuremberg) and Dr. M. Rommel from Fraunhofer Institute for Integrated Systems and Device Technology for the c-AFM measurements.

Natürlich danke ich allen Freunden und meiner Familie für die gute Zeit. Insbesondere bei meinen Eltern möchte ich mich für die großartige und unermüdliche Unterstützung bedanken.

特别感谢我亲爱的宝贝！

Contents

List of Figures

List of Tables

Abbreviations

a-Si	**A**morphous **S**ilicon
AO	**A**tomic **O**rbitals
BHJ	**B**ulk **H**etero**j**unction
BOM	**B**alance **o**f **M**odules
CO_2	**C**arbon di**o**xide
CIGS	**C**opper **I**ndium **G**allium **S**elenide
DSC	**D**ifferential **S**canning **C**alorimetry
DSSC	**D**ye **S**ensitized **S**olar **C**ells
EEL	**E**lectron **E**xtraction **L**ayer
EQE	**E**xternal **Q**uantum **E**fficiency
ETL	**E**lectron **T**ransport **L**ayer
FF	**F**ill **F**actor
FHJ	**F**lat **H**etero**j**unction
GW	**G**iga**w**att
HEL	**H**ole **E**xtraction **L**ayer
HTL	**H**ole **T**ransport **L**ayer
ICT	**I**nteger **C**harge-**T**ransfer
IQE	**I**xternal **Q**uantum **E**fficiency
ITO	**I**ndium-**t**in-**o**xide
j_{SC}	**S**hort **C**ircuit Current Density
NP	**N**ano**p**article
OPV	**O**rganic **P**hoto**v**oltaics
OLED	**O**rganic **L**ight **E**mitting **D**iode
OSC	**O**rganic **S**olar **C**ells

P3HT	**P**oly(**3**-**h**exyl**t**hiophene)
PCBM	[6,6]-**P**henyl-**C**$_{61}$-**b**utyric-acid-**m**ethyl-ester
PC[70]BM	[6,6]-**P**henyl-**C**$_{\mathbf{71}}$-**b**utyric-acid-**m**ethyl-ester
PCE	**P**ower **C**onversion **E**fficiency
ppm	**P**arts **P**er **M**illion
PSC	**P**olymer **S**olar **C**ells
R$_P$	**P**arallel **R**esistance
R$_{Photoshunt}$	**P**hotoshunt **R**esistance
R$_S$	**S**eries **R**esistance
R$_{Shunt}$	**S**hunt **R**esistance ($\widehat{=}$ R$_P$)
RMS	**R**oot **M**ean **S**quare
Si	**S**ilicon
TGA	**T**hermo**g**ravimetric **A**nalysis
TW	**T**era**w**att

Physical Constants

Boltzmann constant	k_B	=	$1.381 * 10^{-23}$ J/K
Planck constant	h	=	$6.626 * 10^{-34}$ Js
Elementary charge	e	=	$1.602 * 10^{-19}$ C

Symbols

a	Distance	m
FF	Fill factor	%
I	Current	A or mA
j	Current density	mA/cm^2
N	Newton	kg*m/s^2
P	Power	W (Js^{-1})
PCE	Power conversion efficiency	%
R	Resistance	Ωcm^2
S	Siemens	A/V
T	Temperature	°C
V	Voltage	V or mV

α	absorption coefficient	1/cm
ϵ	dielectric constant	
η	efficiency	%
ν	frequency	1/s
Φ	work function	eV
σ	conductivity	S/cm

Chapter 1

Introduction

Today's energy generation is heavily dependent on fossil resources. These fossil fuels are limited which results in continuously increasing prices. The prices decreased recently after the fracking method made new resources accessible. But still, burning of conventional fuels creates great amounts of carbon dioxide (CO_2) which is known to promote global warming. Just this year, the keeling curve, displaying the CO_2 concentration in the atmosphere over time, approaches and certainly outruns the 400 parts per million (ppm) mark for the first time in human history (Figure 1.1).

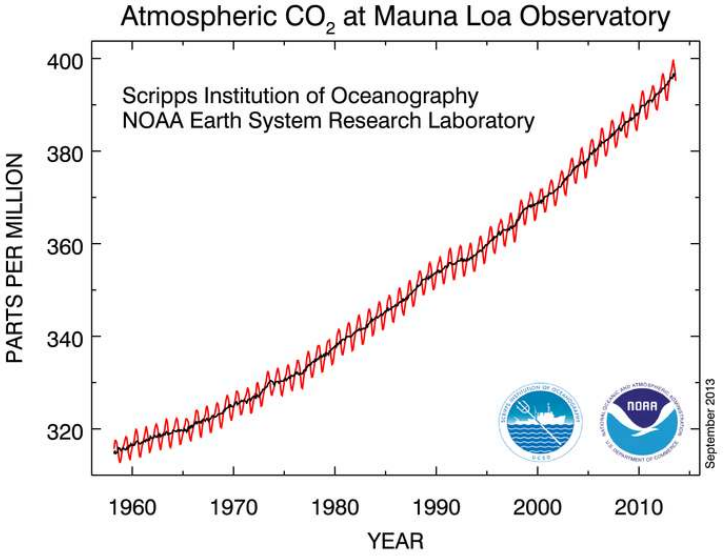

FIGURE 1.1: Carbon dioxide concentration in the atmosphere measured at Mauna Loa. [3]

In view of this development, the need for renewable and clean energies is rising. Among these, solar energy takes a special place as it bears the largest potential for cost reduction. The two main technologies on the market are based on inorganic materials like silicon (Si) and copper-indium-gallium-diselenide (CIGS). While being the most competitive options at the moment, both technologies have intrinsic drawbacks. CIGS needs large amounts of very rare and increasingly expensive materials like Indium. Silicon itself is the second most abundant element of the earth crust [22], but to get electronic grade silicon consumes extensive amounts of energy. On the search for alternatives, photovoltaic based on organic, often polymeric, materials is getting more and more attention. To a large extent, this is due to the huge increase in efficiency of these types of solar cells, rising this relatively young technology on a level with dye sensitized solar cells (DSSC) and amorphous silicon (a-Si) [23]. Apart from that, the raw materials are generally earth abundant and inexpensive. Furthermore, organic solar cells are capable of roll-to-roll production and even solution-processing without the need for high temperature and vacuum steps on flexible, cheap plastic substrates. This is a key production technology when the goal is to grow from nowadays gigawatt (GW) to future terawatt (TW) production. While contemporary production is a hardly scalable batch-to-batch process, roll-to-roll printing production is easily capable to be upscaled to TW. The world needs energy generation capacity of a couple of tens of TW electricity. If solar energy should have a notable share, it needs to be produced on the TW scale. But before organic or polymer solar cells can address larger markets, a number of processing and stability issues need to be solved. One of the main challenges is the design of reliable, environmental robust and easily processable charge extraction layers. These layers are typically processed between the semiconductor and the electrode, and, as suggested by their name, selectively extract one type of carrier while the other type of carrier is rejected. This work is focused on the processing and characterization of different solution processed metal oxides as charge extraction layer and relates their optoelectronic material properties to the solar cell performance.

Chapter 2

Theory of Plastic Solar Cells

2.1 Organic Semiconductors

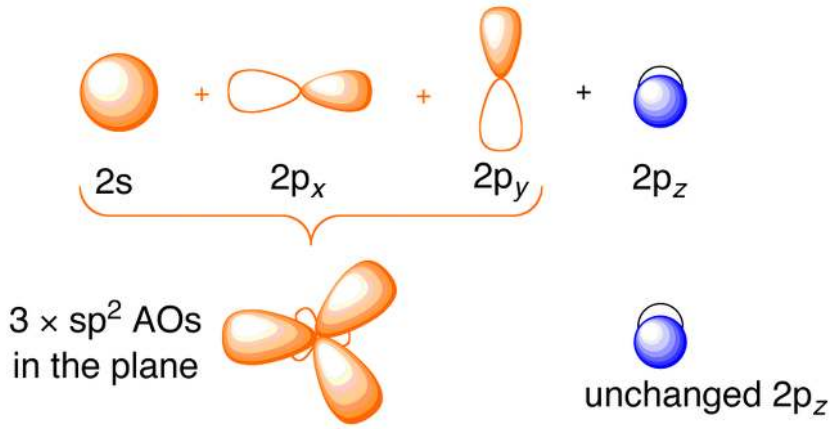

FIGURE 2.1: Atomic orbitals (AOs) involved in sp^2-hybridization. Reproduced from [4].

Organic semiconductors consist of carbon compounds. The carbon atom has 4 valence electrons that determine the behavior in chemical reactions. 2 electrons are in the 2s-orbital and 2 in 3 2p-orbitals. If the atom forms a chemical bond, sp^2-hybridization occurs. The 2s-orbital and 2 of the 3 3p-orbitals form 3 sp^2-orbitals. These orbitals have an asymmetric droplet-form and are aligned in one plane with 120° angle between each other. This process is depicted in Figure 2.1. The sp^2-hybridized orbitals form either a covalent bond between carbon atoms (σ -bonds) or to hydrogen which is shown for the example of an ethene (C_2H_4) molecule in Figure 2.2. The remaining p_z-orbitals of the carbon atoms form additional π-bonds. As the π-bond is weaker than the σ-bond, the energetic level of the π-electrons is

closer to the vacuum level. Therefore the energy (or bandgap) between the lowest unoccupied molecular orbital (LUMO) and the highest occupied molecular orbital (HOMO) is narrower than for σ-only hydrocarbon molecules. The bandgap of such an unsaturated hydrocarbon is lower than for a saturated hydrocarbon. A typical bandgap is between 1.5 and 3 eV which makes the material a semiconductor that absorbs light with visible wavelengths [24].

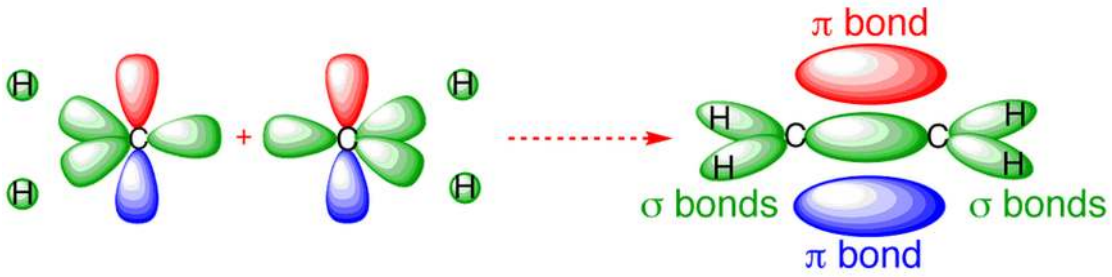

FIGURE 2.2: 2 carbon (C) and 4 hydrogen (H) atoms form an ethene molecule. sp^2-orbitals of the carbon atoms and the s-orbitals of the hydrogen atoms overlap to form covalent σ-bonds (green). The remaining p_z-orbitals of the carbon atoms form weaker bound π-bonds (red+blue). Reproduced from [4].

In contrast to inorganic semiconductors which are usually employed in crystalline form, organic semiconductors are mostly amorphous. Therefore no classical band structures occur, but localized densities of states. The fermi energy is the energy up to which all lower lying states are occupied by fermions (here: electrons) at T=0 K. Many classical methods of band theory of inorganic semiconductors can be applied to organic semiconductors with the analogues LUMO $\widehat{=}$ conduction band and HOMO $\widehat{=}$ valence band.

A further very important difference between organic and inorganic semiconductors (e.g. Si or GaAs $\epsilon \approx 12$ [24]) is the much lower dielectric constant (ϵ) in organic semiconductors (typically ≈ 3 [25]). As the coulomb attraction is proportional to $1/\epsilon$, it is stronger in organic materials than in inorganic ones. The coulomb attraction and the more localized confinement of electrons and holes to $\approx$ a molecule length, lead to heavily bond electron-hole pairs (Frenkel excitons). These excitons in organic semiconductors have typical binding energies between 0.4 to 1.4 eV [26]. Excitons in inorganic semiconductors have much lower binding energies and can be dissociated thermally. This process is very inefficient in organic semiconductors.

The charge carrier mobility of organic semiconductors is typically lower than in inorganic semiconductors. The carriers in organic materials have to travel through thermally activated hopping processes over defects or from one molecule to the

other. This is rather inefficient and limits organic devices to thicknesses in the order of a few hundred nanometers.

As the charges are heavily localized, organic semiconductors absorb in rather narrow bands. But the absorption coefficient in these areas is very strong (about 3 orders of magnitude larger than silicon) [27]. Therefore a few hundred nanometers of thickness is enough to absorb a large portion of the photons. Hereby organic semiconductor materials are still suitable materials for a solar cell and have the advantage to save material at the same time.

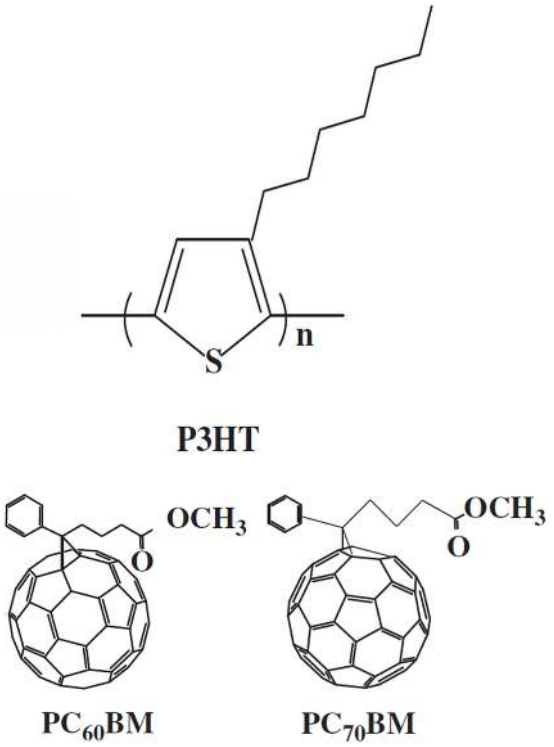

FIGURE 2.3: Chemical structures of important molecules and polymers. Adapted with permission from [5].

Organic semiconductors can be divided in two groups. Long-chained, conjugated polymers which contain many identical molecule units and compact small molecules. Examples for a small molecule used in this work are fullerene derivates as depicted in Figure 2.3. Here, either the solubilized versions of the C_{60} or C_{70} fullerene, namely [6,6]-Phenyl-C_{61}-butyric-acid-methyl-ester (PCBM) and [6,6]-Phenyl-C_{71}-butyric-acid-methyl-ester (PC[70]BM) are used. They are the standard acceptor materials in the field. In this work, only conjugated polymers were employed as donors for the photoactive layer. An important example for a conjugated polymer is poly(3-hexylthiophene-2,5-diyl) (P3HT) (also shown in

Figure 2.3). Apart from the active layer, conjugated polymers are employed as interface layers. The most commonly employed hole selective layer is poly(3,4-ethylendioxythiophene):poly(styrenesulfonate) (PEDOT:PSS).

2.2 Bulk Heterojunction

The absorber layer of a solar cell should convert photons in free charge carriers that can be collected at the respective electrodes. This process can be seperated in 5 steps with respective efficiencies: (i) Absorption of photons (η_{Abs}), (ii) generation and diffusion of excitons (η_{Diff}), (iii) separation of the exciton (η_{Sep}), (iv) charge carrier transport to the electrode (η_{Trans}) and (v) charge carrier extraction at the electrode (η_{Ext}) [5]. The external quantum efficiency (EQE) is described by the product of these five terms, while the internal quantum efficiency (IQE) is $IQE = \eta_{Diff} * \eta_{Sep} * \eta_{Trans} * \eta_{Ext}$. In other words, the EQE is the relation between incident photons to extracted charge carriers at the electrodes and the IQE relates absorbed photons to extracted charge carriers. In inorganic materials, the absorption of light leads directly to quasi-free charge carriers (see section 2.1). Absorbed photons create heavily bound excitons in organic materials. Efficient exciton separation takes place at the interface of two materials with sufficiently different electron affinity and ionization potential. The electron ends up at the material with higher electron affinity (acceptor), while the hole goes to the material with lower ionization potential (donor). The first organic solar cells employed a bilayer heterojunction as depicted in Figure 2.4 [28]. The generated excitons are separated at the interface of donor (D) and acceptor (A). A big limitation of the bilayer structure is, that the optical absorption depth ($\approx$ 300 nm) of usual organic materials is roughly a factor of 10 larger than the exciton diffusion length (less than 20 nm) [5]. An exciton needs to find an interface to get separated within the exciton diffusion length. Only the volume of the active layer that is less then +/- exciton diffusion length apart from the interface is contributing to free charge carrier production [6].

This limitation is largely overcome by the concept of the bulk heterojunction, an intimate mixture of donor and acceptor. The morphology of the bulk heterojunction has to be optimized to provide a maximum interface area between D and A, while still maintaining good charge carrier transport to the electrodes at the same time (see Figure 2.5) [5, 6].

The IQE of efficient organic solar cells is usually quite high [29]. Not absorbed or "too hot" photons are typically the largest loss mechanisms. Photons with less energy than the bandgaps of the active layer materials are not absorbed. Additionally, photons with larger energy than the bandgap generate excitons that

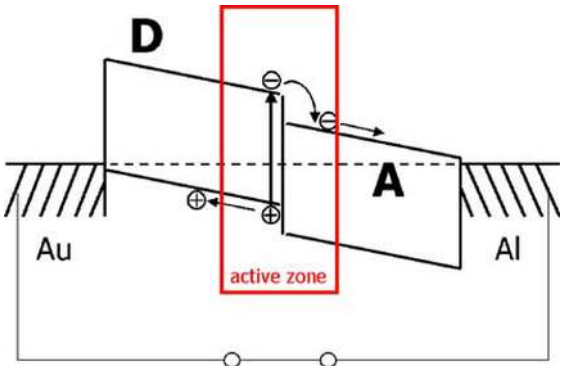

FIGURE 2.4: In bilayer devices, charge carriers can be dissociated at the donor (D) - acceptor (A) material heterojunction. Only excitons generated within diffusion distance to the interface can contribute to the photocurrent. Reproduced with permission from [6]. Copyright 2008, Springer.

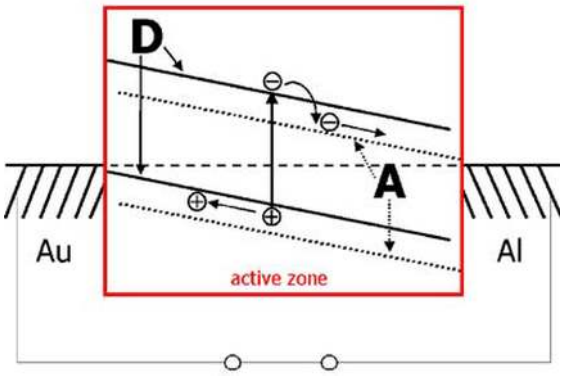

FIGURE 2.5: In bulk heterojunction devices, charge carriers can be dissociated throughout the volume of the active layer. Thus every absorbed photon in the active layer can potentially contribute to the photocurrent. Reproduced with permission from [6]. Copyright 2008, Springer.

loose their additional energy through dissipation (thermalization). For example, P3HT has a rather large bandgap which makes it only sensitive to about 50 % of the available photons in the spectrum of the sun [5]. The portion of absorbed photons can be increased through implementation of ternary absorber concepts [13]. Tandem architectures, which use two absorbing layers with complementary bandgaps, can reduce both loss mechanisms by increasing the number of absorbed photons and decreasing the thermalization losses at the same time [30].

2.3 Electrical Description of Solar Cells

The most important characterization method for solar cells is the measurement of the j-V characteristics. The main parameters of a solar cell can be derived from this measurement curve.

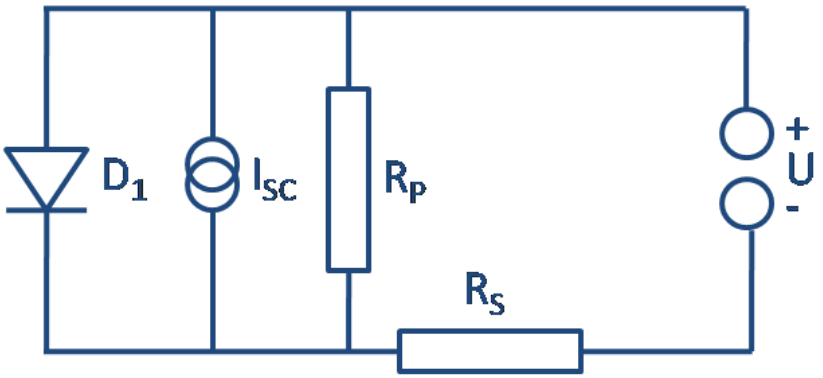

FIGURE 2.6: Replacement circuit of a solar cell. The ideal solar cell consists of the current source I_{SC} with the diode D_1 in parallel connection. The series resistance (R_S) and the parallel resistance (R_P) account for the losses in a real solar cell.

The electronic description of a solar cell can be made by the replacement circuit which is shown in Figure 2.6. An ideal solar cell can be described by a diode (D_1) with a current source (I_{SC}) in parallel connection. To account for the active area (A), the current density $j_{SC} = \frac{I_{SC}}{A}$ is introduced. Real solar cells have a number of loss mechanisms. The series resistance R_S is larger than 0 and the parallel resistance R_P is smaller than infinity. The replacement circuit shown in Figure 2.6 leads to following mathematical equation [31]:

$$j = j_{SC} - j_{D1}\left(exp\left(\frac{e(V+IR_S)}{k_BT}\right) - 1\right) - \left(\frac{V+IR_S}{R_P}\right) \tag{2.1}$$

The j_{SC} and the j_{D1} terms stand for an ideal solar cell. Figure 2.7 depicts a typical j-V curve of an illuminated and non-illuminated or "dark" solar cell in a linear plot and the "dark" curve in a logarithmic plot. The short circuit current density (j_{SC}) and the open circuit voltage (V_{OC}) are directly visible in the linear

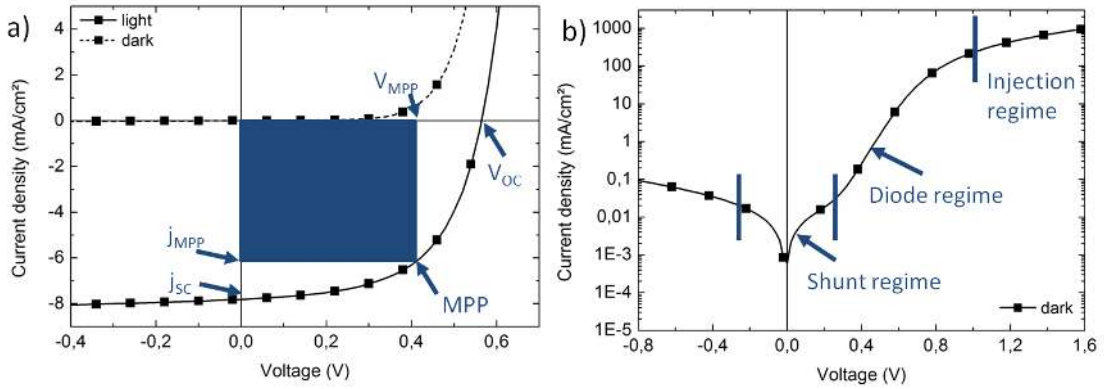

FIGURE 2.7: a) depicts an illuminated ("light") and a non-illuminated ("dark") j-V curve of a solar cell. The key parameters of the solar cell like V_{OC}, j_{SC}, V_{MPP} and j_{MPP} can be derived from the normal illuminated plot. b) The logarithmic plot visualizes the 3 regimes of the dark j-V curve (i) shunt regime around V=0, (ii) the diode regime and (iii) the injection regime at V>>V_{OC} [7].

plot. The fill factor (FF) and the power conversion efficiency (PCE, η) can be calculated using the maximum power point (MPP) and its corresponding voltage V_{MPP} and current density j_{MPP} as well as the power of the illumination (P_{Light}) with following equations:

$$FF = \frac{P_{MPP}}{P_{Max}} = \frac{V_{MPP} * j_{MPP}}{V_{OC} * j_{SC}} \tag{2.2}$$

$$\eta = \frac{P_{MPP}}{P_{light}} = \frac{FF * V_{OC} * j_{SC}}{P_{light}} \tag{2.3}$$

The logarithmic plot of the dark j-V characteristics from Figure 2.7 b) can be separated in 3 parts. (i) the symmetric region around V=0 that is dominated by the shunt or parallel resistance (shunt regime), (ii) the linear part that can be attributed to the diode (diode regime) with a slope proportional to the ideality factor and (iii) the region at high voltages which is the injection regime. The series resistance of the devices can be calculated from the inverse of the slope in forward direction at high voltages and the sum of series and parallel resistance can be calculated from the inverse of the slope around V=0. Usually, this is directly

used as R_P, as in most cases $R_S << R_P$ is valid. Low R_S and high R_P lead to high FF.

2.4 Interfaces in Organic Solar Cells

The interfaces between the active layer (i.e. the blend of donor and acceptor) and the electrode materials play a crucial role. Depending on the material system used, the main functions and impacts of interface materials are [32]:

- to maximize the open circuit voltage (V_{OC})
- to determine the polarity of the device - inverted or normal architecture
- to provide a selective contact for one charge carrier
- to enhance the stability of the device
- to influence the light distribution and propagation as an optical spacer

2.4.1 Open Circuit Voltage of Plastic Solar Cells

Without ohmic contacts at the interfaces, the open circuit voltage of organic solar cells is determined by the work function difference between the electrodes [33]. With ohmic contact to the interfaces, Brabec et al. found that the V_{OC} is determined by the difference of lowest unoccupied molecular orbital (LUMO) of the acceptor and the highest occupied molecular orbital (HOMO) of the donor [8]. Figure 2.8 a) plots the V_{OC} of solar cells with acceptors of different strengh versus the acceptor strength. The influence of the electrode work function is minor in that case (see Figure 2.8 b)). Similar results have been obtained by varying the HOMO of the donor [34].

The Integer Charge-Transfer (ICT) model is the most relevant theory to describe the contact formation of active layer and interface layer in this thesis [9]. The ICT model is valid for interfaces with negligible hybridization of molecular orbitals and the wave function of the substrate. This is typical for solution processed organic devices with contacts between conductive interfaces and organic semiconductors. The model defines two states: (i) the negative ICT state with energy E_{ICT-}, which is the energy gained when one electron is added to the organic material to reach the fully relaxed state, and vice versa (ii) the positive ICT state with energy E_{ICT+}. The ICT model describes 3 possible scenarios that are illustrated in Figure 2.9.

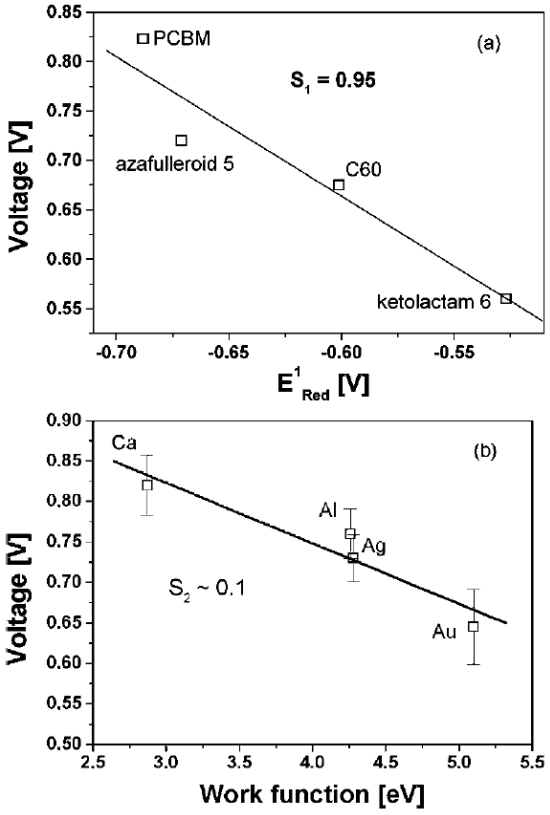

FIGURE 2.8: a) V_{OC} versus acceptor strength and b) V_{OC} versus negative electrode work function. The slopes S_1 and S_2 of the linear fits to the data are given inside the figures. Reproduced with permission from [8]. Copyright 2001, Wiley VCH.

- if the substrate workfunction is lower than the E_{ICT-} of the organic material, electrons will flow from substrate to organic material and the resulting workfunction is fermi level pinned to E_{ICT-} of the organic material.
- if the substrate workfunction is in between E_{ICT-} and E_{ICT+} of the organic material, no charge transfer happens and the resulting workfunction equals the substrate workfunction.
- if the substrate workfunction is higher than the E_{ICT+} of the organic material, electrons will flow from organic material to substrate and the resulting workfunction is fermi level pinned to E_{ICT+} of the organic material.

These three scenarios result in a contact alignment that is usually referred to as "Z of Zorro". An example is depicted in Figure 2.10.

A more general and detailed review on organic/organic and organic/metal interfaces is given in reference [9].

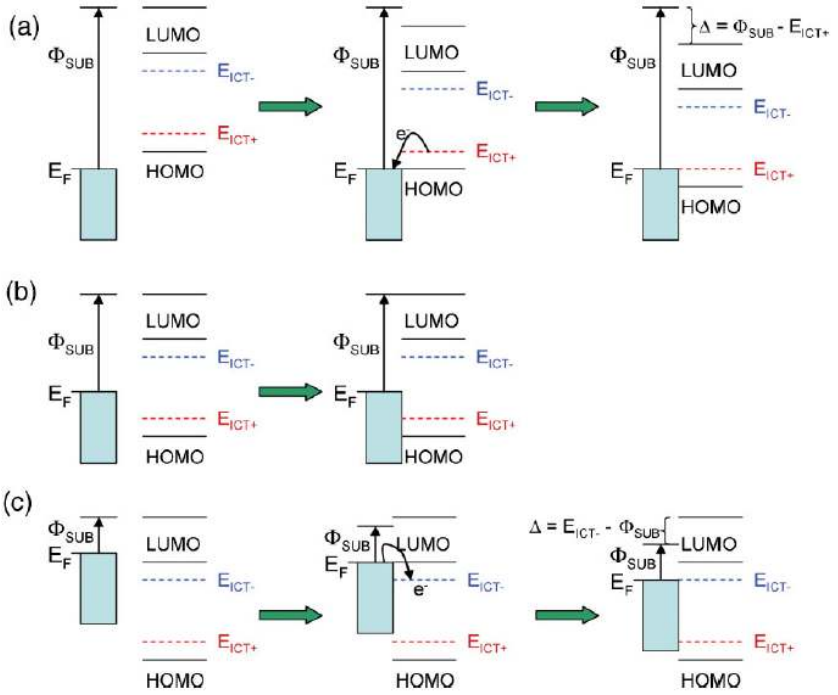

FIGURE 2.9: Schematic illustration of the evolution of the energy-level alignment when a pi-conjugated organic molecule or polymer is physisorbed on a substrate surface when a) $\Phi_{SUB} > E_{ICT+}$: Fermi-level pinning to a positive integer charge-transfer state, b) $E_{ICT-} < \Phi_{SUB} < E_{ICT+}$: vacuum level alignment, and c) $\Phi_{SUB} < E_{ICT-}$: Fermi-level pinning to a negative integer charge-transfer state. The charge-transfer-induced shift in vacuum level, D, is shown where applicable. Adapted with permission from [9]. Copyright 2009. Wiley VCH.

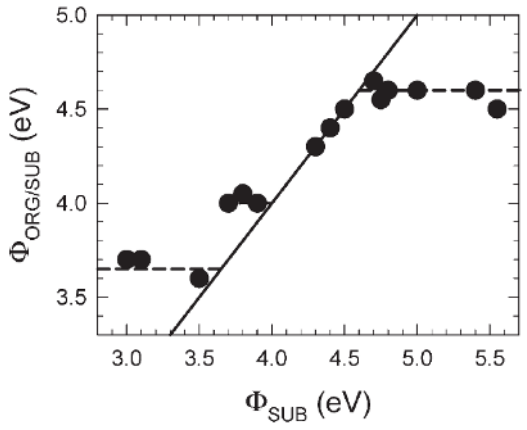

FIGURE 2.10: Dependence of the work function of molecule-coated substrates, $\Phi_{ORG/SUB}$, on the workfunction of bare substrates, Φ_{SUB}, for APFO-Green1 [78]. The solid line is added as a guide to the eye, illustrating the slope=1 dependence expected for vacuum level alignment. The dashed lines are added as guides to the eye, illustrating the slope=0 dependence expected for a Fermi-level pinned interface. Adapted with permission from [9]. Copyright 2009. Wiley VCH.

2.4.2 Impact of Interface Barriers on the Performance of Organic Solar Cells

Barriers occur if the energy levels of interface layers and active layer materials are not well matched. Tress et al. [10] investigated the influence of these barriers on the j-V characteristics of small molecule organic solar cells via systematic variation of donor and hole transport materials with different HOMO levels. In this way, injection and extraction barriers of 0 to 0.6 eV can be realized and their effect on the j-V characteristics for bilayer or flat heterojunction (FHJ) and bulk heterojunction (BHJ) devices can be studied. The layer stack of the investigated devices and the energy level alignment is shown in Figure 2.11.

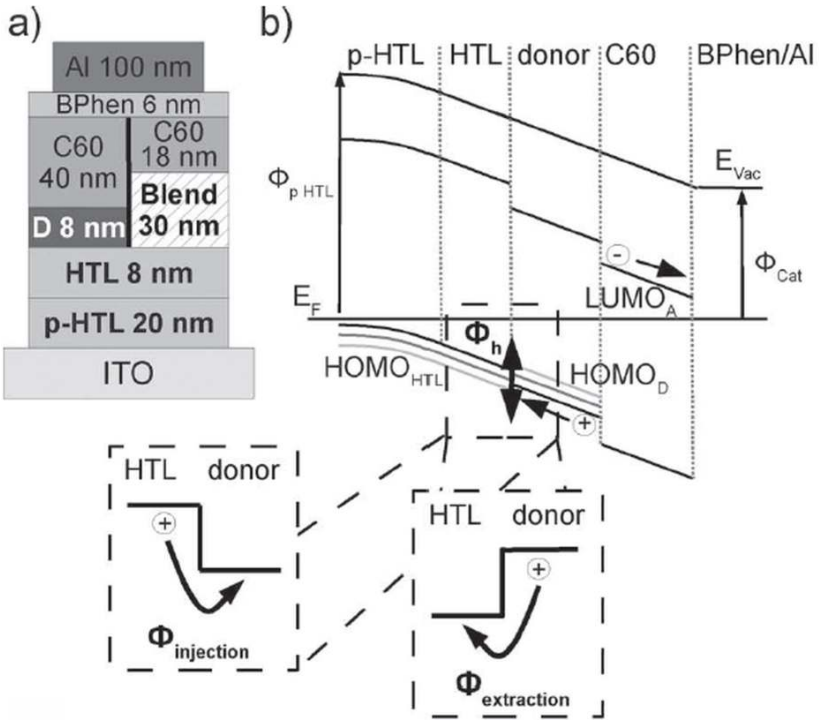

FIGURE 2.11: Layer stack with p-doped hole-transport layer (HTL) for ohmic contact to the ITO, intrinsic HTL, the active material stack, and BPhen-Al contact. The active material stack consists in the case of a FHJ of D (donor) C_{60} or in the case of a BHJ of a blend layer of donor: C_{60} with a mixing ratio of 1:1, followed by 18 nm C_{60}. b) Schematic band diagram of a FHJ with ϕ_h as hole-injection or extraction barrier. The type of ϕ (injection or extraction) depends on the combination of HTL and donor. Adapted with permission from [10]. Copyright 2011, Wiley VCH.

The V_{OC} of the different configurations for FHJ and BHJ devices is depicted in Figure 2.12. The important difference between FHJ and BHJ devices is that the V_{OC} for a FHJ is dominated by the HOMO of the donor and almost independent

of the HOMO of the HTL. If the HOMO of the HTL is higher than the HOMO of the donor of a BHJ, the HOMO of the HTL limits the V_{OC} due to an injection barrier. FHJ and BHJ behave differently as for a FHJ, electrons are "not" present at the donor/HTL interface. Thus electrons cannot recombine at the donor/HTL interface in case of an injection barrier.

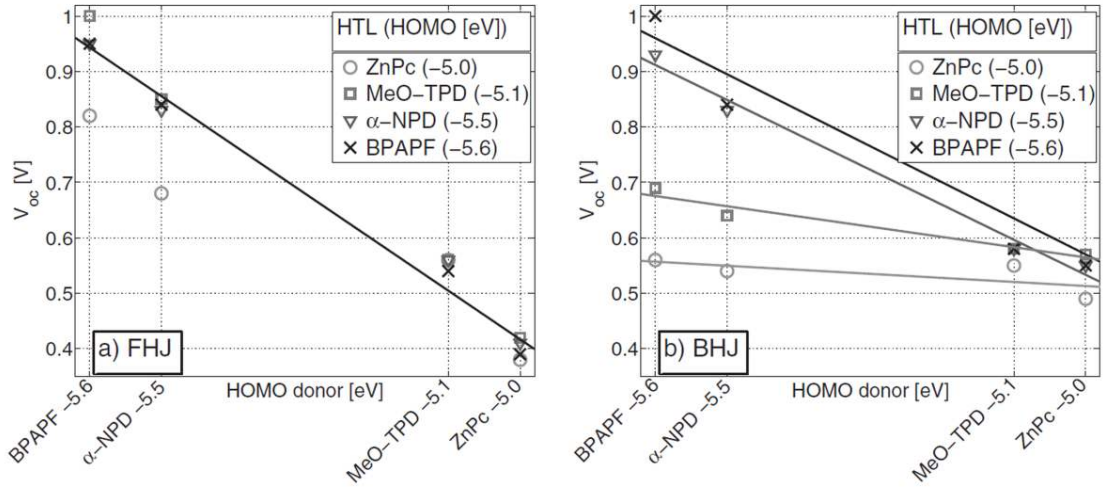

FIGURE 2.12: V_{OC} as a function of the HOMO of the donor material with different HTLs in a) FHJ and b) BHJ solar cells. Reproduced with permission from [10]. Copyright 2011, Wiley VCH.

Figure 2.13 shows the j-V characteristics for an extraction barrier with FHJ active layer. For extraction barriers, the qualitative behavior of the j-V characterisitics is similar for FHJ and BHJ devices (as underlined by the additional curve in Figure 2.13 for a BHJ). The typical s-shape in the j-V curves is observed. The kink is more pronounced for large barriers.

The main influence of an injection barrier for BHJ devices is on the V_{OC} (see Figure 2.14). The larger the barrier, the lower the V_{OC}. The shape of the curve does not change too much, but is shifted to lower V_{OC}'s.

Tress et al. conclude from this study, the accompanying simulations (see [10]) and other data sets of high performance devices that the ideal barrier for small molecule organic solar cells is a low extraction barrier of around 0.1 eV.

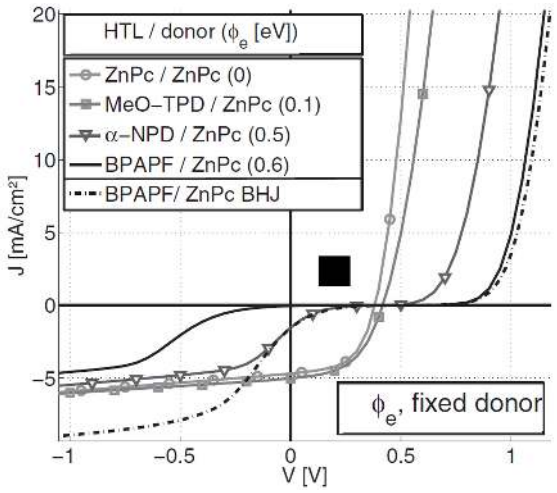

FIGURE 2.13: j-V characteristics with extraction barriers (ϕ_e) for FHJs with varying HTL and fixed donor ZnPc. The data for one BHJ (dash-dotted) is also shown and demonstrates the qualitative agreement of the shape of the j-V curves for extraction barriers for FHJ and BHJ devices. The larger the extraction barrier, the more prominent is the s-shape of the j-V characteristics. Adapted with permission from [10]. Copyright 2011, Wiley VCH.

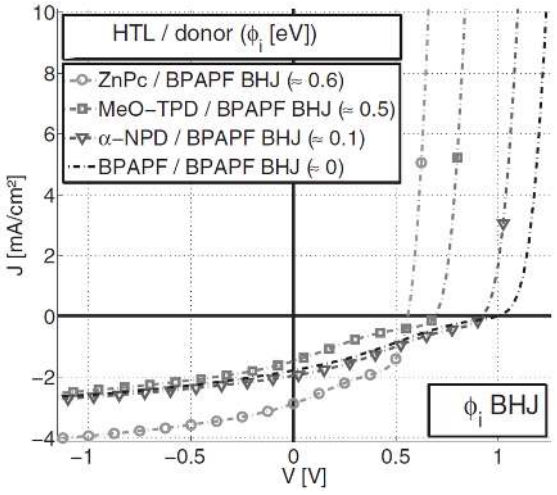

FIGURE 2.14: jV characteristics with injection barriers (ϕ_i) for the fixed donor BPAPF and varied HTL for BHJ solar cells. V_{OC} decreases with increasing injection barrier for a fixed donor. Adapted with permission from [10]. Copyright 2011, Wiley VCH.

2.4.3 Solution Processed Interface Materials

This work is focusing on solution processed polymer solar cells. Therefore, this section presents an overview over the most important solution processable interface materials. Numerous non-solution processed interface materials have been successfully used for organic solar cells and organic light emitting diodes (OLEDs) and there are serveral reviews in literature [32, 35–37].

2.4.3.1 Organic Materials

For polymer solar cells, PEDOT:PSS is the reference anode interface material that is commonly used in solution processed devices [38–41]. PEDOT:PSS forms a selective contact for holes, has a widely tunable conductivity and works with a large selection of donor polymers with high performance. It is solution deposited with excellent film forming properties and has a high transparency. Nevertheless, a lot of research is aiming to replace PEDOT:PSS because of stability issues. Since PEDOT:PSS is acidic (pH $\approx$ 1), byproducts of PEDOT or side reactions between the acid and the other solar cell materials can cause environmental degradation of the devices [42, 43]. The chemical structure of the PEDOT:PSS blend is depicted in Figure 2.15.

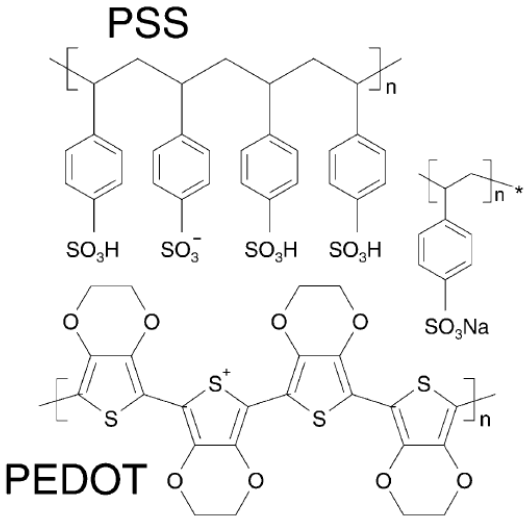

FIGURE 2.15: Chemical structure of the PEDOT:PSS blend. Adapted with permission from [11]. Copyright 2003, Elsevier.

Other solution processed organic materials used as (part of the) cathode are for example poly(ethylene oxide) (PEO) [44], water-soluble polyfluorene (WPF-6-oxy-F) [45] or polyoxyethylene tridecyl ether (PTE) [46].

2.4.3.2 Metal Oxides

The most widespread solution processed materials for n-type contacts in OPV are metal oxides like titanium oxide (TiO_X) [46–50] and zinc oxide (ZnO) [48, 51–56]. The most common issues with these intrinsic oxides are s-shapes in the j-V characteristics due to the poor conductivity, especially when the films are thick and not illuminated with UV light. First examples of organic solar cells employing doped metal oxides as charge transport layer were reported in literature [48, 57, 58]. The enhanced conductivity and charge carrier density of these materials could allow thicker interface layers, avoid s-shapes in the j-V characteristics and could improve contact formation to the metal.

Metal oxides can also form highly selective interface materials at the anode. In the beginning, these materials have been only deposited through vacuum processes. The most important ones are MoO_X [59, 60], VO_X [60] and WO_X [61, 62]. More recently solution processing from precursor or nanoparticle dispersions came into the research focus. A lot of approaches have been presented in literature for MoO_x [63–66], NiO_X [67–69], VO_X [70, 71] and WO_X [71–73]. Typical issues to solve are the low conductivity that requires very thin films or harsh deposition conditions, like high temperatures or the need for oxygen plasma treatments to achieve functional films.

2.4.3.3 Thin Modification Layers

Another group of interface materials are applied in thin semiconducting or insulating modification layers. The most important groups are self assembled monolayers (SAMs), conjugated polyelectrolytes (CPE), salts [12] and polyethlyenimines (PEI). These layers are typically applied in thicknesses of <=10 nm. Self assembled monolayers (SAM) with a permanent dipole moment [52] or a fullerene (C60) [54, 74] were reported in combination with metal oxides, transparent conducting oxides or metals. In case of the permanent dipole, the SAM layer has the functionality to fine-tune the work function of the interface material to guarantee a

well selective contact to the semiconductor. Fullerene SAMs were suggested to modify the surface of the metal oxide and to improve the charge carrier extraction. More recently, thin solution processed layers of conjugated polyelectrolytes (CPEs) [75–79] or polyethylenimines (PEI) [80] were as well reported to modify the interface properties of organic devices. Most often the improvements with these thin modification layers are only verified experimentally. Just few studies have been done so far on the origin of the improvement. Thin modification layers can often modify the work function as depicted in Figure 2.16 [12, 80], saturate defect states at the interface [81] or change the surface energy for different wetting properties [82]. Cathode modifications [80] as well as anode modifications were reported [83].

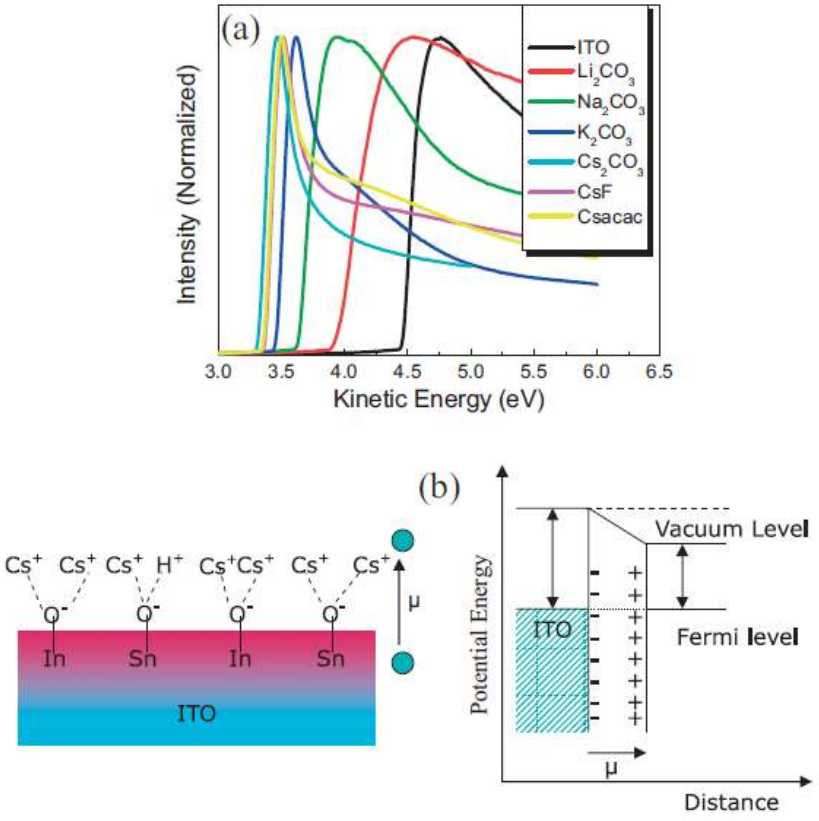

FIGURE 2.16: a) Evolution of secondary electron edge with different buffer layers on ITO, b) scheme for the formation of dipole layer on ITO and its effect on reducing the work function of ITO. Reproduced with permission from [12]. Copyright 2008, Wiley VCH.

2.4.4 Large Area Production Requirements for Interface Layers

After fast progress increasing efficiency of organic solar cells, the important 10 % hurdle has been taken [84], and even higher efficiencies of up to 15 % are becoming realistic by exploring tandem technologies.

Nevertheless, further tremendous efforts are required to develop the OPV technology towards industrial standards. One of the essential, remaining problems is to develop reliable and environmentally stable as well as mechanically robust interfaces. Today's high performance polymers, with only a few exceptions, only perform well in the thin film limit around 100 nm [85] and frequently suffer from a fill factor reduction upon increased film thickness. Either mobility limitations or a poor morphology in the thick film limit are the reasons for that [86, 87]. However, such thin active layers bear the risk of thin film defects, like e.g. shunts, negatively impacting yield and reliability of the production process [87]. A straightforward approach would be to develop polymers that also perform well in thick layers [87]. This is not only challenging from the chemical side, but also unwanted from the economical point of view, since thicker films require more of the rather expensive polymers. Other solutions need to be developed, since material expenses dominate the balance of modules for fast and large scale printing processes.

An alternative, but smart solution is the reengineering of the electrodes and electrode interface layers such that they provide the necessary reliability for the layer stack. Thick, stable and robust interface layers, deposited at low temperatures, encapsulating thin active layers are a viable route to achieve this. Considering the material properties of known interface layers, poly(3,4-ethylene dioxythiophene):(polystyrene sulfonic acid) (PEDOT:PSS) as the p-type side extraction layer meets most requirements. PEDOT:PSS has a widely tunable conductivity and is processed at low temperatures. The drawbacks of PEDOT:PSS are stability concerns, mainly due to the hygroscopic and acidic nature (see section 2.4.3.1). More stable alternatives for PEDOT:PSS are currently investigated. In the main resarch focus are transition metal oxides that will be addressed in chapter 5. This material class is still under development, mainly solving solution processing issues. Low conductive, intrinsic layers of these materials can be processed up to around 50 nm thickness without limiting device performance (see references of section 2.4.3.2).

On the n-type side, the most commonly employed ETL materials are TiO_X and ZnO. The problem setting is similar to the p-type side. Intrinsic TiO_X and ZnO show low conductivities and therefore are limited in the layer thickness. A viable path to overcome this restriction are doped metal oxides with enhanced conductivity. ZnO is the prototype material system for doping investigations. Puetz et al. used an Indium-doped ZnO nanoparticle solution to process EELs with up to 160 nm without great impact on series resistance (R_S) and fill factor (FF) [57].

The interface layer should be applicable on plastic substrates and even organic active layers. The application on plastic substrates restricts the temperatures that can be used to a maximum of 150 °C. If the interface layer should be used on top of previously deposited organic active layers or in tandem devices, additional limitations apply. A solvent with a low surface energy needs to ensure wet-ability and should not dissolve underlying layers. The necessary annealing temperature should be so low that the morphology of already deposited active layers is not influenced. A target temperature value is 80 °C. Furtermore the solution for the interface layer should not contain any components that damage the active layer materials [88]. The compatibility is especially critical for precursors with numerous initial components and reaction products. Therefore, and because of the low annealing temperatures, a nanoparticle dispersion is generally preferred over a precursor. If a precursor is not thoroughly annealed, the residual (organic) materials can be a degradation source for the device. Metal oxides are a very promising material group that have the potential to fulfill these requirements. Therefore metal oxides are in the focus of this work.

The desired properties for large area processable interface layers are summarized in the following list:

- Solution processable
- Intrinsically stable
- Low temperature processable
- Thick and robust
- Applicable on plastic substrates and on top of organic layers
- Nanoparticle dispersion

Adapted from Ref. [16] with permission from The Royal Society of Chemistry.

Chapter 3

Experimental Methods and Materials

3.1 Device Architectures and Sample Layout

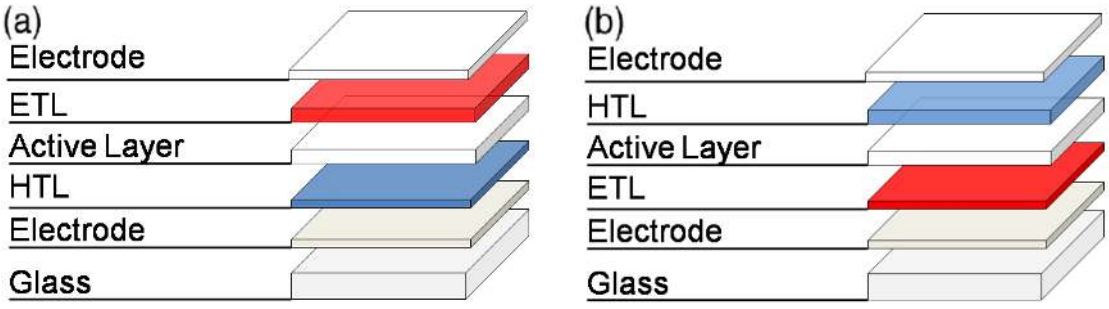

FIGURE 3.1: Typical layer stacks of polymer solar cells: (a) normal and (b) inverted architecture.

The solar cells in this thesis were processed with the layer stacks as depicted in 3.1. The active layer consists of the bulk heterojunction formed by donor and acceptor. The two different architectures are defined by the position of the interface layers. For the normal architecture, the electrons are extracted by the electron transport layer (ETL) on top of the active layer. The holes are extracted through the hole transport layer (HTL) below the active layer. The interface layers are switched for the inverted architecture. The electrodes on top and at the bottom are used for the lateral transportation of the charge carriers.

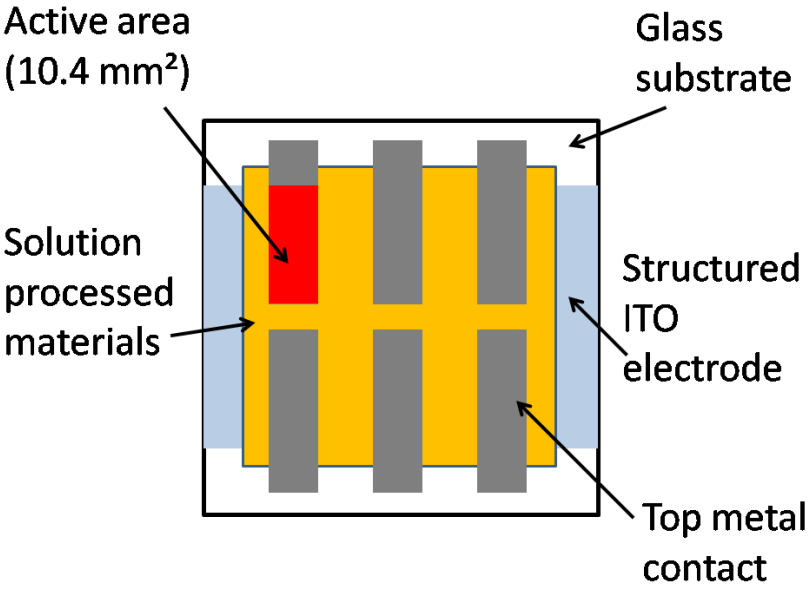

FIGURE 3.2: Sample layout.

The sample layout is shown in Figure 3.2. The solar cells were processed on glass substrates with pre-structured bottom ITO electrode. Afterwards, all solution-processed layers were deposited over the whole substrate area and structured before the top electrode deposition through a shadow mask via thermal evaporation. The overlap of top and bottom electrodes defined the active area. Each substrate had 6 devices.

3.2 Materials

3.2.1 Active Layer Materials

The donors used in this work are poly(3-hexylthiophene) (P3HT), poly[(4,4‘-bis(2-ethylhexyl)dithieno[3,2-b:2,3-d]silole)-2,6-diyl-alt-(4,7-bis(2-thienyl)-2,1,3-benzothiadiazole)-5,50-diyl] (Si-PCPDTBT) and a novel polymer GEN-2 from Merck. [6,6]-Phenyl-C_{61}-butyric-acid-methyl-ester (PCBM) and [6,6]-Phenyl-C_{71}-butyric-acid-methyl-ester (PC[70]BM) are the employed acceptors. The chemical structures of P3HT, PCBM and PC[70]BM are already shown in Figure 2.3. Si-PCPDTBT is depicted in Figure 3.3 and the structure of GEN-2 is not disclosed by the company.

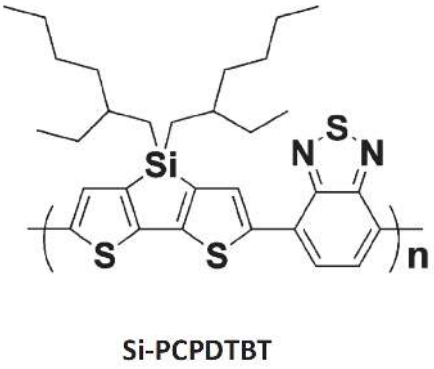

FIGURE 3.3: Chemical structure of Si-PCPDTBT. Adapted with permission from Ref. [13]. Copyright 2012, Wiley VCH.

3.2.2 Material Properties of the Investigated Metal Oxides

The most important materials for this thesis are zinc oxide (ZnO), molybdenum oxide (MoO_X) and tungsten oxide (WO_X). All these materials are semiconductors with wide band gaps of around 3 eV (ZnO $\approx$ 3.3 eV [89], $MoO_X \approx$ 3 eV [90] and WO_X from 2.6 to 3.26 eV [91]). Through the large band gaps, these materials are transparent for "visible" light and therefore suitable as window layers in solar cells.

All three materials are found to be n-type in their intrinsic form. ZnO is used as electron selective layer as the work function is typically around 4.3 eV (measured with Kelvin Probe in air) [55]. The energetic levels of MoO_X and WO_X are very deep. In ultra high vacuum, work functions deeper than 6 eV can be observed [63, 90]. When these films are exposed to air, the work functions quickly drop around 1 eV [63]. With such high work functions, these transition metal oxides form a hole selective contact to the HOMO of the polymers. All values heavily depend on the synthesis, deposition and annealing conditions.

There are two typical approaches for the solution processing of these materials i) from precursor or ii) from nanoparticle dispersion. For both approaches, the post-processing conditions after the film deposition are crucial. The deposited layer contains not only the metal oxide in the final state, but also amorphous compounds, organic ligands and solvent residuals. In Figure 3.4, the conversion of a precursor is depicted during the annealing process. The annealing temperature is critical for the postprocessing from a precursor solution. For a zincacetate based precursor, a typical precursor for (doped) ZnO, the differential scanning calorimetry (DSC) and thermogravimetric analysis (TGA) monitor the energy balance and

weight of the precursor during heating. In this way, the thermal conversion behavior of the material can be investigated. Around 450 °C are necessary for this precursor to reach the final converted state, when the weight reaches a constant value and the energy balance is 0. Critical temperatures for the processing of organic solar cells are much lower in the range from 80 to 150 °C. Therefore, the annealing temperatures and other postprocessing treatments are very important for the material properties of the metal oxides and are able to change important parameters like the conductivity by many orders of magnitude.

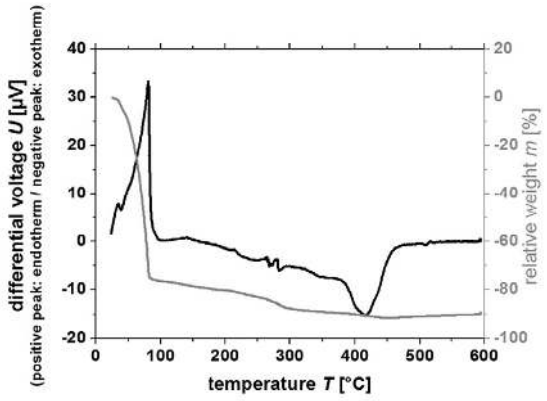

FIGURE 3.4: DSC-TGA curves of the calorimetric and gravimetric analysis during the sol-gel transition and formation of crystalline AZO in a temperature range from 0 to 600 °C for a zincacetate based precursor. Adapted with permission from [14]. Copyright 2012, Elsevier.

3.3 Experimental Methods

3.3.1 Deposition and Morphology

3.3.1.1 Doctor Blading

Most solution processed layers in this thesis have been deposited through doctor blading. The solution containing the material to be deposited, is applied in the slit between the substrate and the blade. Then the blade moves with a defined speed over the substrate to apply the wet film. After drying, the film of the material finds itself on the substrate. The thickness of the film, which can be only a couple of nm thick, is mainly controlled by the speed of the blade and the solid content in the solution. The machines used during this thesis were obtained from Zehntner. Figure 3.5 depicts a device from Erichsen while blading a polymer solution.

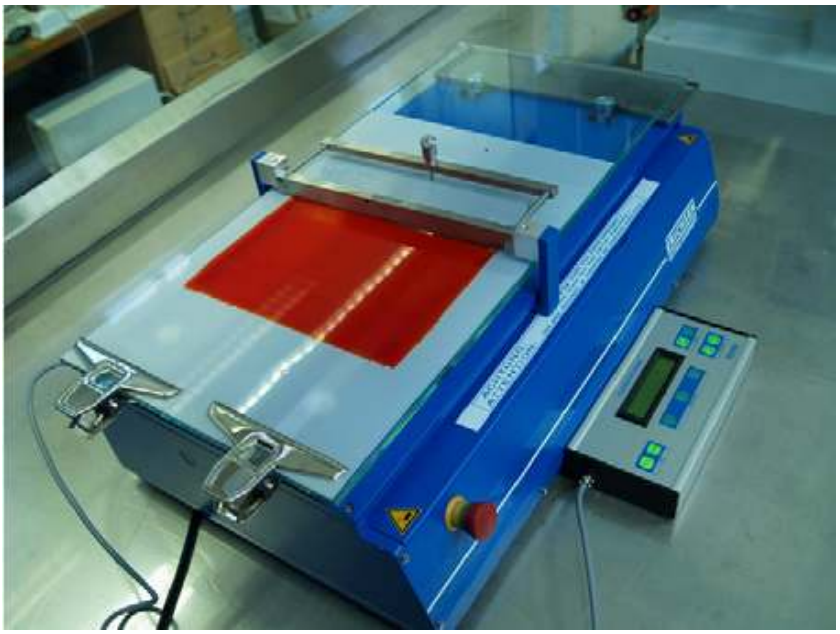

FIGURE 3.5: Doctor blade from Erichsen blading a polymer solution. Adapted with permission from [15]. Copyright 2009, Elsevier.

3.3.1.2 Thickness Measurement

The thickness of thin films was measured using a profilometer (Tencor). A profilometer scans a surface with a small needle and registers height differences. The lateral resolution is in the μm range due to the diameter of the tip of the needle, but the height resolution is in the nm range. The thickness of a film can be measured by removing a part of the film via scratching and measuring the difference from surface of the film to the bottom of the gap. The layers in section 4.2 were measured with an interferometer (NanoFocus) in a comparable way.

3.3.1.3 (Conductive) Atomic Force Microscopy (AFM, c-AFM)

Atomic force microscopy (AFM) was used in this thesis to study the surface and quality of thin films. A thin cantilever is used to scan the surface of the layers and detects height variations in the nm regime. Topographical measurements were done using the tapping mode of a Veeco D3100. Conductive AFM measurements detect the topography and the surface conductivity of a sample at the same time. These measurements were performed in the contact mode. A voltage was applied in between the conductive tip of the cantilever and the sample and the current was detected. These measurements were done with a Bruker Dimension Icon with a NanoScope V controller.

3.3.2 Electrical Characterization

3.3.2.1 External Quantum Efficiency

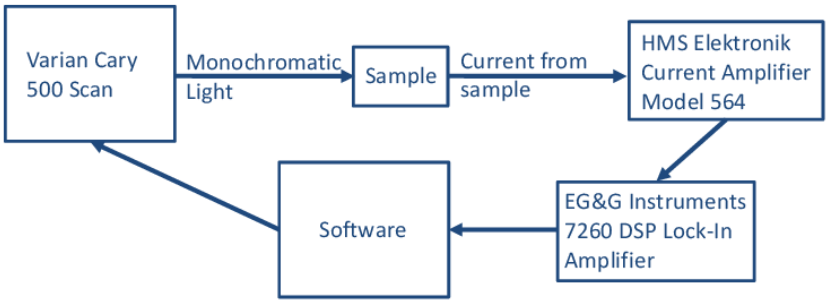

FIGURE 3.6: Scheme of EQE measurement setup.

The scheme of the EQE measurement setup is depicted in Figure 3.6. The samples were illuminated with monochromatic light by a Varian Cary 500 Scan spectrometer with tungsten light source. The current of the sample cell was pre-amplified by a current amplifier from HMS Elektronik and then by a EG&G Instruments Lock-In amplifier. The system was controlled by a custom-made software and referenced to a calibrated Si diode at the beginning of each measurement session.

3.3.2.2 Conductivity Measurements

In this work, the conductivity of thin film samples was measured in a 2-point geometry. As the samples are usually highly resistive, the error of neglecting the contact resistance by not using a 4-point geometry should be quite small. Moreover, the focus is lying on comparing samples, not so much on absolute values. The samples for conductivity measurements were prepared as follows. The sample material was deposited on a glass substrate. The metal electrode of either Al or Ag was deposited using thermal evaporation through a shadow mask. The shadow mask had 2 mm wide lines which were spanned by thin metal wires ($\oslash = 50\ \mu$m). The resistance was measured over the fine gaps that these wires created in the metal line. The conductivity was calculated in Siemens (S) per cm using the slope of the I-V curve measured over the gap with a source measurement unit (SMU, Fa. Keithley 236) with equation:

$$\sigma = \frac{Gap\ width * Slope\ (I-V)}{Layer\ thickness * Contact\ width} \quad \left[\frac{S}{cm}\right] \tag{3.1}$$

The "Gap width" was measured with an optical microscope, the "Layer thickness" with a profilometer (see subsection 3.3.1.2) and the "Contact width" was 0.2 cm. In section 4.2, the conductivity was measured by a potentiostat (Autolab, Metrohm).

Chapter 4

Electron Transport Layers: Zinc Oxide and Aluminum-doped Zinc Oxide

4.1 Electrical Simulations of Electron Transport Layers

Abstract

A minimum conductivity threshold value for "thick" interface layers was estimated by using microscopic 1d electrical simulations of a simplified device stack. A minimum conductivity was found that allows to vary the thickness of the interface layer over a wide range without hampering solar cell performance.

Adapted from Ref. [16] with permission from The Royal Society of Chemistry.

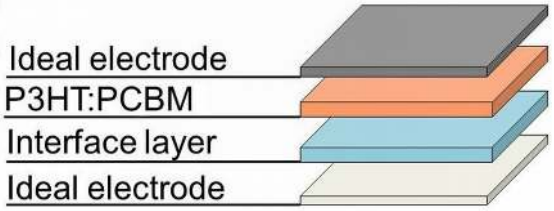

FIGURE 4.1: Simplified device stack used in the simulations. Adapted with permission from Ref. [16] with permission from The Royal Society of Chemistry.

The electrical behavior of solar cells is simulated to derive a conductivity design rule for electron transport layers (ETLs). Namely, the minimum necessary conductivity that the series resistance of the ETL is negligible for the device series resistance and does not affect the performance parameters. The simulations solve the fully coupled nonlinear equations for the 1d microscopic transport with the software PC1D [92]. Figure 4.1 shows the simplified stack used for the microscopic simulation. The thickness and the conductivity (σ) of the interface layer are systematically varied over a wide range of parameters. The parameter set used for the simulation is given in Appendix A.

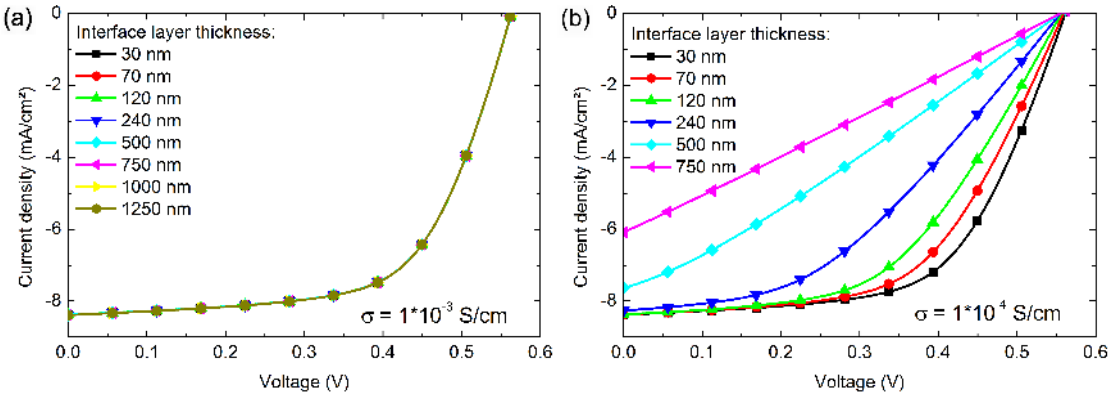

FIGURE 4.2: Simulated j-V characteristics with varying interface layer thicknesses for a conductivity of $1*10^{-3}$ (a) and $1*10^{-4}$ S/cm (b). No limitation of device performance is observed for $1*10^{-3}$ S/cm, while $1*10^{-4}$ S/cm heavily reduces the device performance with increasing interface layer thickness. Reproduced from Ref. [16] with permission from The Royal Society of Chemistry.

Figure 4.2 shows the results for conductivities of $1*10^{-3}$ and $1*10^{-4}$ S/cm with a variation of thicknesses ranging from 30 to 1250 and 30 to 750 nm, respectively. For a conductivity of $1*10^{-3}$ S/cm, no limitation due to the increased interface layer thickness is observed from the device performance. In contrast, a conductivity of only $1*10^{-4}$ S/cm is clearly limiting device performance due to an increased series resistance for thicker films. If the conductivity is further reduced, the typical s-shape behavior in the j-V characteristics is found (see Figure 4.3) [10].

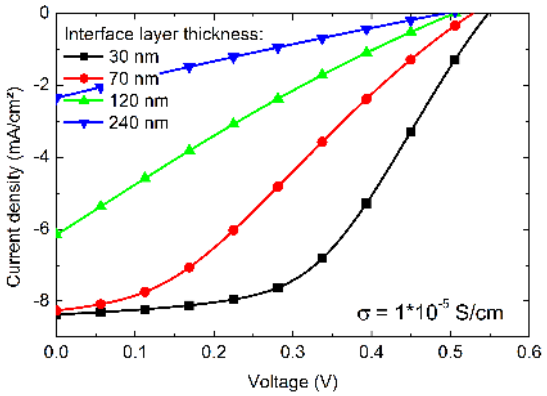

FIGURE 4.3: Low conductive interface layer ($\sigma = 1{*}10^{-5}$ S/cm) induces s-shape behavior in the j-V characteristics. Reproduced from Ref. [16] with permission from The Royal Society of Chemistry.

4.1.1 Summary

Concluding, numerical simulations suggest that a conductivity of $>= 1 * 10^{-3}$ S/cm for the interface layer is sufficient to process thick (i.e. $>$ 100 nm) electron transport layers. These simulations did not take into account secondary effects like contact barriers, photoconductivity, shunts or photoshunts as well as microstructure changes in the thick film limit (interface and/or active layer).

4.2 Comparison of Al-doped Zinc Oxide to Intrinsic Zinc Oxide

Abstract

In this section, a route to solve one of the big challenges in the large scale printing process of organic solar cells is demonstrated. The reliable deposition of very thin layers is problematic. Especially materials for electron (ETL) and hole transport layers (HTL) (except poly(3,4-ethylene dioxythiophene):(polystyrene sulfonic acid) (PEDOT:PSS)) have a low conductivity and therefore require thin films with only a few tens of nanometers thickness to keep the serial resistance under control. To overcome this limitation, inverted polymer solar cells with an active layer comprising a blend of poly(3-hexylthiophene) (P3HT) and [6,6]-phenyl-C61 butyric acid methyl ester (PCBM) with solution processed aluminum-doped zinc oxide (AZO) ETL were investigated. Devices with AZO and intrinsic zinc oxide (ZnO) ETL showed comparable efficiency at low layer thicknesses of around 30 nm. The conductivity of the doped zinc oxide was found to be three orders of magnitude higher than for the ZnO reference and was matching the simulated threshold value that was calculated in the previous section 4.1. Therefore the buffer layer thickness can be enhanced significantly to more than 100 nm without hampering the solar cell performance, while devices with 100 nm ZnO films already suffered from increased series resistance and reduced efficiency.

4.2.1 Materials and Thin Film Properties of ZnO and HT AZO

A typical solution processed ETL is intrinsic ZnO. The layers are either deposited from nanoparticle dispersion [53] or precursor solution [55]. Here, a nanoparticle approach is chosen as reference material for comparison with the doped ZnO. The doping of ZnO with Al is a common approach to increase the conductivity of ZnO [89], but usually either vacuum processes are used for the deposition [89] or very high annealing temperatures (> 400 °C) for solution processed films (see subsection 3.2.2) [14]. In this work, solution processed AZO annealed at lower temperatures is investigated and integrated in devices. The synthesis routes of the ZnO nanoparticles and the AZO solution are described in Appendix C. The ZnO film was deposited via doctor blading and dried at 150 °C for 10 min. Conversion of the precursor to AZO via hydrolysis was achieved by heating the samples to 260 °C for 10 min after doctor blading. This AZO version is therefore named "high temperature" (HT) AZO. Higher layer thicknesses were achieved via subsequent deposition steps. In case of HT AZO, an annealing step was applied after each deposition.

In this section, the electrical conductivity was measured by a potentiostat (Autolab, Metrohm) and the thickness of the thin films was measured by an interferometer (NanoFocus) (see sections 3.3.1.2 and 3.3.2.2).

ETL	Crystallite size (nm)	Work function (eV)	Optical bandgap (eV)	Conductivity (S/cm)
ZnO	4.2	4.3	3.45	$2.22 * 10^{-6}$
HT AZO	4.0	4.2	3.34	$2.35 * 10^{-3}$

TABLE 4.1: Comparison between the thin film properties of ZnO and HT AZO. The properties are very comparable except the three orders of magnitude higher conductivity of HT AZO. The difference in the optical bandgap cannot be discussed in terms of the Moss-Burstein model due to the different synthesis, processing and conversion conditions of the ZnO versus the HT AZO film. Adapted with permission from [17]. Copyright 2011, Elsevier.

Table 4.1 compares the optical, electrical and crystallite properties of ZnO vs. HT AZO. XRD spectra of HT AZO layers reveal a lattice stress in the 002 plane when aluminum is introduced, indicating that higher concentrations of aluminum are interstitially built into the lattice. ZnO particles are wurtzite type crystallites with an average crystal size of 4.2 nm while we find an average crystal size of 4.0

nm for the converted HT AZO layers [48]. The optical band gap is determined by plotting $(\alpha h\nu)^2$ against $h\nu$ from UV-VIS absorption data. The optical bandgap can be found by extrapolating the linear portion of the curve to zero absorption [48]. The transmittance of the two materials is comparable. The most important difference is the increase in conductivity by about three orders of magnitude for HT AZO. A more detailed study of the ZnO layers can be found in [48].

4.2.2 Comparison of ZnO and HT AZO in Solar Cells

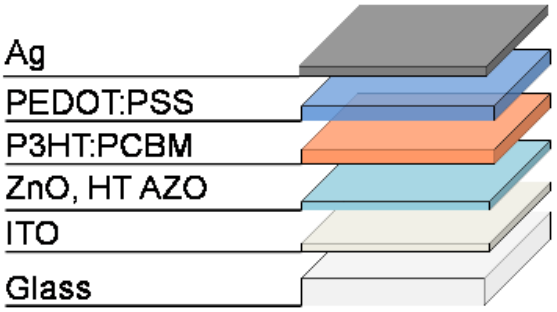

FIGURE 4.4: Layer stack of the investigated devices for the comparison of ZnO and HT AZO ETLs. Adapted with permission from [17]. Copyright 2011, Elsevier.

The layer stack of the investigated devices is shown in Figure 4.4. The j-V characteristics of typical solar cells with thin ZnO and HT AZO layers (around 30 nm) are depicted in Figure 4.5 and devices with thick ETL layers (above 100 nm) are shown in Figure 4.6. The solar cell data for all configurations is summarized in Table 4.2. A device without ETL is shown as reference in Figure 4.5 as well. The j-V characteristics of the devices without ETL are dominated by a large, so-called photoshunt ($R_{Photoshunt}$) [7] and are further injection limited, which results in a nominal very high serial resistance of 23.6 Ωcm^2 (calculated from the slope around 1.25 V). Both loss mechanisms originate at the far from optimized ITO\PCBM interface. The photoshunt can be identified by the difference in the slope of the illuminated versus the dark j-V curve at negative applied voltages. It originates from the several orders of magnitude higher charge carrier density of the active layer under illumination. The same mechanism is responsible for photoconductivity as well seen under forward bias as an increased injection current density. In case of the poorly charge selective ITO\PCBM interface, holes are more easily injected into the active layer at the nominal cathode. Therefore the shunt resistance scales with the conductivity of the active layer. Together with the ITO\PCBM contact resistance, this results in decreased key solar cell parameters: Open circuit voltage (V_{OC}, 426 mV), short circuit current density (j_{SC}, -6,86 mA/cm^2), fill factor (FF, 29.2 %) and consequently poor power conversion efficiency (PCE) of only 0.85 %.

Thin layers (≈30 nm) of ZnO and HT AZO provide a much better electron selective interface and ohmic cathode contact. Losses at the cathode interface are minimized, because the electrons are extracted to ZnO or HT AZO, both at a higher work function than bare ITO. This results in increased FF, V_{OC} and j_{SC}

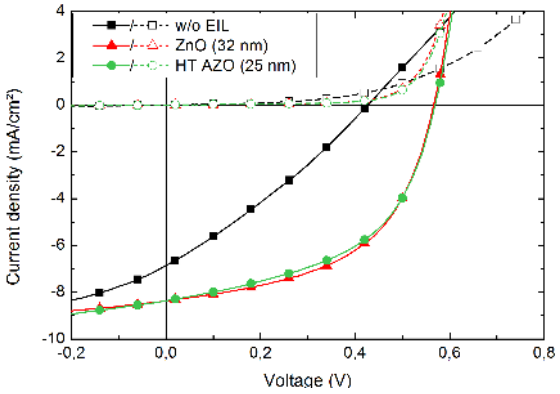

FIGURE 4.5: j-V characteristics of solar cells without ETL, thin ZnO and HT AZO films. Adapted with permission from [17]. Copyright 2011, Elsevier.

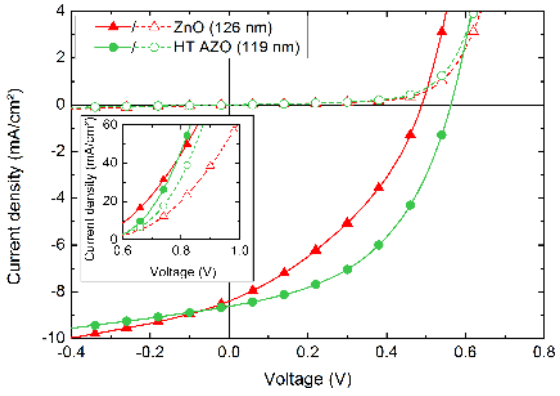

FIGURE 4.6: j-V characteristics of solar cells with thick ZnO and HT AZO films. The inset shows the injection behavior for high forward bias. Adapted with permission from [17]. Copyright 2011, Elsevier.

and a significantly higher PCE of around 2.5 % for both EILs. The series resistance of both device configurations is around 1.1 Ωcm^2 and well within expectations.

ETL	V_{OC} (mV)	j_{SC} (mA/cm^2)	PCE (%)	FF (%)	R_S (Ωcm^2)	R_{Shunt} ($k\Omega cm^2$)
w/o ETL	426	-6.86	0.85	29.2	23.6	3.0
ZnO (32 nm)	565	-8.41	2.56	53.9	1.1	6.2
ZnO (126 nm)	486	-8.40	1.54	37.7	3.2	3.1
HT AZO (25 nm)	569	-8.36	2.42	50.8	1.1	4.9
HT AZO (119 nm)	558	-8.69	2.40	49.4	1.2	3.9

TABLE 4.2: Key parameters of the investigated solar cells without ETL and thin\thick ZnO or HT AZO ETL. Adapted with permission from [17]. Copyright 2011, Elsevier.

Increasing the layer thickness of the ZnO from around 30 to over 100 nm results in a severely reduced device performance from 2.5 to 1.5 %. The main losses are a reduction of the FF from 53.9 to 37.7 % and a reduction of the V_{OC} from 565 mV

to 486 mV. These losses originate dominantly from three different mechanisms, which can be observed in the j-V-characteristics. First, an increase of the series resistance from 1.1 to 3.2 Ωcm^2 (see inset of Figure 4.6) is caused by the thick ZnO layer. The higher R_S results dominantly in a FF loss. The V_{OC} loss is more subtle. The increased series resistance due from the ZnO layer is not expected to influence V_{OC} unless significant carrier recombination occurs in this region. Given the good charge selectivity of the ZnO layer, we exclude this loss mechanism. A contribution to the FF and V_{OC} loss originates from the already introduced photoshunt, which is much more strongly expressed in the case of thick ZnO layer. Photoshunts are a result of an interface-shunt, i.e. a defect shunting the electrode and the semiconductor. The photoshunt resistance is strongly dependent on the minority carrier blocking properties of the interface, the so called contact permeability of the buffer layers. This translates in our architecture to a defect, where holes become injected directly into the active layer via the ZnO [7]. We note that the photoshunt seems to emerge with increased ZnO layer thickness, as the shunt resistance under illumination is reduced from 0.59 $k\Omega cm^2$ for the thin ZnO ETL down to 0.33 $k\Omega cm^2$ for the thicker ZnO ETL (see Table 4.2). The dark shunt resistance also decreases from 6.0 $k\Omega cm^2$ to 3.1 $k\Omega cm^2$. This is an indication for a reduced layer quality of the thick films. In summary, the photoshunt contributes to the losses in V_{OC} and FF. The third loss mechanism is associated with the photoconductivity of the ETL, which is much more significant for the ZnO based devices as compared to the HT AZO based devices. Illuminated ZnO is significantly more conductive, which leads to enhanced carrier injection under forward bias. Overall, this effect causes an increased current density under illumination (see inset of Figure 4.6). This increased injected photocurrent does already compensate the photovoltaic photocurrent at lower bias, and in summary, the V_{OC} becomes reduced. This photoconductivity effect is responsible for the biggest part of the V_{OC} loss. Solar cells with a thicker AZO ETL do not suffer from these defects. The series resistance of a device with an approx. 120 nm HT AZO layer is still as low as 1.2 Ωcm^2, which shows, that the contribution of the HT AZO ETL is negligible. For thicker HT AZO ETL the photoshunt is maintained at values larger than 0.45 $k\Omega cm^2$, so the V_{OC} and the FF are not affected much as for the thick ZnO ETLs. All key parameters like FF, V_{OC}, j_{SC} and PCE remain constant for HT AZO layer thicknesses between 30 and 120 nm. In summary, doped ZnO opens the possibility to incorporate thick interface layers into the device architecture without sacrificing efficiency.

4.2.3 Summary

In this section, the interface layer specifications are discussed as required from a reliable, large volume printing process for polymer solar cells. A thick electron injection layer using a solution processed Al-doped ZnO with high conductivity was suggested for this purpose. An increase of the intrinsic ZnO layer from 30 nm to 120 nm reduced the device performance from initially 2.5 % to 1.5 %. The main losses are a reduction of the FF and V_{OC}, which are caused by the photoconductivity of the ZnO layer, the photoshunt behavior of the devices as well as its higher serial resistance. Aluminum doped ZnO could be processed as thick as 120 nm without causing losses. In the next step, the annealing temperature of the HT AZO films has to be reduced to around 150 °C before these films can be processed on plastic substrates as proposed in 2.4.4. This is the topic of the following section 4.3. Nevertheless, thick pin-hole free layers with good coverage are a prerequisite for the reliable large scale printing of organic solar cells with low shunts and high yield. In the presented concept, thick electron transport layers were incorporated into the devices and it is proposed that mechanically robust, thick ETLs and HTLs will be beneficial for the processing of thin active layers. This concept appears as an interesting strategy to optimize the lifetime and performance of single junction as well as tandem junction solar cells.

4.3 Precursor Engineering for Improved Processing Conditions

Abstract

Higher conductive aluminum-doped zinc oxide (AZO), which was introduced in the previous section 4.2 meets the desired conductivity threshold, however, at the cost of high temperature processing. High annealing temperatures (>150 °C) significantly improve the electrical properties of metal oxides, but prohibit processing on plastic substrates or organic active layers. Here we report on AZO layers from a sol-gel precursor, which already gives sufficient high conductivities at lower processing temperatures (<150 °C). The influence of different precursor compositions on the electrical properties of the thin films and their performance in inverted poly(3-hexylthiophene):[6,6]-phenyl-C61 butyric acid methyl ester (P3HT:PCBM) solar cells was investigated. Low temperature AZO layers with thicknesses up to 680 nm maintained comparable performance to devices with thin AZO layers.

Section adapted from Ref. [16] with permission from The Royal Society of Chemistry.

4.3.1 Characterization of AZO Layers from Different Precursor Formulations

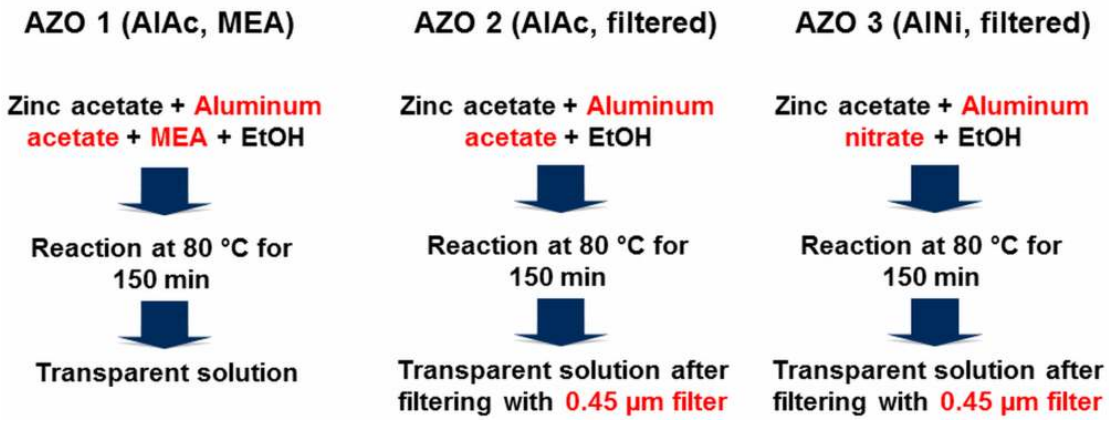

FIGURE 4.7: Schemes of the synthesis routes for the three investigated AZO precursor formulations. Reproduced from Ref. [16] with permission from The Royal Society of Chemistry.

Three different precursor formulations based on zincacetate were synthesized to determine the relation between composition and film properties (Figure 4.7). Either aluminumacetate (AlAc) or aluminumnitrate (AlNi) was used as dopand. Apart from that, the precursor formulations were stabilized with ethanolamine (MEA) or filtered after reaction. The three investigated formulations were (i) AZO 1 (AlAc dopand, MEA stabilized), (ii) AZO 2 (AlAc dopand, no stabilization, filtered) and (iii) AZO 3 (AlNi dopand, no stabilization, filtered). The synthesis routes are described in Appendix C. The synthesis route for AZO 1 is the same as the previously presented HT AZO. The resulting conductivities of the films were measured in the 2 point probe geometry as a function of two different annealing temperatures: 140 °C or 260 °C (see Table 4.3). 140 °C is a suitable temperature for plastic substrates and for the deposition onto organic films, while 260 °C is chosen as reference (see section 4.2). As reported before, AZO 1 reaches a conductivity value in the order of 10^{-3} S/cm after annealing at 260 °C, while annealing at lower temperatures results in conductivities in the order of 10^{-5} S/cm. AZO 2 gives a conductivity of 10^{-4} S/cm at 140 °C, which is already close to the target conductivity. The best conductivity at 140 °C annealing is found for AZO 3 with $7 * 10^{-3}$ S/cm. AZO 3 at 140 °C has similar conductivity as AZO 1 at 260 °C.

Interestingly, AZO 2 and 3 show even higher conductivities above 10^{-1} S/cm when annealed at 260 °C. A possible explanation for this improvement, when the precursor solution is filtered instead of stabilized, is that MEA forms metal-organic

	Conductivity (S/cm)	
Materials	140 °C	260 °C
AZO 1 (AcAc, MEA)	$8 * 10^{-5}$	$4 * 10^{-3}$
AZO 2 (AcAc, filtered)	$3 * 10^{-4}$	$7 * 10^{-0}$
AZO 3 (AlNi, filtered)	$7 * 10^{-3}$	$6 * 10^{-1}$

TABLE 4.3: Conductivities of the investigated AZO precursors at 140 and 260 °C. AZO 1 at 260 °C ≙ HT AZO and AZO 3 at 140 °C ≙ LT AZO. Adapted from Ref. [16] with permission from The Royal Society of Chemistry.

complexes with zincacetate [93, 94]. These complexes need higher temperatures to decompose. The benefit of exchanging AlAc by AlNi is most likely due to the better solubility of AlNi in ethanol. This could promote a more homogenous distribution of Al in the precursor complex and result in a more effective doping. To investigate the nature of the observed conductivity variations, the mobility (μ_{FET}) of the AZO 1 and 3, annealed at either 140 °C or 260 °C, was measured in a thin film transistor geometry. All films showed a μ_{FET} in the range of $0.5-5.3*10^{-3}$ cm^2/Vs (see Appendix D). As the conductivity ($\sigma = e * n * \mu$; e = elementary charge, n = carrier concentration, μ = mobility) of the four films varies by 4 orders of magnitude, the major influence on the conductivity is assigned to an increase in the carrier concentrations rather than in the mobility. According to the conductivity investigations, LT AZO (AZO 3 at 140 °C) was chosen for solar cell testing (see next subsection 4.3.2) and referenced to the previously investigated HT AZO (AZO 1 at 260 °C) (see section 4.2). The work function of LT AZO was measured using Kelvin probe to -4.4 eV. This is sufficiently low to properly contact the lowest unoccupied molecular orbital (LUMO) of PCBM (at -4.3 eV) and is further comparable to the previously reported -4.2 eV for HT AZO (see section 4.2). The LT AZO layers have a high transmission, comparable to the previously investigated (doped) zinc oxides (see Figure 4.8). Even very thick LT AZO films of up to 680 nm have very high transmittance in the visible. They only show increased absorption in the UV which is due to the optical bandgap. The optical bandgap was calculated from a Tauc-plot to 3.3 eV, assuming a direct bandgap (HT AZO: 3.2 eV (see section 4.2)).

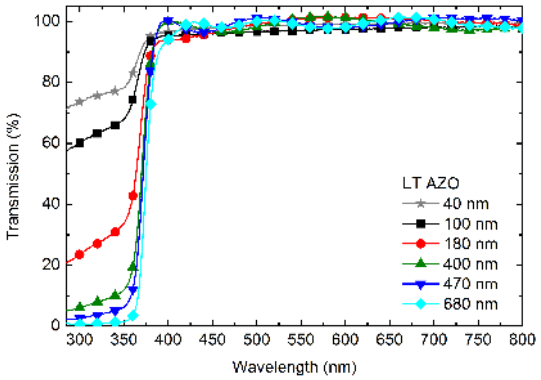

FIGURE 4.8: Optical transmission of LT AZO films with thicknesses from 40 to 680 nm excluding the glass substrate. The transmission is very high for all thicknesses in the visible wavelengths. Reproduced from Ref. [16] with permission from The Royal Society of Chemistry.

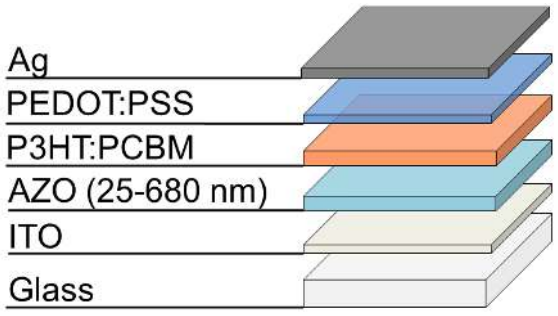

FIGURE 4.9: Layer stack of investigated devices comparing HT and LT AZO at different layer thicknesses. Reproduced from Ref. [16] with permission from The Royal Society of Chemistry.

4.3.2 Solar Cell Experiments with Different AZO Precursors

The layer stack of the investigated devices is displayed in Figure 4.9. The solar cells were processed as described in Appendix B. The performance of HT and LT AZO was compared in experiment A. The statistics of the key parameters are summarized in Figure 4.10. The thickness of the ETLs was varied from 25 over 120 to 220 nm for HT AZO and from 40 over 120 to 240 nm for LT AZO. Thicker layers were processed through subsequent deposition and annealing steps. The V_{OC} of all devices is sufficiently high and comparable. For the j_{SC} we observe some statistical variation without a specific trend. The FF trend is more interesting and relevant to discuss. The FFs of the devices with the two thinnest ETLs is above 55 %, while the devices with the thickest AZO (> 200 nm) layers is in the 50-55 % regime. Analyzing the device with the one diode model and comparing the series

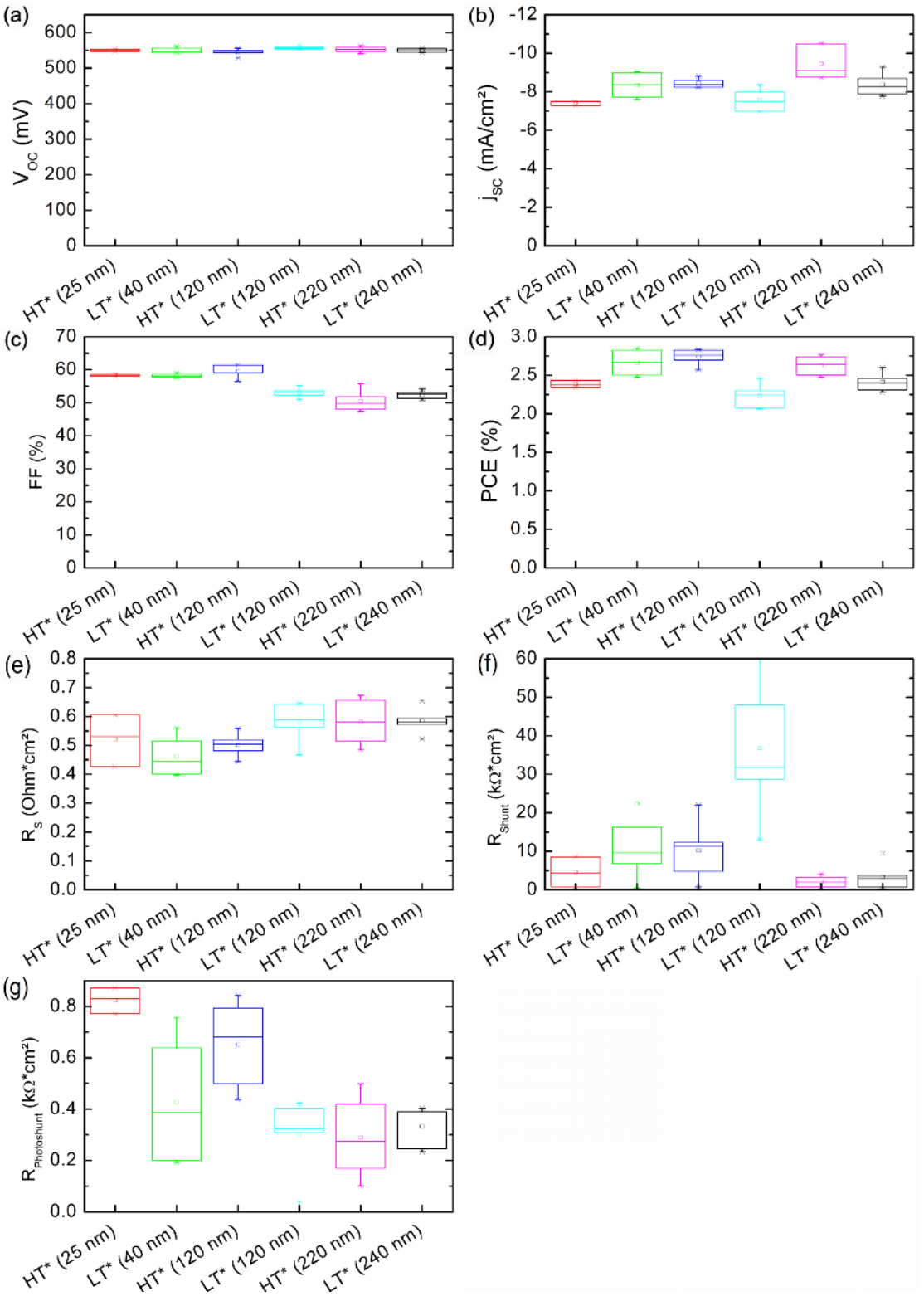

FIGURE 4.10: Key parameters (V_{OC}, FF, j_{SC}, PCE, R_S, R_{Shunt} and $R_{Photoshunt}$) of the investigated devices in experiment A with AZO layers from two different precursors* and annealing conditions as a function of ETL thickness. (*HT=High temperature (260 °C) annealed AZO 1 (AlAc, MEA stabilized), LT=Low temperature (140 °C) annealed AZO 3 (AlNi, filtered)). Reproduced from Ref. [16] with permission from The Royal Society of Chemistry.

and parallel resistance reveals that the series resistance is comparably low for all AZO layers. At a series resistance $< 1\ \Omega cm^2$, no losses in the FF are expected (Figure 4.10 e)). The shunt resistance is sufficiently high for all configurations (Figure 4.10 f)). The photoshunt resistance, which is the shunt resistance of the illuminated curve (see description in section 4.2), shows a slight trend to lower values for higher AZO film thicknesses (Figure 4.10 g)). The efficiency of LT AZO at 140 °C matches the performance for the HT AZO processed at 260 °C in film conductivity and solar cells. The simulations in section 4.1 predict that with the conductivity of LT AZO, a several hundred nanometer ETL should be possible. In experiment B, up to 680 nm thick LT AZO ETLs were incorporated into the solar cells to verify the prediction. The illuminated j-V characteristics of the devices are displayed in Figure 4.11 and the key parameters are listed in Table 4.4. For the thickest tested film, the R_S still stays low at around 1 Ωcm^2. Therefore, the performance of the devices is comparable in FF ($\approx$ 60 %) and V_{OC} ($\approx$ 0.56-0.58 V) for all tested thicknesses. The j_{SC} varies around $\approx 1\ mA/cm^2$ which can be due to the morphology of the very thick films and optical effects (see figure 4.12). All that combined, the reduction of the PCE for thick films, even up to 680 nm, is only 10 % compared to the 100 nm AZO film.

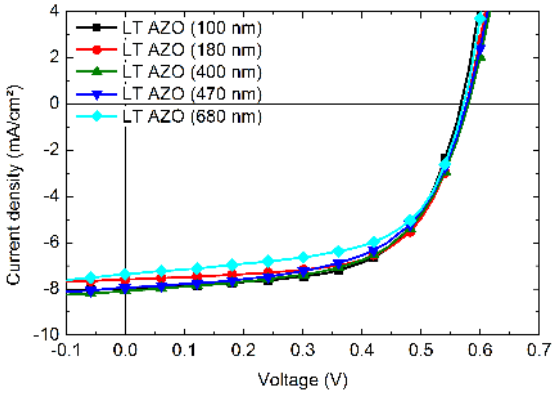

FIGURE 4.11: Illuminated j-V characteristics of experiment B with different thicknesses (100-680 nm) of the low temperature (140 °C) processed AZO 3 (LT AZO) EELs. Reproduced from Ref. [16] with permission from The Royal Society of Chemistry.

4.3.3 Summary

Through a systematic variation of the AZO precursor materials, an improved formulation for highly conductive AZO layers processed at low temperatures was identified. The filtered precursor comprising aluminumnitrate dopand (AZO 3)

ETL LT AZO	V_{OC} (V)	j_{SC} (mA/cm^2)	PCE (%)	FF (%)
100 nm	0.57	-7.98	2.79	61.4
180 nm	0.58	-7.59	2.79	63.4
400 nm	0.57	-8.09	2.70	58.6
470 nm	0.58	-7.94	2.68	58.1
680 nm	0.57	-7.37	2.52	60.0

TABLE 4.4: Key parameters of the devices of experiment B with different thicknesses (100-680 nm) of the low temperature (140 °C) processed AZO 3 (LT AZO) EELs. Adapted from Ref. [16] with permission from The Royal Society of Chemistry.

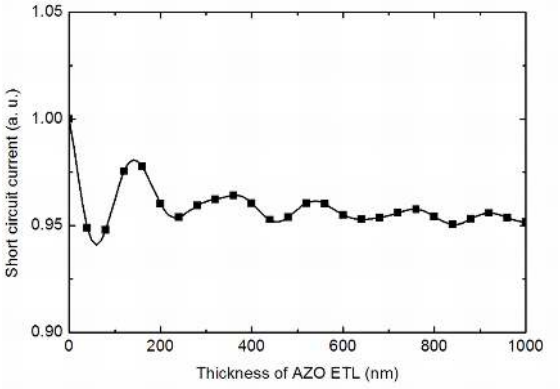

FIGURE 4.12: Optical simulation of the short circuit current with varying AZO EEL from 0-1000 nm. The simulated layer stack was Glass/ ITO(400 nm) / AZO(0-1000 nm) / P3HT:PCBM(100 nm) / PEDOT:PSS(40 nm) / Ag(100 nm). Reproduced from Ref. [16] with permission from The Royal Society of Chemistry.

shows the best electrical properties ($\sigma = 7{*}10^{-3}$ S/cm) at 140 °C. The conductivity of these layers matches the films of the previously investigated formulation AZO 1 at 260 °C (see section 4.2) and is above the simulated threshold to overcome the thickness restriction for interface layers ($\sigma = 1 * 10^{-3}$ S/cm) from section 4.1. As a result, the performance of these two films as ETLs in polymer solar cells is also comparable and well. Even when applying the LT AZO EEL in thicknesses of 680 nm, the efficiency and the series resistance of the devices are still comparable to the ones with thin ETLs.

Comparing the properties of LT AZO with the large area production requirements from section 2.4.4, all the desired properties are achieved except the ultra low annealing temperatures of only 80 °C and the preferred pathway of a nanoparticle dispersion. Nevertheless, due to their excellent properties, LT AZO layers found

application together with silver nanowires as transparent, solution processed electrode (see section 4.5) and in tandem solar cells [95], but the use directly on top of organic layers was found to be problematic (see section 4.6).

4.4 Surface Modification of AZO Interface Layers

Abstract

In this part of the work, the influence of aluminum-doped zinc oxide (AZO) electron extraction layers (EEL) modified with self-assembled monolayers (SAMs) on the j-V characteristics of inverted polymer solar cells based on a poly(3-hexylthiophene) (P3HT) and [6,6]-phenyl-C61 butyric acid methyl ester (PCBM) active layer was studied. It is found that phosphonic acid anchored SAMs can decorate the surface of AZO nanoparticles and modify its electrical properties. This leads to an increase in the parallel resistance, but also in the series resistance of the corresponding photovoltaic devices. It is further shown that an increase in series resistance can be avoided by employing a SAM forming molecule with a buckminster fullerene (C60). Charge transfer from C60 to AZO is efficient and leads to a reduction of the series resistance, while maintaining the high parallel resistance. This results in an increased fill factor and short circuit current density of the solar cells and a relative efficiency enhancement from 2.9 to 3.3 %.

4.4.1 AZO Surface Modified Through Self-Assembled Monolayers

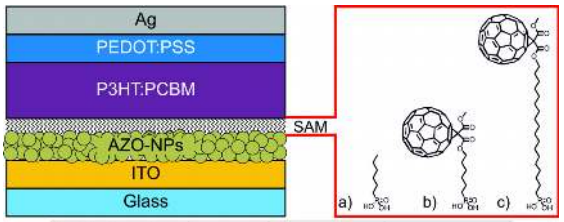

Contact angles				
Substrate	w/o	SAM(C6)	SAM(C6-C60)	SAM(C18-C60)
AZO	50.8	120.6	77.2	75.7
AlO_X	-	98.2	79.0	85.8

FIGURE 4.13: Layer stack of the investigated solar cells, SAM molecules a) C6 alkane spacer (SAM(C6)), b) C6 alkane spacer with fullerene (SAM(C6-C60)), and c) C18 alkane spacer with fullerene (SAM(C18-C60)) and contact angles of water on reference AZO and AlO_X substrates with and without SAMs. Reproduced with permission from Ref. [18]. Copyright 2012, Wiley VCH.

One of the weak points of metal oxide based EELs frequently discussed are their reliability and reproducibility when processed at low temperature (i.e. below 140 °C) [96]. Low processing temperatures may yield incomplete ligand removal, and thus result in bad control of the electronic surface properties. Decoration of metal oxides with self-assembled monolayers (SAMs) is one way to achieve defined surface properties. Potential SAM anchoring groups to metal oxides are amines, mercaptanes, catechol, carboxylic or phosphonic acids (PAs) [52, 54, 74, 97]. Among these, the bidentate phosphonic acid group forms a strong bond [97].

4.4.2 Organic Solar Cells with SAM-Modified AZO ETLs

In this section, PA anchored aliphatic and fullerene functionalized SAMs are explored as termination groups for doped metal oxide films. It is demonstrated that the functionality of the SAM molecule determines the electronic properties of the ETL and allows the controlling of series resistance as well as shunt resistance in organic solar cells. The polymer solar cells investigated in this section were fabricated according to the layer stack shown in Figure 4.13. The detailed description of the synthesis route for AZO can be found in Appendix C and the solar cell fabrication in Appendix B. The j-V characteristics of typical solar cells with AZO, AZO-SAM(C6), AZO-SAM(C6-C60) and AZO-SAM(C18-C60) are depicted in Figure 4.14. The solar cell data for all configurations is summarized in

Table 4.5 and the statistics on the key parameters are provided in the Figure 4.15. Hau et al. investigated phosphonic acid terminated SAMs and highlighted the possibility of etching damages of the TCO due to the phosphonic acid groups [74]. According to these findings, we chose a suitable ratio between the concentration of the SAM solution and the reaction time in the solution for proper deposition. The integrity of the AZO film after immersion in the SAM solution was confirmed with AFM images (see Figure 4.16), and the proper deposition of the SAM on AZO was monitored via contact angle measurements on reference AZO and AlO_X layers (Figure 4.13). Densely packed SAMs of hydrophobic n-alkane phosphonic acids were found to show large contact angles (> 95 °), while C60 terminated SAMs resulted in layers with smaller contact angles [98, 99]. The morphology and coverage of the SAMs on reference AZO layers was confirmed by c-AFM measurements (Figure 4.16). Proper termination of the AZO surface results in a reduction of the current (integral over all pixels) by one order in magnitude for both investigated SAMs.

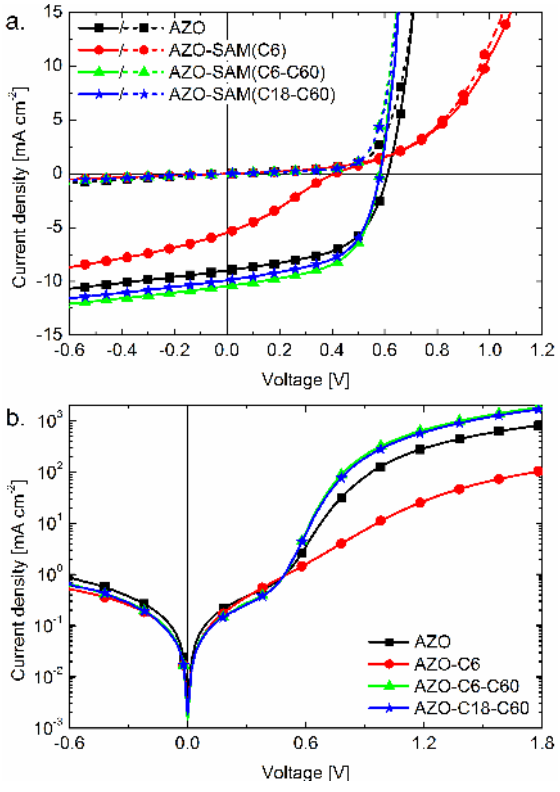

FIGURE 4.14: a) jV characteristics of best solar cells on the typical substrates (see Table 4.5). b) corresponding logarithmic plot of dark jV characteristics. Reproduced with permission from Ref. [18]. Copyright 2012, Wiley VCH.

The reference cells with only the AZO ETL have an open circuit voltage (V_{OC}) of 602 mV, a short circuit current density (j_{SC}) of -9.23 mA/cm^2, a fill factor (FF)

of 51.9 % and a power conversion efficiency (PCE) of 2.88 %. The series resistance (R_S) is 1.2 Ωcm^2 and the parallel resistance (R_P) is 655 Ωcm^2. Deposition of the SAM with the alkane spacer unit (SAM(C6)) deteriorates the device performance. The V_{OC} drops to 354 mV, the j_{SC} to -3.94 mA/cm^2, and the FF is reduced to 25.3 %. Consequently, the PCE drops down to 0.38 %. The j-V characteristics show an s-shape commonly referred to as second diode behavior. The occurrence of an s-shape was discussed in terms of surface recombination [100], work function mismatch and interface barrier [10, 32], or low transport properties [32]. Here, we ascribe the s-shape to the insulating layer formed by the short alkane chains, which is probably best understood as interface barrier with low transport properties. As a result, the non-conductive alkane chains hinder the charge transfer from PCBM to AZO, and the R_S of the devices is increased to 9.5 Ωcm^2. The R_P is increased to 1011 Ωcm^2, which is due to the decoration of the AZO nanoparticles by an insulating nanolayer, resulting in a suppression of the leakage current density.

ETL	V_{OC} (mV)	j_{SC} (mA/cm^2)	PCE (%)	FF (%)	R_S (Ωcm^2)	R_{Shunt} ($k\Omega cm^2$)
AZO	602	-9.23	2.88	51.9	1.2	655
(Best)	(620)	(-9.00)	(2.98)	(53.6)	(1.2)	(692)
AZO-SAM(C6)	354	-3.94	0.38	25.3	9.5	1011
(Best)	(398)	(-5.48)	(0.63)	(28.7)	(9.9)	(1141)
AZO-SAM(C6-C60)	583	-9.92	3.32	57.4	0.6	1473
(Best)	(578)	(-10.46)	(3.32)	(57.4)	(0.6)	(919)
AZO-SAM(C18-C60)	584	-9.24	2.88	53.5	0.9	1353
(Best)	(577)	(-9.90)	(3.25)	(56.8)	(0.6)	(887)

TABLE 4.5: Key parameter set of the solar cells: average of at least 5 cells on a typical substrate. Best corresponds to the best cell on the substrate. Adapted with permission from Ref. [18]. Copyright 2012, Wiley VCH.

The solar cells with an AZO-SAM(C6-C60) cathode show a drastically improved performance as compared to alkane based SAMs. On the average, the C6-C60 terminated AZO does indeed perform slightly better than the pristine AZO reference. The performance data of the C6-C60 terminated AZO yield a V_{OC} of 583 mV, a j_{SC} of -9.92 mA/cm^2, a FF of 57.4 %, and a PCE of 3.32 %. The improvement is mainly due to an increased FF and a slightly higher j_{SC}. The parallel resistance increases up to 1473 cm, obviously due to the same mechanism as for the SAM(C6). In addition to that, the fullerene at the end of the alkane chain does successfully mediate charge transfer from the active layer into the AZO. The good series resistance together with the increased parallel resistance explains the better FF compared to the reference device. Hau et al. ascribed the j_{SC} increase

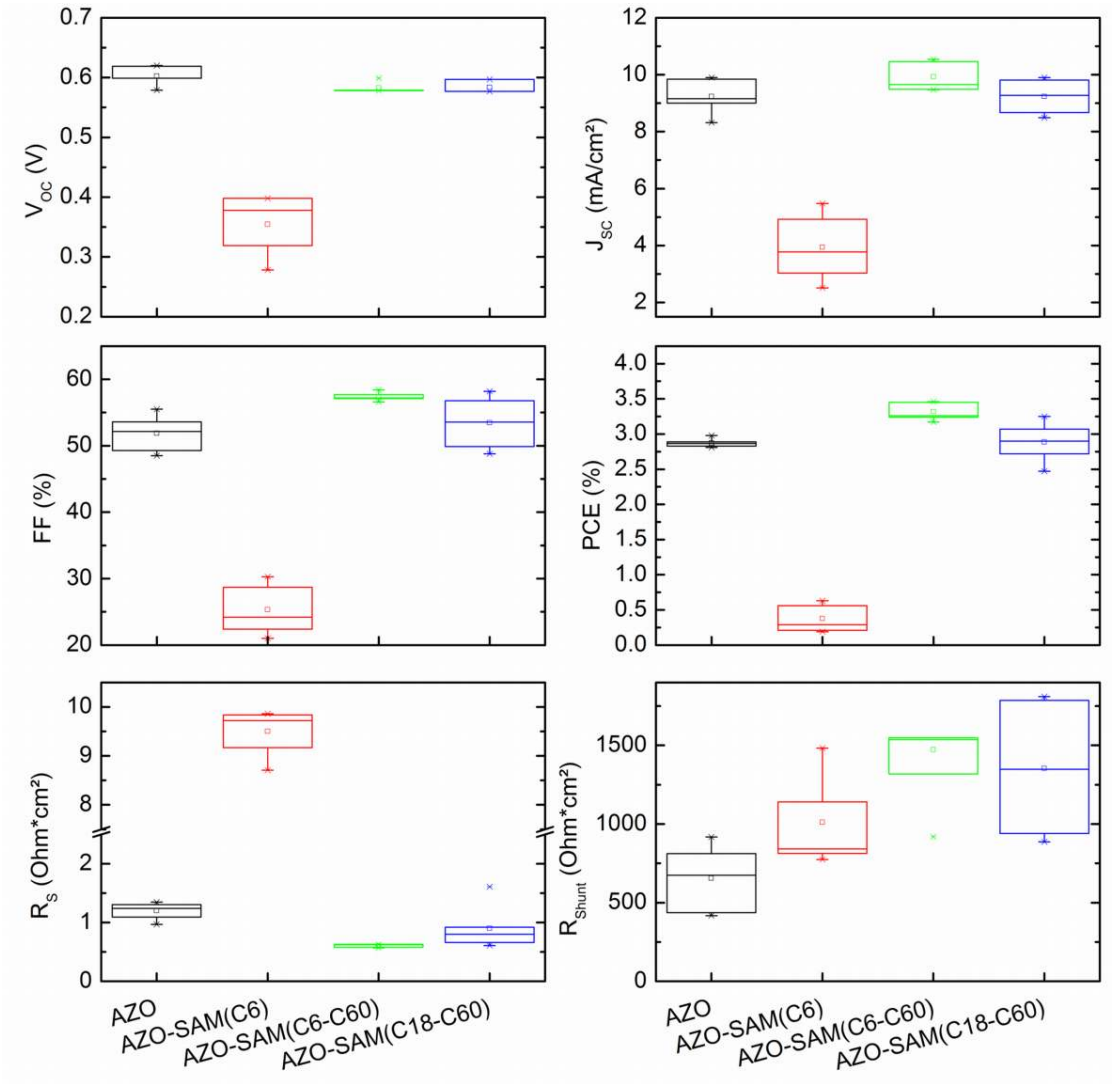

FIGURE 4.15: Boxplots of the key parameter sets of the investigated solar cells underlining the statistical relevance of the performance differences. Reproduced with permission from Ref. [18]. Copyright 2012, Wiley VCH.

to an improved morphology of the active layer, induced by the surface energy modification at the interface [97]. A better stratification of the fullerene - polymer microstructure is known to suppress recombination at the ETL/active layer interface. Finally, we verified that the length of the alkane chain in the SAM forming Fullerene molecules only slightly influences the charge transport processes. The performance of best devices incorporating SAMs with a long alkane spacer chain (SAM(C18-C60)) is almost comparable to the cells with a short spacer chain (see Figure 4.14). In particular the injected current density is equal for both fullerene containing SAMs, which proves that the increased spacer chain length from 6 to 18 units is not hindering the charge transfer between AZO and the organic semiconductor bulk. One explanation for this observation is that the Fullerene SAMs

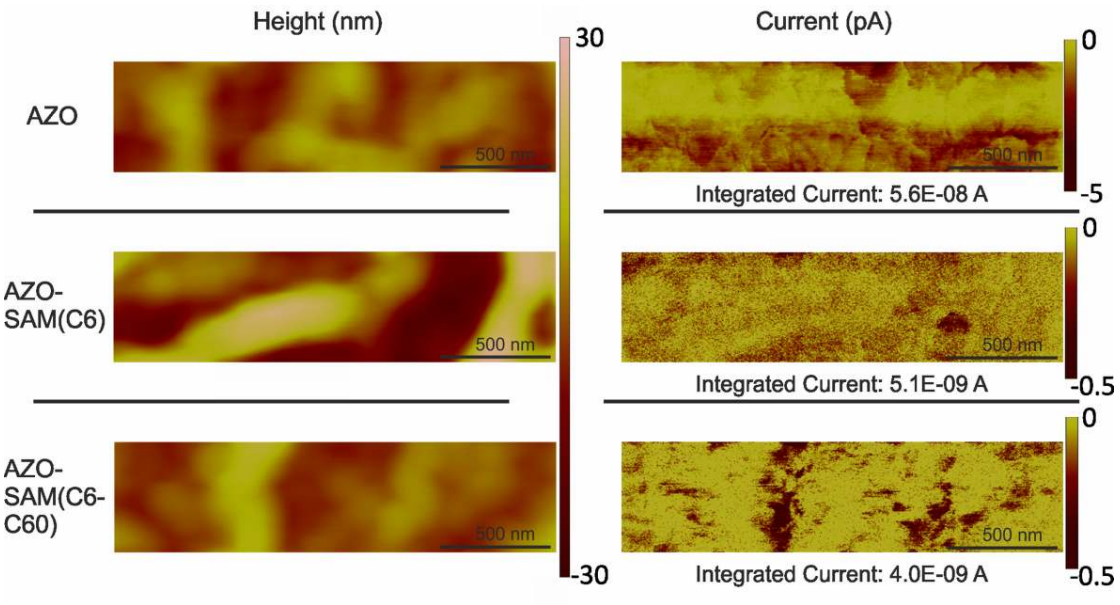

FIGURE 4.16: c-AFM measurements on bare AZO, AZO covered by the SAM(C6) and SAM(C6-C60). (Integrated Current resembles the addition of the currents for all pixels.). Reproduced with permission from Ref. [18]. Copyright 2012, Wiley VCH.

assemble in a densely packed but disordered manner with random distribution of C60 moieties within the layer thickness. A SAM(C18-C60) on flat AlO_X was found to be only 2.5 nm thick, while the fully stretched molecule is 3.5 nm long [98]. The same effect was observed on spherical objects with C18-C60 SAMs on ZnO nanorods [101]. Assuming a similar assembly behavior of the SAMs on AZO, the alkane chains are compressed or tilted in a way that the fullerene moiety can have direct contact with the AZO, which is certainly favored be the mismatch between the fullerene and the alkane chain/anchoring group. The AFM and c-AFM measurements in Figure 4.16 strongly support this hypothesis and suggest that such mismatch may preferentially occur at more irregular or rough layer regions, as expected for instance at the intersection of larger AZO regimes. For the C60 terminated SAM layers, higher current densities are observed specifically at those regimes where the height profile varies. As this behavior applies for both Fullerene SAMs, it could explain the similar performance of the solar cells.

4.4.3 Summary

The functionality of SAM modified AZO interfaces on the performance of P3HT / PCBM solar cells was investigated in detail. The successful and rather complete

decoration of the AZO surface with phosphonic acid anchored SAMs was proven and results in a modification of the electronic properties of the AZO. SAM decorated AZO electrodes resulted in an increased parallel resistance. SAM layers without a covalently linked fullerene form an insulating barrier, which increases series resistance and deteriorates the device performance significantly. By employing the Fullerene-SAM, the charge transfer from PCBM to AZO is improved, and the series resistance is reduced while the shunt resistance remains high. As a result, the average solar cell efficiency could be improved by approx. 15 % from 2.9 to 3.3 %.

4.5 AZO interface layers with solution processed, transparent silver nanowire electrode

Abstract

In this section, a replacement for the commonly used indium-tin-oxide (ITO) electrode material by a low temperature solution processed silver nanowire/(doped) metal oxide composite is presented. Devices employing silver nanowires (AgNWs)/ buffer layer electrodes with a photoactive layer of poly(3-hexylthiophene) (P3HT) and [6,6]-phenyl-C61 butyric acid methyl ester (PCBM) are showing a comparable performance to the ITO reference cell with fill factors (FF) of over 62 % and a power conversion efficiency of ≈ 2.7 %. Zinc oxide (ZnO) and highly conductive Al doped ZnO (AZO) were used as buffer layer. AgNW devices without a buffer layer have a high open circuit voltage (V_{OC}) but the FF and the short circuit current density (j_{SC}) are substantially lower. Overall it is demonstrated that AgNWs and the low temperature solution process of the buffer layer are an attractive device concept towards an indium free organic solar cell.

Section adapted with permission from Ref. [19]. Copyright 2012, Elsevier.

4.5.1 Solution Processed, Transparent Cathodes

Solution processed electrodes are required for large scale printed organic photovoltaics (OPV) and generally organic electronics [102]. The key requirements are high transparency and conductivity at the same time, but various further properties like stability and low temperature deposition also need to be fulfilled. Graphene sheets [102–105], carbon nanotubes [102, 106–108], transparent conductive oxide nanoparticles and -rods [102, 109], conducting polymers [102, 110–112] and printed metal grids [102, 113] were already proposed as possible alternatives. Due to the low sheet resistance, high transmittance and solution processing, silver nanowires (AgNWs) are considered as highly promising candidates to replace brittle and expensive sputtered indium-tin-oxide (ITO) [114–119]. The AgNW percolation type electrode needs to be filled with a buffer layer to smooth out the roughness, to adjust the work function and provide charge selectivity. N-type metal oxides like (doped) ZnO and TiO_X are a suitable and stable material group that can fulfill these requirements. The application of TiO_X and intrinsic ZnO as buffer layers for AgNWs are already reported [114, 118]. Leem et al. successfully applied TiO_X as buffer layer for an electrode using NWs from Cambrios Technologies Corporation with comparable properties to those NWs used in this study [118]. The typical size of the NWs was a few tens of nanometers in diameter and a few tens of micrometers in length. One further report used intrinsic zinc oxide to fill a network comprising rather thick ($\approx$ 80 nm) and short ($\approx$ 6 μm) AgNWs [114]. Because of the high roughness of this electrode, a very thick active layer (400 nm) was needed to reduce shunts. This is not applicable to most new high performance polymers, as most of them require active layer thicknesses in the range of 70 to 130 nm [120–122]. Consequently, a just 100 nm thick P3HT:PCBM active layer is chosen for the devices in this section. Low temperature, solution processed AgNW/(doped) metal oxide electrodes with excellent functionality are presented. Additionaly, doped and intrinsic zinc oxide buffer layers are compared for this percolation type electrode. In contrast to planar ITO electrodes, the performance of intrinsic and doped zinc oxide is found to be quite comparable when combined with nanowire electrodes.

4.5.2 Organic Solar Cells with AgNW/(Doped) Metal Oxide Cathodes

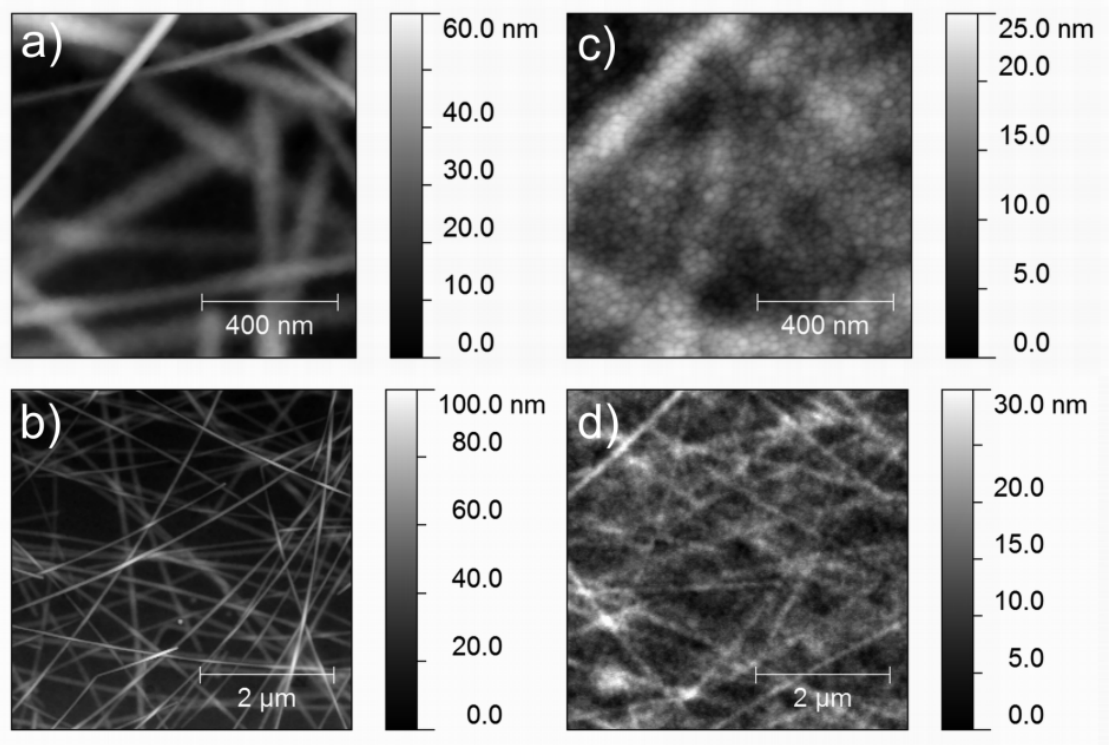

FIGURE 4.17: a) + b) display the surface topography of the AgNW films (RMS: 11-15 nm) and c) + d) show the surface of the AgNWs covered by the AZO layer (RMS 4 nm). Reproduced with permission from Ref. [19]. Copyright 2012, Elsevier.

Figure 4.17 shows the AFM images of the AgNWs and AgNWs covered by the AZO layer. The metal oxide nanoparticles enclose the nanowires. Thereby the AZO film smooths the roughness of the AgNW electrode from RMS of over 10 nm to around 4 nm and generates a rolling-hill morphology without the sharp edges and ridges observed for the pure AgNW film.

The j-V characteristics of the investigated devices are shown in Figure 4.18. Interestingly in contrast to the previous report of Leem et al. [118], we find that the reference device with only AgNWs performed already quite well. The V_{OC} is already comparable to the cells with buffer layer. This is explained by the quite low work function (WF) of 4.4 eV measured by a Kelvin Probe setup (KP Technology LTD, SKP5050). The low WF matches the lowest unoccupied molecular orbital (LUMO) of PCBM well. But as the bare AgNW electrode lacked selectivity and was quite rough, the FF of the device is low at 46.4 %, the j_{SC} 6.52 mA/cm^2 and the PCE 1.65 %. When a ZnO or an AZO buffer layer is used the FF‘s are

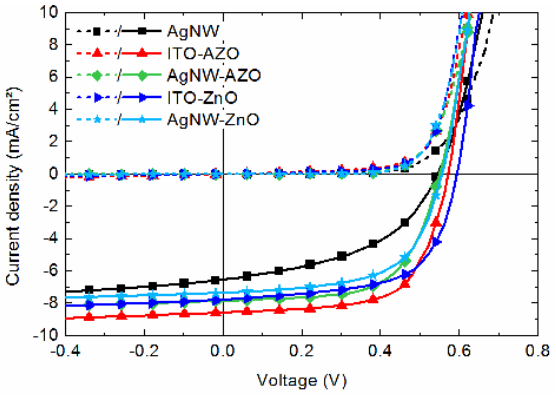

FIGURE 4.18: j-V characteristics of the investigated devices with different cathode configurations (Cathode-P3HT:PCBM-PEDOT:PSS-Ag). Reproduced with permission from Ref. [19]. Copyright 2012, Elsevier.

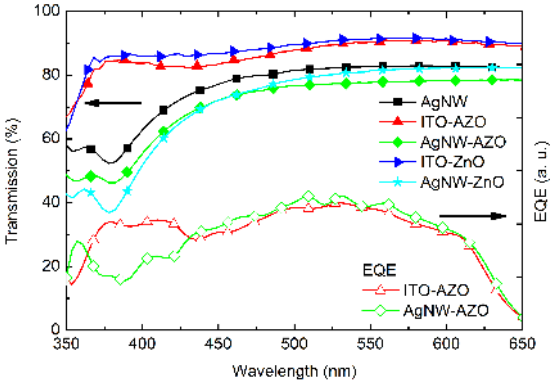

FIGURE 4.19: Transmission of the investigated electrodes (including forward scattering and the glass substrate) as well as the comparison of the EQEs of an ITO-AZO and an AgNW-AZO based device. Reproduced with permission from Ref. [19]. Copyright 2012, Elsevier.

largely increased to 60.2 and 62.3 %. The j_{SC}'s are also enhanced to -7.34 and -7.86 mA/cm^2 leading to PCEs of 2.46 % and 2.68 %. These results are quite comparable to the reference devices on ITO substrates. There are only slightly better values for the FF (≈2 % (absolute)), V_{OC} (≈20-45 mV) and j_{SC} (≈0.4-0.7 mA/cm^2) of the ITO based devices leading to 0.4 to 0.5 % (absolute) higher PCE. Efficient inverted solar cells based on AgNWs are achieved using ZnO and AZO layers. The electrical and optical properties of the metal oxide layers are presented in sections 4.2 for ZnO and 4.3 for LT AZO. Both buffer layer materials achieve comparable and well performing devices. This is attributed to the better charge selectivity and the improved morphology of the electrodes as observed in the AFM pictures. Only quite thin metal oxide layers encapsulate the NWs while the rest of the material filled the network of the electrode. The advantage of AZO over ZnO in the thick film limit on planar ITO electrodes (see sections 4.2 and 4.3)

does not play an important role for this percolation type electrode. Interestingly the AgNW devices need a "burn-in" procedure to show maximum performance. Via applying light reverse bias of e.g. -2 V, shunts that might originate from AgNWs with contact to the top electrode are burned. This burn-in process increases the selectivity (hole blocking) of the electrode. This is more pronounced for the devices without buffer layer than with a metal oxide. A light soaking effect is not existing or so weak that it is not observed in the first measurement for these devices under AM1.5G. The j_SC of the AgNW based devices is observed to be slightly lower than the j_{SC} of the ITO reference devices. To investigate the origin of the difference, the transmission of the electrodes is measured (Figure 4.19). The AgNW electrodes show an approx. 10 % (absolute) lower transmission over the wavelengths above 470 nm than the ITO electrodes. Below 470 nm the gap in the transmission is further increased due to the plasmonic absorption of the AgNWs [117, 123]. This trend is not observed in the EQE measurements as also depicted in Figure 4.19. The EQE's of the ITO-AZO or AgNW-AZO based devices are comparable for all wavelengths above 470 nm. Only below 470 nm, when the plasmonic absorption of the AgNWs sets in, the EQE of the AgNW cell is significantly reduced compared to the ITO cell. Overall, the EQE measurements show that the j_{SC} is 5-7 % lower for the AgNW than for ITO cell (with AZO buffer layer) which is in good agreement with the j-V measurements. This minute difference of the transmission and EQE measurements might be explained by the longer pathway and therefore better absorption of forward scattered light at the AgNW electrode. Other influences might only occur when the light distribution of the whole stack is taken into account. For example backward scattering at the AgNWs of the reflected light from the silver back electrode and improved coupling of the light into the active layer through Ag plasmons as well as other thin film interference effects might be responsible for this observation.

4.5.3 Summary

Efficient inverted solar cells are demonstrated using low temperature, solution processed AgNWs as cathode. Even devices with only 100 nm thick active layer and without n-type buffer layer are functional and already showed high V_{OC}. Application of a ZnO or AZO buffer layer increases dominantly the FF up to over 62 % as well as the j_{SC} of the solar cells. AgNW based devices show comparable performance to the ITO references, although slightly lower values for FF, V_{OC} and

j_{SC} are observed. AZO devices are found to perform negligibly better than the ZnO devices, which is different to the findings for planar ITO electrodes.

4.6 AZO Nanoparticle Layers

Abstract

An AZO nanoparticle (NP) dispersion is introduced in inverted and normal architecture solar cells. In inverted devices, a comparable performance to the precursor formulations of the previous sections 4.2 and 4.3 could be demonstrated. In normal architecture devices, the AZO NP formulation can perform comparable to the reference Ca cathode while the cells with LT AZO precursor ETL didn't show any functionality. The replacement of the low work function metal as cathode for normal architecture solar cells demonstrates a pathway to increase the lifetime of such devices.

4.6.1 Electrical Properties of AZO NP Layers

The previous sections focused on AZO layers from precursor solutions that already fulfilled most of the large area production requirements discussed in section 2.4.4 except the processability at 80 °C and directly on top of organic active materials in normal architecture solar cells wasn‘t demonstrated. A nanoparticle dispersion is the preferred option for these properties. As nanoparticle dispersions already can contain the “final” material and the additional components of the dispersion like the system of solvents and ligands can be chosen according to the application. The investigated AZO nanoparticle (NP) dispersion was obtained from Nanograde. The AZO particles (2% Al concentration in the precursor) were synthesized via flame spray pyrolysis [124]. Afterwards the particles were dispersed in ethanol using a silane as ligand. The electrical characterization of the AZO NP layers that were annealed at only 80 °C for 5 min revealed comparable values to previously investigated LT or HT AZO layers that were treated with considerable higher annealing temperatures of 140 °C, respectively 260 °C (see sections 4.2 and 4.3). The conductivity of the AZO NP‘s is measured to $2 * 10^{-2}$ S/cm which is even slightly higher than LT AZO and HT AZO (10^{-3} S/cm). The work function of the AZO NP layer was measured to be -4.5 eV using Kelvin probe (HT AZO: -4.2 eV, LT AZO: -4.4 eV).

4.6.2 AZO NP Layers in inverted and normal architecture solar cells

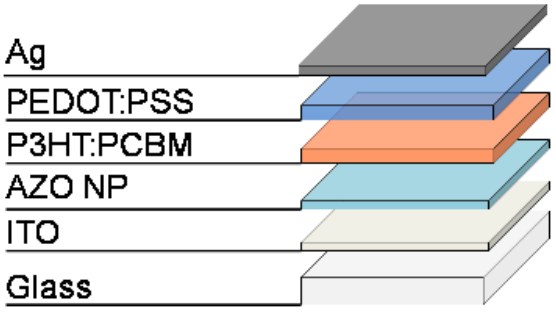

FIGURE 4.20: Layer stack of investigated inverted devices with AZO NP interface layer at 80 °C.

The inverted polymer solar cells were fabricated according to the layer stack shown in Figure 4.20 following the recipe described in Appendix B. The j-V characteristics of typical inverted solar cells with AZO NP ETL are depicted in Figure 4.21. The

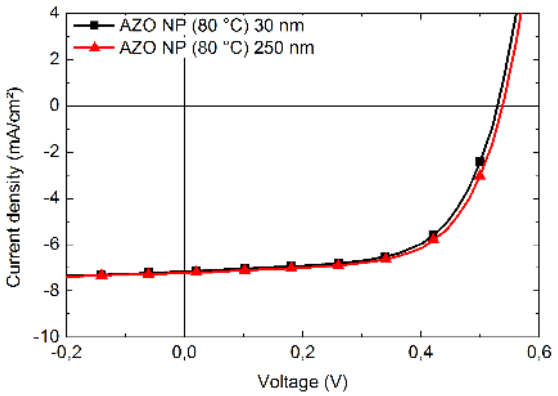

FIGURE 4.21: j-V characteristics of inverted devices showing comparable performance for thin (30 nm) and thick (250 nm) AZO NP ETLs.

data confirms proper functionality of the AZO NP ETLs in thin (30 nm) and also thick (250 nm) films (see Table 4.6). Moreover, the performance of around 2.4-2.5 % PCE is comparable to the previously investigated precursors.

ETL	V_{OC} (mV)	j_{SC} (mA/cm^2)	PCE (%)	FF (%)
Inverted devices				
AZO NP (30 nm)	529	-7.15	2.39	63.1
AZO NP (250 nm)	539	-7.20	2.46	63.4
Normal devices				
Ca	604	-11.19	4.23	62.9
LT AZO	113	-0.07	0.00	24.0
AZO NP	602	-11.59	4.16	59.6

TABLE 4.6: Key parameter set of the best solar cells for each configuration. Inverted devices based on a P3HT:PCBM active layer and measured with solar simulator illumination. The normal devices are based on Si-PCPDTBT:PCBM and illuminated with LED‘s.

Stable polymer solar cells are currently processed in the inverted architecture as the used materials and material combinations are more stable in the inverted layer stack. Most importantly, this architecture avoids the use of unstable, low workfunction metals like Ca, Ba or Al. The most common layer stack for a normal architecture solar cell is ITO \PEDOT:PSS \Active Layer \Al or Ca \Ag. In a further experiment, the application of the previously investigated ETL‘s, namely LT AZO and AZO NP, for a stable top electrode with Ag for solar cells in normal architecture was tested. As the aim is to find a versatile solution for a large number of active layer materials, the annealing temperature for the ETL is chosen to only 80 °C. This ensures minimal impact on the morphology of the active layer and the integrity of organic materials.

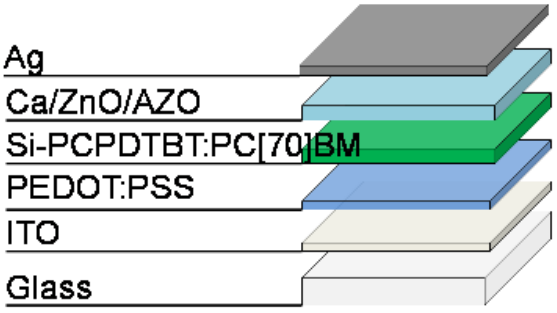

FIGURE 4.22: Layer stack of normal architecture devices with different ETL's.

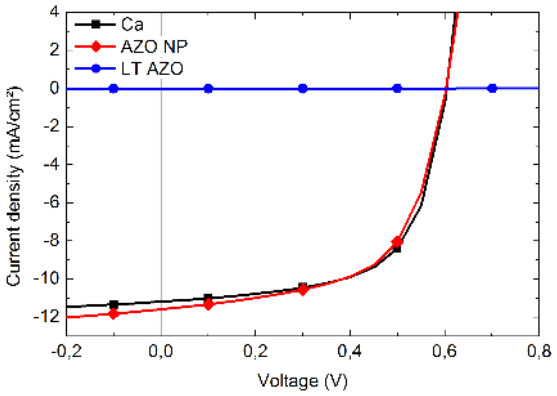

FIGURE 4.23: j-V characteristics of normal architecture devices comparing LT AZO and AZO NP ETL's with Ca. Solar cells with LT AZO don't work at all while cells with AZO NP layer show good performance.

The layer stacks of the investigated normal devices are depicted in figure 4.22 following the recipe described in Appendix E. The j-V characteristics of typical cells with different ETL's are shown in Figure 4.23 and the key parameters are listed in Table 4.6. Solar cells with Ca and AZO NP ETL showed comparable performance. Therefore AZO NP's can replace the very unstable Ca ETL and show a pathway to a longer lifetime of normal architecture cells. Devices with LT AZO didn't show any functionality. The advantage of AZO NP's is that there is no need for high temperatures for the conversion to the final material on the substrate. LT AZO might not work due to the too low annealing temperature for the conversion of the precursor and\or a harmful interaction of the precursor with the active layer [88].

4.6.3 Summary

AZO NP's synthesized using flame spray pyrolysis were introduced in inverted devices with up to 250 nm thickness. The performance of the devices and the

electrical parameters are comparable to the AZO precursors from the previous chapters. The benefit of this interface layer is the low annealing temperature of only 80 °C and the possibility to use this material as replacement to unstable low workfunction metals in devices with normal architecture. This demonstrates a pathway to normal architecture solar cells with longer lifetime.

Chapter 5

Hole Selective Contacts

5.1 Molybdenum Oxide

Abstract

In this section, solution processed molybdenum oxide (MoO_X) layers are incorporated as hole transport layer (HTL) in polymer solar cells (PSCs) and demonstrate the replacement of the commonly employed poly(3,4-ethylene dioxythiophene):(polystyrene sulfonic acid) (PEDOT:PSS). MoO_X is known to have excellent electronic properties and to yield more stable devices compared to PEDOT:PSS. In the view of large scale production of organic photovoltaics, the major limitations of MoO_X so far were the narrow film thickness of a few nanometers to control the serial resistance and the usually employed vacuum process for deposition. Here, fully functional solar cells are presented with up to 65 nm thick MoO_X HTL deposited from a nanoparticle suspension at low temperatures. The PSCs with an active layer comprising a blend of poly(3-hexylthiophene) (P3HT) and [6,6]-phenyl-C_{61} butyric acid methyl ester (PCBM) and a MoO_X HTL show comparable performance to reference devices with a PEDOT:PSS HTL. The best cells with MoO_X reach a fill factor (FF) of 66.7 % and power conversion efficiency (PCE) of 2.92 %. Moreover, MoO_X containing solar cells exhibit an excellent shunt behavior with a parallel resistance of above 100 $k\Omega cm^2$.

Section adapted with permission from Ref. [20]. Copyright 2011, AIP Publishing LLC.

5.1.1 Solution Processed MoO_X for Organic Solar Cells

The working horse material employed as solution processed hole transport layer (HTL) for organic photovoltaics is poly(3,4-ethylene dioxythiophene):(polystyrene sulfonic acid) (PEDOT:PSS). Unfortunately, PEDOT:PSS is identified as a major source of degradation due to its acidic and hygroscopic nature [42, 43, 125–128]. In the standard architecture of a polymer solar cell as depicted in the inset of Figure 5.1, PEDOT:PSS is deposited on the indium-tin-oxide (ITO) electrode. In the presence of humidity, the acidic PEDOT:PSS can etch the ITO electrode, which leads to fast degradation [43, 128]. A frequently employed strategy to solve this issue is to invert the layer sequence. Inverted architectures find PEDOT:PSS sandwiched between the organic semiconductor and a more stable back electrode like e.g. Ag, Au [7, 46]. The polymer-fullerene bulk heterojunction surfaces often have a very low surface energy, which makes it very difficult to coat water-based solutions like conventional PEDOT:PSS formulations on top. For example, a P3HT:PCBM active layer (ratio 1:1) has a surface energy of only ≈25 mN/m (measured using the contact angle measurement setup OCA30 from dataphysics). Furthermore, being committed to the inverse layer sequence in order to achieve stable devices has the disadvantage that the vertical phase separation of the bulk heterojunction is unfavorable to the inverted architecture for many organic photovoltaic materials [56, 129]. A big advantage is the possibility to choose the most suitable architecture for each bulk heterojunction material. Ultimately, employing the normal layer sequence and just replacing PEDOT:PSS through a more stable alternative is a promising approach to solve this stability issue. Materials, which can provide a more stable hole selective contact, are transition metal oxides like MoO_X [20, 56, 60, 63–65], WO_X [61, 71, 72, 130], VO_X [60, 88] and NiO_X [67, 69]. Among these, MoO_X is one of the most interesting materials, because of its non-toxic nature and the very deep lying electronic states [63, 90]. Various groups have shown that comparable device performance can be achieved with evaporated MoO_X as PEDOT:PSS replacement [42, 64]. Additionally, an increased lifetime has been reported for evaporated MoO_X ($eMoO_X$) [42, 56]. Therefore, MoO_X is a promising, more stable alternative material as hole extraction layer replacing PEDOT:PSS in organic solar cells. From the perspective of large scale production, the frequently employed vacuum process for deposition and the limited layer thickness are two major disadvantages of MoO_X [42]. Recently, solution processed

molybdenum oxide layers from precursor solution [64] as well as from a commercially available nanoparticle dispersion [63] were reported. Especially the layers deposited from nanoparticle dispersion appear attractive, since it has been reported, that they offer electronic properties comparable to $eMoO_X$, while at the same time having the advantage of low temperature solution processing (max. 100 °C) and the possibility to deposit comparatively thick layers [63]. The conduction band of this solution processed MoO_X measured in air is found to be 4.9 eV ($eMoO_X$: 5.5 eV), the valence band 8.3 eV ($eMoO_X$: 8.6 eV) and the fermi energy 5.4 eV ($eMoO_X$: 5.7 eV) [63]. In the next section, the incorporation of molybdenum oxide layers processed from this nanoparticle suspension is presented as HTL in PSCs.

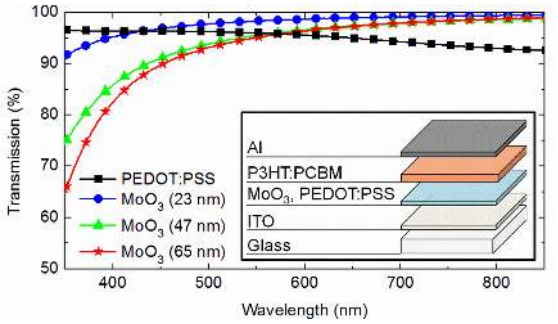

FIGURE 5.1: Transmission of solution processed MoO_X versus the PEDOT:PSS reference. The inset shows the layer stack of the investigated solar cells. Reproduced with permission from Ref. [20]. Copyright 2011, AIP Publishing LLC.

5.1.2 Replacing PEDOT:PSS with Solution Processed MoO_X

The solution processed MoO_X was investigated in three different layer thicknesses ca. 23, 47 and 65 nm. As reference, an approx. 50 nm PEDOT:PSS layer was used. Figure 5.1 shows the transmission of the 4 layers. MoO_X starts absorbing weakly in the blue, which is only significant for the two thicker layers. For the longer wavelengths, the transmission of all 4 layers is comparable and high (> 90 %). The j-V characteristics of the solar cells incorporating the 4 different HTLs are shown in Figure 5.2 and the corresponding key parameters are listed in Table 5.1. The solar cells with MoO_X layers show a trend as a function of film thickness. The fill factor (FF) and the open circuit voltage (V_{OC}) increase slightly with layer

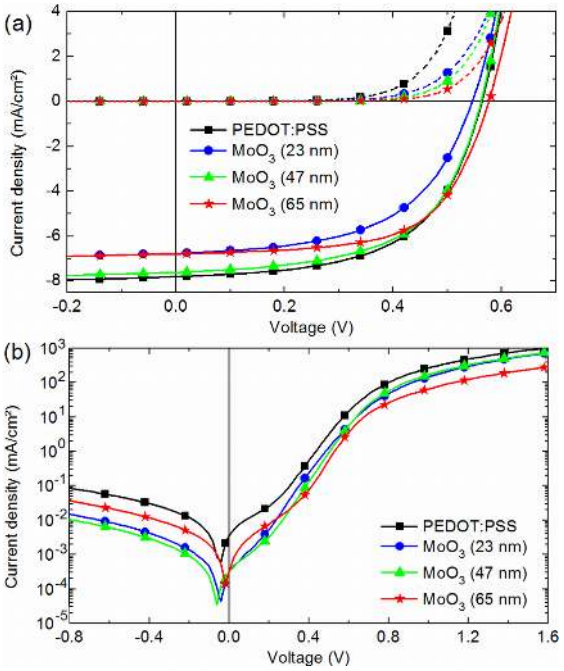

FIGURE 5.2: (a) averaged j-V characteristics of solar cells with solution processed MoO_X versus PEDOT:PSS HELs (b) corresponding logarithmic plot of dark j-V characteristics. Reproduced with permission from Ref. [20]. Copyright 2011, AIP Publishing LLC.

HTL	V_{OC} (mV)	j_{SC} (mA/cm^2)	PCE (%)	FF (%)	R_S Ωcm^2	R_{Shunt} $k\Omega cm^2$	Optical j_{SC} loss* (%)
PEDOT:PSS	563	-7.81	2.53	57.4	0.8	14	-4
$sMoO_X$ (23 nm)	547	-6.76	2.02	54.6	1.1	73	-3
$sMoO_X$ (47 nm)	558	-7.61	2.47	58.0	1.1	107	-9
$sMoO_X$ (65 nm)	579	-6.79	2.42	61.5	3.0	36	-11
Overall best PEDOT:PSS	580	-8.96	3.16	62.2			
Overall best $sMoO_X$ (47 nm)	570	-7.67	2.92	66.7			

TABLE 5.1: Averaged data of at least 5 cells from one substrate of a representative run is displayed. Overall best means best cell from 7 runs. (*Simple optical modeling, only considering single pass absorption in the HEL without taking thin film interference and reflection into account). Adapted with permission from Ref. [20]. Copyright 2011, AIP Publishing LLC.

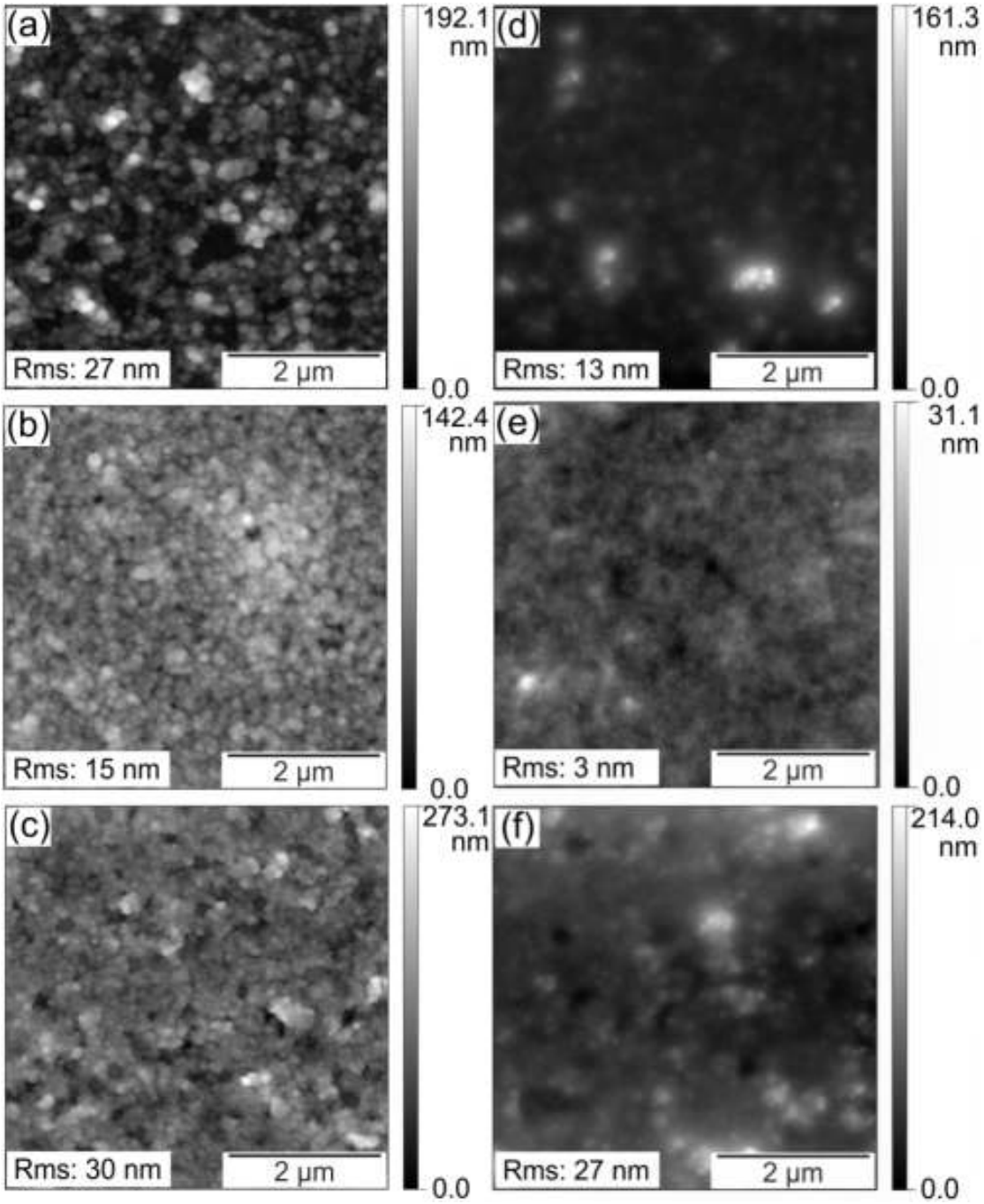

FIGURE 5.3: AFM images of 23 nm ((a), (d)), 47 nm ((b), (e)) and 65 nm ((c), (f)) thick MoO_X films on ITO. For (d) to (f) the layers are covered with a ca. 100 nm thick active layer. Reproduced with permission from Ref. [20]. Copyright 2011, AIP Publishing LLC.

thicknesses from 54.6 % to 58.0 % and 61.5 % for the FF and 547 mV to 558 mV and 579 mV for the V_{OC}. This increase is explained by a decreasing j_0 with thicker MoO_X layers as obtained via simulation of the j-V characteristics using a method described by Waldauf et al. [131]. However, the main impact on the device performance can be attributed to the short circuit current density (j_{SC}). The solar cell with a 47 nm thick MoO_X layer shows a j_{SC} of -7.61 mA/cm^2, while the other two configurations only show -6.76 mA/cm^2 (23 nm) and -6.79 mA/cm^2 (65 nm). Three effects were identified which influence the j_{SC} change as a function of MoO_X layer thicknesses. One contribution arises from optical losses due to absorbed photons in the different HTLs. Table 5.1 gives an overview on the roughly estimated absorption losses in the HTLs. One can see clearly that the differences are too small to explain the j_{SC} trend. Moreover, they also do not correlate qualitatively with the measured data. Next, we analyzed the losses from serial resistance (R_S). The R_S of the devices incorporating the two thinner MoO_X layers is more or less identical at around 1 Ωcm^2 and well within expectations. This is a proof that the contribution of the HEL to the R_S of the device is negligible for these thicknesses. The contribution of the MoO_X layer to the R_S becomes perceptible for the 65 nm film, and it increases to 3 Ωcm^2. Such high R_S can explain a small part of the j_{SC} reduction observed for the thick MoO_X devices. However, in general the series resistance values are far too low to explain the j_{SC} trend. This is particularly true for the thin MoO_X layers. The third and probably most prominent influence on j_{SC} is deduced from the Figures 5.3 a)-f), showing the AFM images of the three MoO_X layers. The layer with the mean thickness of 23 nm (Figure 5.3 a)) shows low coverage and quite significant particle agglomeration leading to a high pinhole density and surface roughness (Rms = 27 nm).The 47 nm film exhibits the best homogeneity among the three layers with the lowest pinhole density and surface roughness (Rms = 15 nm). The thicker film (≈65 nm) again shows higher defect density and surface roughness (Rms = 30 nm). The AFM images of the surfaces of the poly(3-hexylthiophene):[6,6]-phenyl-C61 butyric acid methyl ester (P3HT:PCBM) films covering the MoO_X layers are depicted in Figures 5.3 d)-f). In Figure 5.3 d) and f), it is observed that some agglomerates even poke through the subsequently deposited active layer for the 23 nm and 65 nm thick films. Even though the 47 nm thick film that exhibits the best morphology is not free from defects, P3HT:PCBM film apparently evens out the surface of MoO_X quite efficiently and the Rms value of the P3HT:PCBM surface is low with only 3 nm (see Figure 5.3 e)). With respect to this information,

interface (direct contact of active layer and ITO electrode) and active layer shunts are expected, which reduce the performance of the devices significantly. Counter-intuitively, the shunt resistance (R_{Shunt}) of all the MoO_X containing devices is very high with values of up to 107 $k\Omega cm^2$ (47 nm film). The R_{Shunt} is found to be 73 $k\Omega cm^2$ even for the 23 nm film and still 36 $k\Omega cm^2$ for the 65 nm film. These values are much better than the 14 $k\Omega cm^2$ of the PEDOT:PSS reference device. From that we can conclude that MoO_X based devices do not suffer from shunting. Coming back to the j_{SC} losses, we suggest that the area where MoO_X pokes into or even through the active layer has a reduced photocurrent production. This would coincide qualitatively with the trend for the measured j_{SC}.In summary, we have identified three different loss mechanisms, which can potentially explain the tendency to lesser photocurrent. Surface roughness, incomplete coverage and optical losses may be responsible for this observation. In addition, it is important to note that an increased active layer thickness may reverse this trend. But as most active layer materials only work efficiently with thicknesses around 100 nm, we decided to work with this practicable parameter [29, 132–136]. Overall, the best devices incorporating 47 nm thick MoO_X films show comparable performance to the PEDOT:PSS reference devices (see Table 5.1). According to the experiments until now, the j_{SC} of the devices incorporating MoO_X is found to be generally equal or slightly lower than the current density of the PEDOT:PSS reference devices. In our experiments, we could observe MoO_X devices with FF‘s of up to 66.7 % and PCE‘s of 2.92 %, while the best PEDOT:PSS based device reached 62.2 and 3.16 %.

5.1.3 Summary

A solution processed MoO_X layer is demonstrated as a promising stable alternative to PEDOT:PSS. The MoO_X films can be deposited from nanoparticle solution at low temperatures and reasonable thickness of up to 65 nm without reducing the device performance significantly. Furthermore, devices incorporating MoO_X layers show very high R_{Shunt} values of up to over 100 $k\Omega cm^2$, thus clearly outperforming the PEDOT:PSS reference. The high R_{Shunt} allows for maintaining the high PCE also at low light intensity conditions, which is very important for all indoor and mobile applications [137]. The presented data shows that the excellent material properties of MoO_X are not only available from vacuum evaporation, but also through a solution process and at reasonable layer thickness. Thus, MoO_X is a

highly interesting material for large scale organic photovoltaic production. Here, thick and robust layers are a big advantage when building stable devices with high yield and low shunts. Further investigations on a method to deposit a transition metal oxide layer without an oxygen plasma post treatment, which is a vacuum process, are necessary to fulfill the desired properties for large area production as listed in section 2.4.4. The next step in this direction is presented in the following section with WO_X.

5.2 Tungsten Oxide

Abstract

In this section, a solution processed tungsten oxide (WO_X) is incorporated as hole extraction layer (HEL) in polymer solar cells (PSCs) with active layers comprising either poly(3-hexylthiophene) (P3HT) or poly[(4,4'-bis(2-ethylhexyl)dithieno[3,2-b:2,3-d]silole)-2,6-diyl-alt-(4,7-bis(2-thienyl)-2,1,3-benzothiadiazole)-5,50-diyl] (Si-PCPDTBT) mixed with a fullerene derivative. The WO_X layers are deposited from an alcohol-based, surfactant-free nanoparticle solution. A short, low temperature (80 °C) annealing is sufficient to result in fully functional films without the need for an oxygen plasma treatment which was necessary for MoO_X (section 5.1. This allows the application of the WO_X buffer layer in normal as well as inverted architecture solar cells. Normal architecture devices based on WO_X HELs show comparable performance to the PEDOT:PSS reference devices with slightly better fill factors and open circuit voltages. Very high shunt resistances (>1 $M\Omega cm^2$) and excellent diode rectification underline the charge selectivity of the solution processed WO_X layers. In inverted devices, the results of the development of electron transporting and hole extracting metal oxides are combined. Two solution-processed metal oxides are used at the same time. For the active layers of these devices not only P3HT is used but also a higher performing, commercially available polymer. All the materials used in such a device are intrinsically stable.

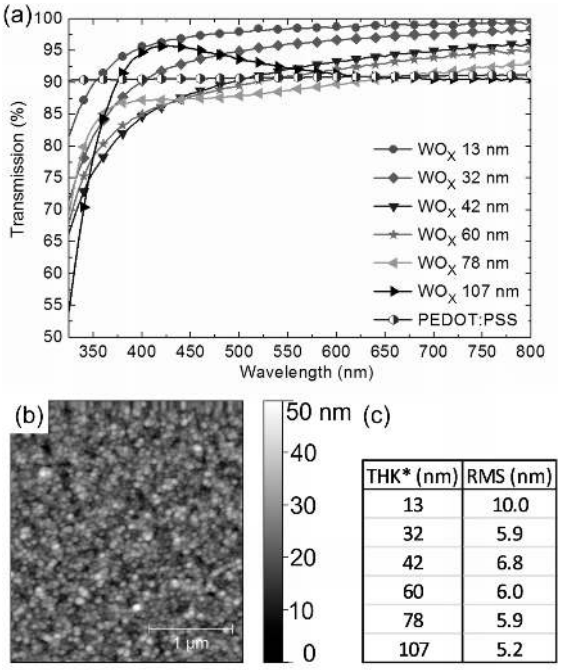

THK* (nm)	RMS (nm)
13	10.0
32	5.9
42	6.8
60	6.0
78	5.9
107	5.2

FIGURE 5.4: (a) Transmission of solution processed WO_X layers (including forward scattering), (b) AFM image of 32 nm thick WO_X film and (c) table of WO_X film thicknesses with corresponding roughness values (*THK=Thickness, RMS=Root mean square). Reproduced with permission from Ref. [21]. Copyright 2012, Wiley VCH.

5.2.1 Why WO_X instead of MoO_X?

All transition metal oxides under discussion can be considered equally promising as all of them are working very comparable in terms of solar cell efficiency, when compared in the same device stack [60]. None of these materials is so rare or expensive that costs or supply arguments would exclude them from the list of candidates. In terms of environmental stability, an argument in favor of WO_X and NiO_X is that they are insoluble in water [138]. Furthermore, considering the classification in the Globally Harmonized System of Classification and Labelling of Chemicals (GHS), WO_X is rated the least harmful material. WO_X (GHS07) and MoO_X (GHS07 and GHS08) are only classified as harmful (Xn), NiO_X (GHS07 and GHS08) is rated toxic (T) and VO_X (GHS07-GHS09) is toxic (T) and dangerous to environment (N) [139]. The low toxicity is an argument in favor of WO_X, but given the very small amounts required for PSC processing, this argument is a minor one. Based on these material specific considerations it is not possible to priorize one specific material due to its intrinsic material properties. Further decision criteria are the deposition and processing conditions as well as the reliability of film formation. PEDOT:PSS is very strong in these aspects. Formation of thin

and homogenous films between 20 and 200 nm with very low surface roughness is straight forward for most PEDOT:PSS formulations. Moreover, PEDOT:PSS is processed from water, requires only low temperature drying, is fully compatible to plastic substrates, and has been reported to give equally good performance in normal as well as inverted architecture PSCs [47]. The key requirements for a HTL material are therefore the low temperature deposition ($<$ 150 °C, target value 80 °C) from solution as well as thick, smooth and robust films with high transmittance and stability. A nanoparticle dispersion is generally favored over a precursor route as precursors can harm the active layer, when applied on top of the organic film [88] (see section 2.4.4). Specifically the low temperature annealing without plasma postprocessing has turned out to be a challenge for many p-type metal oxide layers [20, 63, 67, 69]. In a previous section 5.1, the need of plasma postprocessing for HTLs coated from a MoO_X dispersion from Nanograde (Product No. 3007) is described. For this work, we used a reengineered WO_X solution (Nanograde, Product No. 4035). The transition from MoO_X to WO_X was motivated by the smaller particle size of the WO_X (7 nm instead of 15 nm). Smaller particles have a higher surface energy which helped to stabilize the dispersion in a polar solvent system with no binders. This enables the deposition of pure WO_X films without the need to remove organic residues from the layer that inhibit the electronic functionality of the metal oxide. Removal of the organic residues usually requires high temperatures or (oxygen)plasma posttreatment. The switch from a non-polar xylene based MoO_X dispersion to an alcohol-based, polar solvent system with low boiling point opens the possibility to process WO_X in normal as well as inverted architectures. Moreover, the low surface energy of the alcohol based dispersion does guarantee proper wetting of organic as well as anorganic surfaces. There are only very few studies reporting on solution processed WO_X HTLs for PSCs [71, 72]. Huang et al reported well performing inverted solar cells with nanoparticular WO_X as well as VO_X layers processed from solution [71]. Choi et al demonstrated devices with thin (10 nm) WO_X layers from precursor solution almost matching the performance of PEDOT:PSS in normal architecture devices [72]. The precursor requires no temperature treatment, but a long time for hydrolysis (overnight) for functional films which is an obstacle for the integration in a possible production process. In this study, normal and inverted architecture PSCs with thin active layers (≈100 nm) are investigated that are based on P3HT and Si-PCPDTBT comprising HTLs deposited from WO_X nanoparticle dispersions. Various posttreatments are applied to the WO_X layer and the impact of

postprocessing and HTL thickness on the device performance is studied. Fully functional PSCs with high fill factors of > 65 % are demonstrated for WO_X HTLs with optimized film thickness without the need of plasma postprocessing.

To gain better insight into the material properties of WO_X, the work function (WF) as well as the conductivity of WO_X layers was measured. The WF of a 120 nm WO_X (Annealing: 80 °C/5 min) layer was measured using Kelvin Probe (Kelvin Probe Technologies Inc., SKP5050) in air to 5.35 eV without O_2-Plasma and 5.56 eV after O_2-Plasma. These values are well within expectations as Meyer et al. reported that the WF of WO_X in vacuum is 6.4 eV directly after deposition, but decreases largely (1.0 eV) after air exposure [140]. The lateral conductivity of a WO_X thin film (120 nm) is in the order of 10^{-6} S/cm. As expected, the conductivity of the low temperature, nanoparticulate film is a bit lower than the ones observed for bulk WO_X (10-10^{-4} S/cm), depending on oxygen vacancies) [141]. The transmission of the solution processed WO_X layers was investigated for different film thicknesses ranging from 13 to 107 nm (Figure 5.4 (a)). The transmission is reduced with layer thickness from nearly 100 % (13 nm) to around 90 % (107 nm) in the wavelength regime between 600 and 800 nm. For shorter wavelengths, the transmission is first reduced with increasing layer thickness (from 13 nm to 42 nm), but then starts to rise again (from 60 nm to 107 nm). Thin film interference phenomena were reported by Li et al. for thermally evaporated WO_X layers and may be responsible for this observation [142]. Overall, the transmission of all layers is very high and WO_X is well suited for the application as window layer in solar cells. The morphology of the layers was investigated by AFM images. As an example, the film with 32 nm thickness is shown in Figure 5.4 (b). Figure 5.4 (c) depicts a list of roughness values observed for the different film thicknesses. Only the thinnest, not fully covering film has a roughness value above 10 nm (RMS = root mean square). The other films all have comparable and low roughness between 5 and 7 nm.

5.2.2 WO_X in Organic Solar Cells in Normal Architecture

The layer stacks of the investigated devices and the energy levels of the materials are depicted in Figure 5.5. The j-V characteristics of P3HT:PCBM based solar cells incorporating the WO_X HTLs with different post treatments are shown in Figure 5.6 (a), and the corresponding key parameters are listed in Table 5.2.

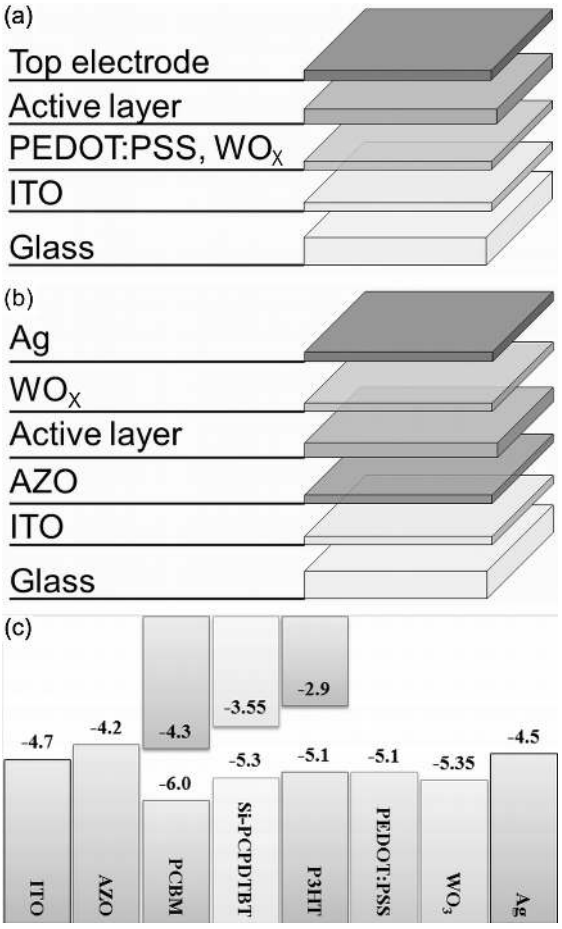

FIGURE 5.5: Layer stacks of the investigated devices in the (a) normal architecture and (b) inverted architecture. (c) Energy levels of the materials investigated in this work. The values for ITO, AZO, PEDOT:PSS and WO_X have been measured using the Kelvin Probe technique in air. The other values are taken from literature. Reproduced with permission from Ref. [21]. Copyright 2012, Wiley VCH.

Three different conversion processes were investigated for 32 nm thick WO_X layers. After deposition, these layers were subject to a posttreatment by either (i) an O_2-Plasma or by a baking step at (ii) 80 °C for 5 min or at (iii) 130 °C for 30 min. The performance of the cells with the PEDOT:PSS reference and the different processed WO_X HTLs is very comparable at around 3 % efficiency for all three postprocessing conditions. The open circuit voltage (V_{OC}) and the fill factor (FF) of the devices containing WO_X (up to 585 mV V_{OC} and 67.3 % FF) is even slightly higher than for the PEDOT:PSS reference (564 mV and 64.7 %). The short circuit current density of the devices ($\approx$7.7 mA/cm^2) that are only baked on the hotplate is slightly less than for the oxygen plasma treated WO_X and the PEDOT:PSS reference ($\approx$8.5 mA/cm^2). But this is very likely due to a statistical variation of the experiment, when accounting all processed device configurations. This result

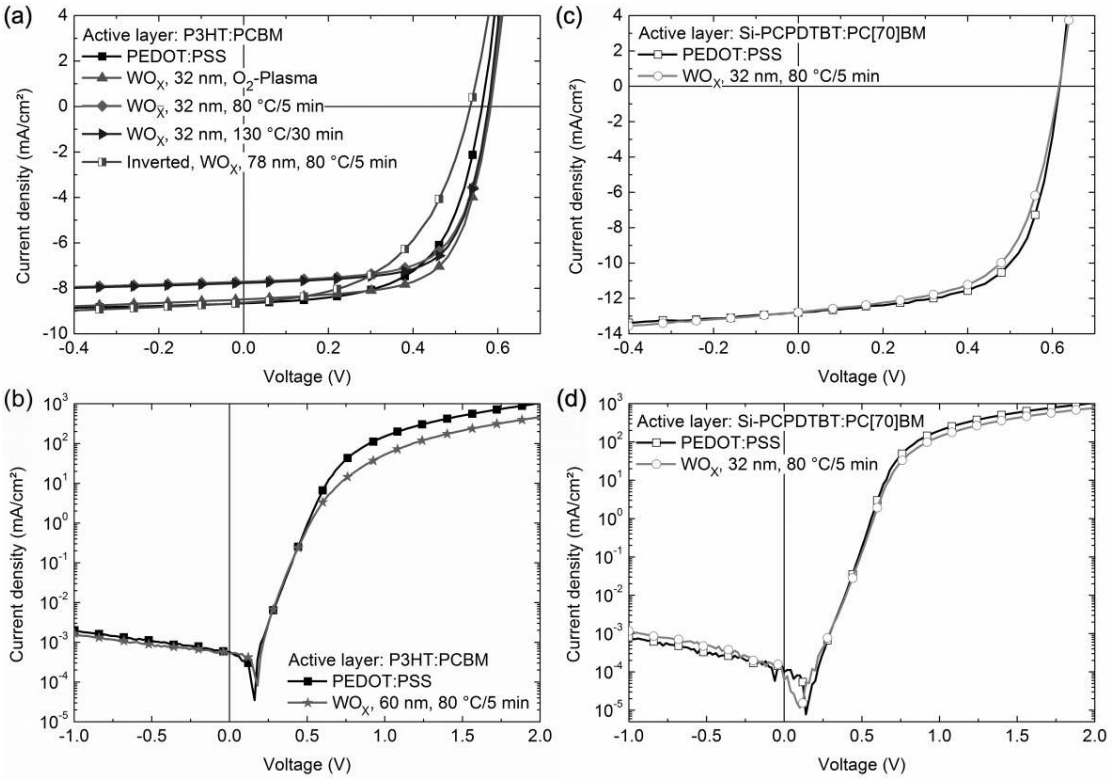

FIGURE 5.6: (a) j-V characteristics of the best P3HT:PCBM based solar cells with different posttreatments of the solution processed WO_X layers versus the PEDOT:PSS reference (b) Comparison of the dark j-V characteristics of the PEDOT:PSS and WO_X solar cell with the best shunt resistance (P3HT:PCBM) (c) j-V characteristics of the best solar cells with Si-PCPDTBT:PC[70]BM active layer comparing PEDOT:PSS and WO_X as well as (d) the corresponding dark j-V characteristics. Reproduced with permission from Ref. [21]. Copyright 2012, Wiley VCH.

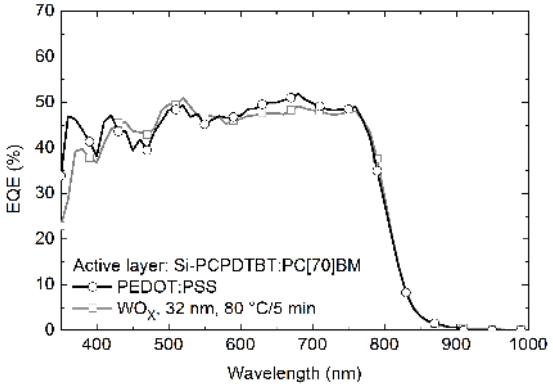

FIGURE 5.7: EQE spectra of a device with solution processed WO_X layer versus the PEDOT:PSS reference. The calculated j_{SC} from this EQE data is 12.9 mA/cm^2 for WO_X and 13.0 mA/cm^2 for PEDOT:PSS. Reproduced with permission from Ref. [21]. Copyright 2012, Wiley VCH.

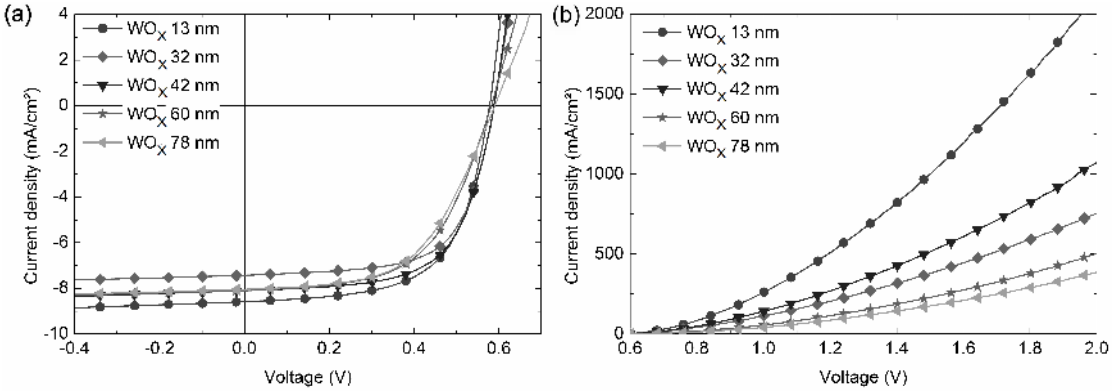

FIGURE 5.8: (a) j-V characteristics of the best P3HT:PCBM devices with increasing WO_X thickness and (b) corresponding injection regime. Reproduced with permission from Ref. [21]. Copyright 2012, Wiley VCH.

HTL	V_{OC} (mV)	j_{SC} (mA/cm^2)	PCE (%)	FF (%)	R_S (Ωcm^2)	R_{Shunt} ($k\Omega cm^2$)
P3HT:PCBM						
PEDOT:PSS	564	-8.7 (-8.6*)	3.2	64.7	0.9	568
WO_X, 32 nm, O_2	585	-8.5	3.2	65.4	1.8	16
WO_X, 32 nm[1]	582	-7.7	2.9	65.4	1.0	127
WO_X, 32 nm[2]	579	-7.8 (-7.8*)	3.0	67.3	0.8	89
WO_X, 13 nm[1]	579	-8.6	3.1	62.3	0.6	12
WO_X, 42 nm[1]	590	-8.1	3.0	63.1	0.9	23
WO_X, 60 nm[1]	584	-8.1	2.7	56.7	1.9	1106
WO_X, 78 nm[1]	593	-8.0	2.6	54.9	2.2	747
WO_X, 107 nm[1]	483	-8.5	1.8	42.8	3.6	3
Inverted P3HT:PCBM						
WO_X, 78 nm[1]	541	-8.5	2.4	51.3	1.1	11
Si-PCPDTBT :PC[70]BM						
PEDOT:PSS	617	-12.7* (-13.0#)	5.0	64.0	1.1	980
WO_X, 32 nm[1]	616	-12.8* (-12.9#)	4.8	60.4	1.4	924

TABLE 5.2: Key parameters of the best devices for each configuration. Illumination was provided by an LED cover. (O_2 means O_2-Plasma, [1] 80 °C/5 min, [2] 130 °C/30 min, *Current density values obtained by illumination with the solar simulator, #Current density values derived from EQE measurement). Adapted with permission from Ref. [21]. Copyright 2012, Wiley VCH.

proves that a low temperature posttreatment at only 80 °C is sufficient for the WO_X buffer layer. To demonstrate the application of the WO_X buffer layer in inverted devices, the curve of an inverted device with 78 nm thick WO_X is also displayed in Figure 3 (a). The cell shows a comparable V_{OC} (541 mV) and j_{SC} (8.5 mA/cm^2) to the normal architecture devices. The FF (51.3 %) is matching the device with the same buffer layer thickness in the normal architecture and leads to a PCE of 2.4 %. The scaling of the performance of inverted devices with WO_X layer thickness is complex and will be published elsewhere [143]. To confirm the functionality of the WO_X HELs for thin non-P3HT based active layers, solar cells comprising the low bandgap polymer Si-PCPDTBT were fabricated. The illuminated j-V characteristics of these devices are displayed in Figure 5.6 (c), the EQE spectra in Figure 5.7 and the key parameters are also listed in Table 5.2. In the direct comparison, PEDOT:PSS and WO_X (annealed at 80 °C/5 min) again perform very comparable at around 5 % efficiency. The j_{SC} values calculated from the EQE data are 12.9 mA/cm^2 for WO_X and 13.0 mA/cm^2 for PEDOT:PSS. Figure 5.6 (b) and (d) display the excellent rectification of the dark j-V characteristics of the best PEDOT:PSS and WO_X based devices with the two investigated active layers. The leakage current at -1 V reverse bias is below 2 $\mu A/cm^2$ for both WO_X and both PEDOT:PSS based cells, demonstrating the excellent selectivity of solution processed WO_X as hole extraction layer. The high shunt resistance (R_{Shunt}) guarantees the high FF and V_{OC} also under low light intensity conditions, which is very important for all indoor and mobile applications [137]. Despite there was no lightsoaking necessary for the devices shown in this report, a small effect was observed for some other batches. This is currently under investigation. Furthermore we studied the dependence of the solar cell performance of P3HT based devices on the HTL film thickness. The WO_X layer thickness was varied between 13 and 107 nm (see Figure 5.7 and Table 5.2). Full performance of the devices in all key parameters FF, j_{SC} and V_{OC} is observed up to a HEL thickness of 42 nm. Above 42 nm, especially the FF is reduced from over 60 to around 55 % (60 and 78 nm) and further reduced to 43.5 % in the thick film limit (107 nm). In parallel, the series resistance (R_S) increases from around 1 to 3.5 Ωcm^2 (measured at 1.9 V bias). For the 60 and the 78 nm films, the performance is only around 10 % lower than for the thinner films. The efficiency of the device based on the thickest WO_X film (107 nm) drops to only 1.89 % PCE as a so called second diode behavior is observed. Here, additional to the FF losses, the V_{OC} is reduced to 514 mV. Thicker WO_X films do cause a higher series resistance which

is well within expectations considering the quite low conductivity of the material. Simulations of the j-V curves using a 1-diode replacement circuit [7], confirm the scaling of the cell performance as a function of the HEL thickness. The behavior is mainly governed by the R_S and shunt resistance (R_{Shunt}). Previous investigations of MoO_X layers with different film thickness showed a significant impact of the HEL morphology found on the j_{SC} [20]. The resulting roughness and number of voids depended strongly on the thickness of the deposited film. Increased roughness led to a reduction of active volume and area for current generation and with that the j_{SC}. This specific trend, the reduction of the j_{SC} upon a HEL increase is not observed (or only weakly expressed) for the nanoparticular WO_X based devices. One reason for this might be the smaller particle size of WO_X, which results in smoother films for all layer thicknesses. This is a clear advantage over the previously reported MoO_X HTLs in section 5.1.2, where the larger nanoparticles caused films with a larger roughness (>=15 nm). Taking all investigated devices into account, besides the statistical variation, the j_{SC} of the WO_X devices can match the j_{SC} of the PEDOT:PSS devices.

5.2.3 WO_X in Organic Solar Cells in Inverted Architecture

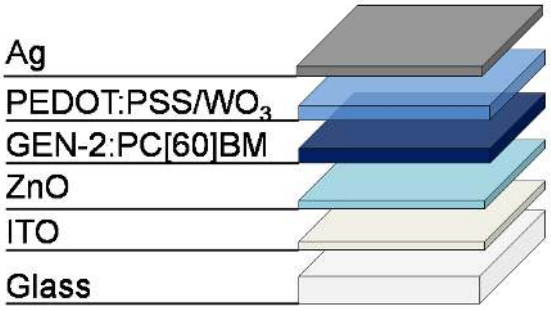

FIGURE 5.9: Layer stack of devices with "pure" metal oxide interfaces.

In this section, an efficient, inverted polymer solar cell with "metal oxide-only" interfaces is presented. Figure 5.9 depicts the used layer stack. A polymer from Merck "GEN-2" is used for a highly efficient active layer together with PCBM. The ETL is formed by ZnO provided by Nanograde (Product No. 5039). As HTL, PEDOT:PSS and WO_X are compared. The structure without PEDOT:PSS contains only intrinsically stable materials with ITO and Ag as electrodes. The j-V characteristics of the well performing inverted solar cells are depicted in Figure 5.10 and the key parameter set is listed in Table 5.3. PEDOT:PSS can be exchanged

to the metal oxide interface without loss in performance for this polymer. While the V_{OC} (760 versus 746 mV) and the j_{SC} (-13.2 versus -12.4 mA/cm^2) is slightly higher for the PEDOT:PSS device, the FF (64.6 versus 59.7 %) of the WO_X cell is better. This results in a similar efficiency close to 6 % for both configurations.

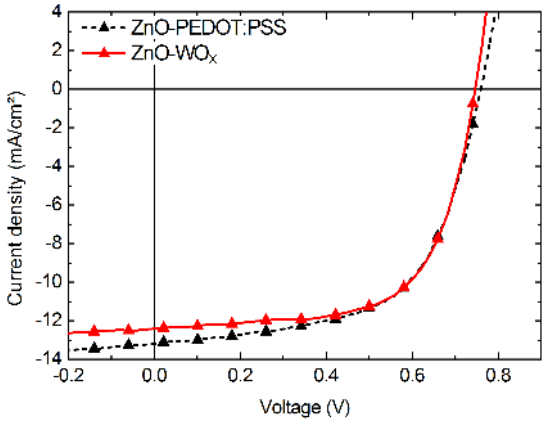

FIGURE 5.10: j-V characteristics of the inverted GEN-2 solar cells with PEDOT:PSS or WO_X HTL.

HTL	V_{OC} (mV)	j_{SC} (mA/cm^2)	PCE (%)	FF (%)
PEDOT:PSS	760	-13.2	5.99	59.7
WO_X	746	-12.4	5.98	64.6

TABLE 5.3: Key parameter set of the best devices for each configuration.

5.2.4 Summary

To conclude, we have demonstrated the application of solution processed WO_X as hole extraction layer in PSCs. The alcohol-based WO_X nanoparticle dispersion fulfills all requirements for the application on plastic substrates and on top of organic active layers. The solution is stabilized without surfactants and an oxygen plasma posttreatment of the HTL is not required. The WO_X layers are fully functional when they are only baked at 80 °C for 5 min. The smooth films formed by the small particles are successfully employed in standard architecture solar cells with thin active layers based on P3HT and Si-PCPDTBT of 100 nm thickness. Devices with WO_X show excellent FFs, V_{OC}s, R_{Shunt}s and PCEs matching or even outrunning the PEDOT:PSS reference. A well performing, "PEDOT-free", "metal oxide-only" inverted polymer solar cell incorporating a commercially available active material is presented in this section as well. The device only contains

materials which are considered intrinsically stable and shows a PCE of ≈ 6 %. The demonstration of such a device enables interesting lifetime studies. Even though the materials should be intrinsically stable, there might be harmful interactions between the materials.

+

Chapter 6

Summary

The world consumes several tens of terawatts (TW) of electricity. If solar energy should have a notable share in the energy generation of the future, the fabrication of solar modules has to be changed from nowadays batch-to-batch processes that operate in the gigawatt regime to a reliable production that allows TW's. Large area roll-to-roll (R2R) printing enables solar cell manufacturing to proceed to TW production.

Organic photovoltaics (OPV) are one of the very promising technologies for printing production. The 10 % hurdle has been overcome after huge progress in increasing the efficiency of OPV over the past years. Now, mainly large scale production and stability issues are in the research focus. Developing the interface layers, situated between active layer and electrodes, of organic solar cells (OSCs) is one of the central parts to solve these challenges. The interface layers are used to maximize efficiency, define the polarity and increase the lifetime of the devices. Apart from their functionality, the interface layers should fulfill the requirements for a large scale printing production. Metal oxides are a very promising option to provide functionality at the required processing conditions.

On the n-type side, this thesis concentrates on zinc oxide (ZnO) and doped zinc oxide as electron transport layer (ETL). The low conductivity (typically $\approx 10^{-6}$ S/cm) of intrinsic ZnO restricts the layer thickness of such an ETL to a few tens of nanometers. A conductivity in the order of 10^{-3} S/cm was derived from electrical simulations as sufficient to increase the interface layer thickness to over 1 μm which would provide all the desired freedom for this parameter. This conductivity can be achieved via doping with Aluminum (Al). In this thesis, Al-doped ZnO (AZO) is introduced as interface layer from precursor solution with comparable performance to ZnO in thin films. AZO maintains the performance also in thick films, while ZnO devices suffer from electrical losses.

Further work was performed to improve the deposition parameters, especially the annealing temperature. The annealing temperature could be improved to a technologically relevant regime of below 150 °C via the engineering of the AZO precursor solution. For the precursor approach, fully functional interface layers with up to 680 nm are experimentally realized to verify the relevance of the simulated results. Thick interface layers may improve the lifetime of the devices and this ETL fulfills the requirements to start lifetime tests.

The surface of the ETL plays a deciding role in the contact formation to the active layer. The surface of an AZO ETL was systematically manipulated using self-assembled monolayers (SAMs) to study its impact on device performance.

The performance of the resulting devices varied between 13 % and 115 % of the unmodified reference device depending on the used SAM. This demonstrates the crucial role of the surface of metal oxide interlayers.
Furthermore, the developed ETL's were tested with a solution processed electrode. Nowadays preferred transparent electrode indium-tin-oxide (ITO) is expensive and brittle. Both make it unattractive for future R2R production on flexible substrates. Solution processed silver nanowires are a candidate to replace ITO. Silver nanowires are solution processable at low temperatures and flexible. The AgNW's form a network with a quite rough morphology that needs to be filled and smoothed by an interface layer. The developed ETL's (ZnO and AZO) are found to be fitting solutions and fully functional devices with 2.7 % efficiency and over 60 % fill factor (FF) are demonstrated. Especially the high FF expresses the excellent electrical functionality of the low temperature, solution processed transparent electrode. This work was an essential step towards fully solution processed and semitransparent devices that have been realized afterwards [1, 2].
Normal architecture solar cells usually employ rather unstable, low work function metals as cathode that limits device lifetime. One approach to make more stable devices is to use metal oxides with high workfunction metals as cathode instead. The previously investigated precursors showed no functionality when applied on top of active layers in the normal architecture. Therefore an AZO nanoparticle (NP) dispersion is employed that shows comparable electrical parameters to the previously used precursors at only 80 °C annealing temperature. The nanoparticle dispersion enables the use of an AZO ETL even on top of previously deposited organic active layers without affecting the morphology or harming the sensitive materials. AZO NP are a replacement with comparable performance to unstable Ca as cathode and can be employed together with stable Ag for normal architecture solar cells.
On the hole transport side, the commonly employed organic poly(3,4-ethylendioxythiophene):poly(styrenesulfonate) (PEDOT:PSS) was found to be a major source of degradation through its hygroscopic and acidic nature. Transition metal oxides are investigated in this thesis as promising candidates with better intrinsic stability. At first, MoO_X deposited from a nanoparticle suspension is introduced as HTL in organic solar cells. The performance is found to match PEDOT:PSS with improved parallel resistance, but an oxygen plasma treatment is necessary for functional films.
The experience gained with MoO_X was applied to develop an improved approach

with WO_X. WO_X was chosen because of the possibility to get very small and mono disperse particles that can be stabilized without organic ligands in an alcoholic solvent system. This enables the deposition smooth films that only need a very low temperature (80 °C) treatment without oxygen plasma for functional films and devices. This WO_X dispersion can even be used in the inverted architecture where the layer is deposited on top of the organic active layer.
Hereby "metal oxide interface only" inverted solar cell with a commercially available active material with high efficiency of around 6 % are made possible. This layer stack contains only electrode materials that are considered as intrinsically stable and that fulfill the previously discussed large area production requirements to a large extent. Promising lifetime studies with devices containing metal oxides that were developed in this thesis, can be started now.

Appendix A

Parameter Set for PC1D

Software available at (last access: October 2013):
http://www.pv.unsw.edu.au/info-about/our-school/products-services/pc1d

Active layer:
Thickness: 0.16 μm
Material modified from program defaults
Fixed electron mobility: $3 * 10^{-3}$ cm^2/Vs
Fixed hole mobility: $8 * 10^{-4}$ cm^2/Vs
Dielectric constant: 3
Band gap: 0.85 eV
Intrinsic conc. at 300 K: $1 * 10^{12}$
Refractive index: 1.8
Absorption coeff. from internal model
No free carrier absorption
P-type background doping: $1 * 10^{15}$ cm^{-3}
No front diffusion
No rear diffusion
Bulk recombination: $\tau_n = \tau_p = 5$ μs
No Front-surface recombination
No Rear-surface recombination

Electron extraction layer:
Thickness: variable, 0.03-1.25 μm

Material modified from program defaults
Fixed electron mobility: $1 * 10^{-3}$ cm^2/Vs
Fixed hole mobility: $1 * 10^{-3}$ cm^2/Vs
Dielectric constant: 25
Band gap: 1.3 eV
Intrinsic conc. at 300 K: $1.1 * 10^8$ cm^{-3}
Refractive index: 2
Absorption coeff. from internal model
No free carrier absorption
N-type background doping: variable, $6.25 * 10^{16}$ - $6.25 * 10^{18}$ cm^{-3}
No front diffusion
No rear diffusion
Bulk recombination: $\tau_n = 1 * 10^6$ μs, $\tau_p = 5$ μs
No Front-surface recombination
No Rear-surface recombination
Excitation:
Excitation mode: Transient, 200 timesteps
Temperature: 300 K
Base circuit: Sweep from 0 to 0.562 V, Start at t = 0
Collector circuit: Zero
Primary light source enabled
Constant intensity: 0.1 W cm^{-2}
Spectrum AM 1.5 G
Secondary light source disabled

Appendix B

Processing of Inverted Architecture Solar Cells

The inverted photovoltaic devices were processed and characterized in ambient atmosphere. Structured ITO coated glass substrates (either ≈12 Ω/square from Osram or ≈5 Ω/square from Weidner Glas) were subsequently cleaned in acetone and isopropyl alcohol for 10 minutes each. After drying, the substrates were coated with the solution for the electron transport layer. P3HT purchased from Merck and technical grade PCBM from Solenne were separately dissolved in chlorobenzene at a concentration of 2 wt% and stirred for at least 1 hr at 60 °C before being blended in a volume ratio of 1:1. The blended solution was stirred for at least another hour at 60 °C before use. The ca. 100 nm thick active layer was deposited via doctor blading. PEDOT:PSS (Clevios PH) from H.C. Starck was diluted in isopropyl alcohol (1:3 or 1:5 volume ratio) with Dynol 604 from AirProducts as surfactant (0.2 or 0.13 volume percent) before deposition via doctor blading. The whole stack was annealed at 140 °C for 10 min on a hot plate before evaporation of a 100 nm thick Ag layer to form the top electrode. The active area of the investigated devices was 10.4 mm^2.

Variations from this recipe:
Sections 4.2 and 4.4: The PEDOT:PSS formulation with isopropyl alcohol (1:3 volume ratio) and 0.2 volume percent Dynol 604. The substrates were from Osram.
Section 4.3: The PEDOT:PSS formulation with isopropyl alcohol (1:5 volume ratio) and 0.13 volume percent Dynol 604. The substrates were from Weidner Glas.

Section 4.4: The AZO formulation was annealed at 150 °C for 10 min on Osram substrates. Afterwards the samples with SAM were immersed in the isopropyl alcohol solution containing the SAM forming molecules with a concentration of ca. 0.01 mmol/l for 24 h.
Section 4.5: Osram substrates were used for reference devices. AgNW based devices were processed on float glass slides. The AgNW film was deposited via doctor blading and annealed at 140 °C for 15 min resulting into a low sheet resistance of $\approx 7\ \Omega$/square. The following layers were processed identically on ITO and AgNWs. The PEDOT:PSS formulation with isopropyl alcohol (1:5 volume ratio) and 0.13 volume percent Dynol 604. The whole stack was annealed for 5 min before and 5 min after evaporation of the top electrode at 140 °C on a hotplate.
Section 4.6: The substrates were from Weidner Glas. The AZO NP layer was deposited in a thickness of 30 or 250 nm from an ethanol dispersion (5 wt%) via doctor blading. Afterwards the layers were annealed at 80 °C for 5 min. The PEDOT:PSS formulation with isopropyl alcohol (1:5 volume ratio) and 0.13 volume percent Dynol 604.

Appendix C

Synthesis Routes for ZnO and AZO

Synthesis of ZnO nanoparticle suspensions adapted from [144]: The ZnO nanoparticles were prepared in methanol via hydroxylation of zinc acetate dihydrate ($Zn(Ac)_2$*$2H_2O$) by potassium hydroxide (KOH) and afterwards dissolved in acetone at a concentration of 2 wt%.

Synthesis of Al doped ZnO precursors for sections 4.2 (AZO 1), 4.3 (AZO 1-3) and 4.5 (AZO 3) (Routes partly adopted from [58, 145]: (Doping ratio: 1 at% Al) AZO 1 (AlAc, MEA) (Film annealed at 260 °C $\widehat{=}$ HT AZO): $Zn(Ac)_2$*$2H_2O$ (2.20 g), $Al(Ac)_2OH$ (0.016 g) and Ethanolamin (MEA, 0.16 mL) were mixed in 100 mL of ethanol. The mixture was heated to 80 °C for 2.5 h. The result is a clear solution. AZO 2 (AlAc, filtered): $Zn(Ac)_2$*$2H_2O$ (2.20 g) and $Al(Ac)_2OH$ (0.016 g) were mixed in 100 mL of ethanol. The mixture was heated to 80 °C for 2.5 h and afterwards filtered through a 0.45 micron filter to remove insoluble material. AZO 3 (AlNi, filtered) (Film annealed at 140 °C $\widehat{=}$ LT AZO): $Zn(Ac)_2$*$2H_2O$ (2.17 g) and $Al(NO_3)_3$*$9H_2O$ (0.038 g) were mixed in 100 mL of ethanol. The mixture was heated to 80 °C for 2.5 h (3 h for 4.5) and afterwards filtered through a 0.45 micron filter to remove insoluble material.

Synthesis of Al doped ZnO for section 4.4: $Zn(OAc)_2$*$2H_2O$ (20 g), $Al(OH)(OAc)_2$ (0.3 g) and Zonyl FSO-100 (0.6g) were mixed in demineralized water (200 mL). The mixture was stirred for 2 hours and filtered through a 0.45 micron filter to remove insoluble material.

Appendix D

Transistor Fabrication and Measurement Data

The substrate was a heavily p-doped silicon wafer with 100 nm thermally grown silicon dioxide. The gate electrodes were formed by evaporating 30 nm aluminum through a shadow mask. Then a solution of poly(4-vinylphenol) (PVP) and the cross-linking agent poly(melamine-co-formaldehyde) in propylene glycol monomethyl ether acetate was spincoated at 4000 rpm for 20 s, dried for 1 min at 100 °C and subsequently cross-linked at 200 °C for 6 min The resulting PVP dielectric layer had a thickness of about 190 nm and a capacitance of 90 nF/cm^2. Then the different AZO layers were doctor bladed and annealed before the evaporation of 30 nm thick Aluminum layers as top electrodes forming channels with a length of 40 μm and width of 600 μm.

The transistor devices were fabricated and evaluated in the Organic Materials and Devices (OMD) group at the Institute of Polymer Materials (Friedrich-Alexander-University Erlangen-Nuremberg).

Adapted with permission from Ref. [16] with permission from The Royal Society of Chemistry.

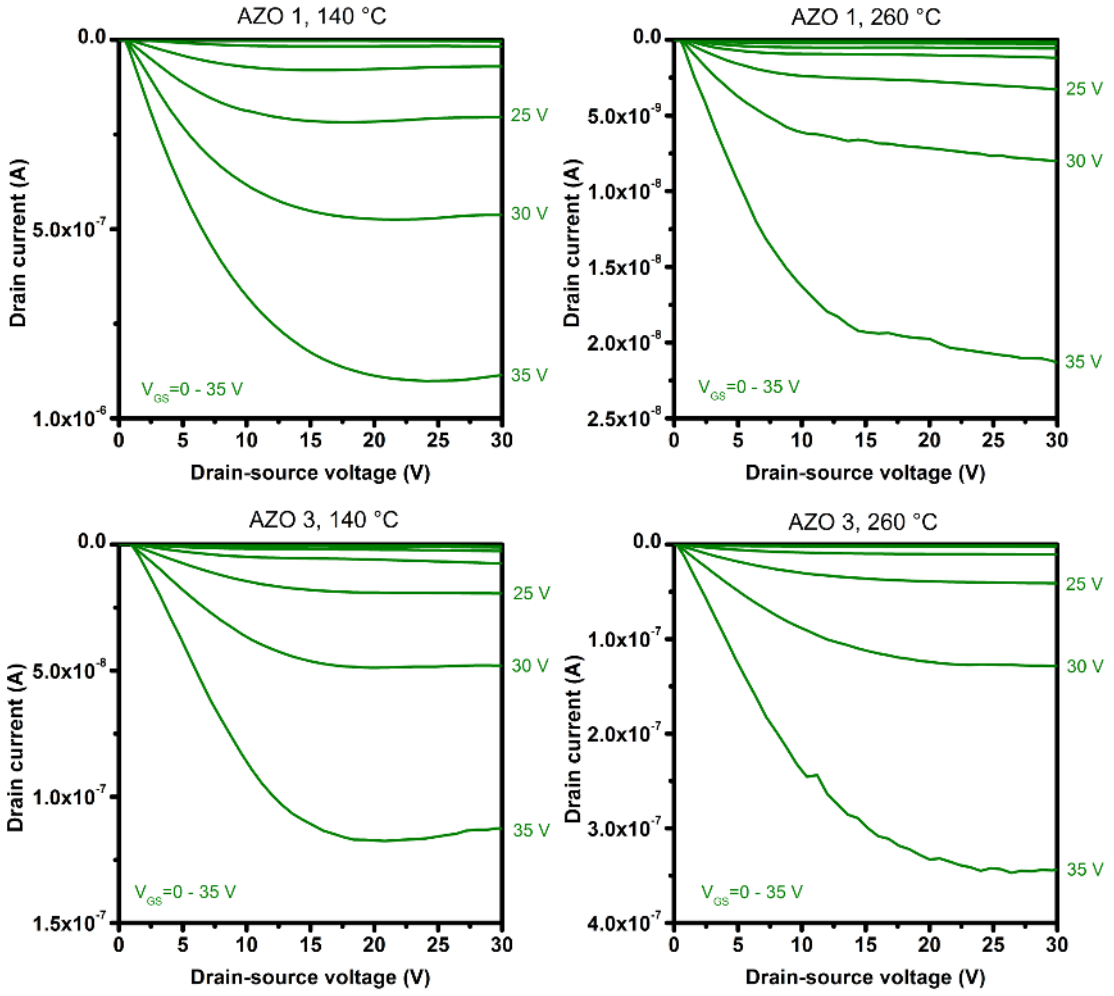

FIGURE D.1: Output characteristics of the transistor devices with different AZO layers. Reproduced from Ref. [16] with permission from The Royal Society of Chemistry.

Appendix E

Processing of Normal Architecture Solar Cells with Varying Cathode Configurations

The photovoltaic devices were processed in ambient atmosphere. Pre-structured ITO coated glass substrates (obtained from Weidner Glas ($\approx$ 5 Ω/square) were subsequently cleaned in acetone and isopropyl alcohol for 10 minutes each. After drying, the substrates were coated with an approx. 50 nm thick PEDOT:PSS (VP Al 4083, H.C. Starck) layer which was then annealed at 120 °C for 5 min. An approx. 100 nm thick active layer was doctor bladed from a dichlorobenzene solution of Si-PCPDTBT (Konarka) and PCBM ([6,6]-phenyl-C_{61} butyric acid methyl ester, Solenne) in weight ratio 1:1.5. The blend was not fully optimized in terms of fullerene ratio and film thickness. The solar cells were finalized by the evaporation of a Ca (20 nm)/Ag (100 nm) top electrode as reference. For the devices with LT AZO (70 nm) or AZO NP (50 nm) layer, the devices were annealed at 80 °C for 5 min after deposition of the solutions. For these devices, Ag (100 nm) was deposited as top electrode as well. The active area was 10.4 mm^2.

Appendix F

Processing of Solar Cells with Varying Hole Transport Layer

The photovoltaic devices were processed in ambient atmosphere. Pre-structured ITO coated glass substrates (obtained from Osram) were subsequently cleaned in acetone and isopropyl alcohol for 10 minutes each. After drying, the substrates were coated with the HTL.

For section 5.1: The MoO_X suspension(5 wt%, surfactant stabilized by an undisclosed block copolymer in xylene), obtained from Nanograde (Product No. 3007), was deposited via doctor blading. The further treatment followed a method described by Meyer et al. [63]. Different thicknesses from 23 to 65 nm were obtained by varying the solid content (0.5 to 2 wt%) of the dispersion by dilution with xylene. Afterwards, the samples were baked on a hot plate at 100 °C for 10 min. To remove the dispersing agent,the samples were treated in an O_2-plasma (2 min, 200 W, 0.2 mbar, gas flow 3 sccm). For reference devices, PEDOT:PSS (VP Al 4083) from H.C. Starck was diluted in isopropyl alcohol (1:3 volume ratio) before deposition of an approx. 50 nm thick layer. P3HT purchased from Merck and technical grade PCBM from Solenne were dissolved separately in chlorobenzene at a concentration of 2 wt% and stirred for at least 1 hr at 60 °C before being blended in a volume ratio of 1:1. The blended solution was stirred for at least another hour at 60 °C before use. The approx. 100 nm thick active layer was deposited via doctor blading. The whole stack was annealed on a hot plate at 140 °C for 5 min after evaporation of a 100 nm thick Al layer to form the top electrode. The active area of the investigated devices was 10.4 mm^2.

For section 5.2: The WO_X suspension (2.5 wt%, surfactant-free, alcohol-based, XRD: 7nm particle size, crystal structure: triclinic) was obtained from Nanograde Llc. (Product No. 4035). Before use, the solution was centrifuged for 4 min at 1000 rpm to sediment secondary particles. The dispersion was deposited via doctor blading without dilution except for the 13 nm film (1:1 with EtOH). The samples were posttreated in an O_2-plasma (2 min, 200 W, 0.2 mbar, gas flow 3 sccm) or annealed on a hotplate at different temperatures: 80 °C for 5 min or 130 °C for 30 min. An approx. 50 nm thick PEDOT:PSS (VP Al 4083, H.C. Starck) layer was deposited for reference devices.

- Normal architecture P3HT devices: An approx. 100 nm thick active layer was doctor bladed from a chlorobenzene solution of P3HT (Merck) and technical grade PCBM ([6,6]-phenyl-C_{61} butyric acid methyl ester, Solenne) in weight ratio 1:1. The whole stack was annealed on a hot plate at 140 °C for 5 min after evaporation of a 100 nm thick Al layer to form the top electrode.

- Si-PCPDTBT devices: An approx. 100 nm thick active layer was doctor bladed from a dichlorobenzene solution of Si-PCPDTBT (Konarka) and PC[70]BM ([6,6]-phenyl-C_{71} butyric acid methyl ester, Solenne) in weight ratio 1:1.5. The blend was not fully optimized in terms of fullerene ratio and film thickness. The solar cells were finalized by the evaporation of a Ca (20 nm)/Ag (100 nm) top electrode.

- Inverted architecture P3HT devices: Al doped ZnO was synthesized as described as AZO 1 in C and doctor bladed as electron extraction layer on the cleaned ITO substrates. An approx. 100 nm thick active layer was doctor bladed from a chlorobenzene solution of P3HT (Merck) and technical grade PCBM ([6,6]-phenyl-C_{61} butyric acid methyl ester, Solenne) in weight ratio 1:1. Before the deposition of a 78 nm thick WO_X layer, the samples were annealed at 140 °C for 5 min. The whole stack was annealed on a hot plate at 80 °C for 5 min before evaporation of a 100 nm thick Ag layer to form the top electrode.

The active area of all solar cells was 10.4 mm^2. Current density-voltage (j-V) characteristics were measured with a source measurement unit from BoTest. Illumination was provided by an OrielSol 1A Solarsimulator with AM1.5G spectra at 0.1 W/cm^2 (in air) or an LED cover (BoTest) with 12 ultra-bright, white LEDs (in

nitrogen, glovebox). When using the LED cover, the light intensity of the LEDs was adjusted, that the cells showed the same current under the solar simulator and the LED cover. Six solar cells were processed for each configuration.

Bibliography

[1] J. Krantz, T. Stubhan, M. Richter, S. Spallek, I. Litzov, G. J. Matt, E. Spiecker, and C. J. Brabec. *Adv. Funct. Mater.*, 23(13):1711–1717, 2013.

[2] F. Guo, X. Zhu, K. Forberich, J. Krantz, T. Stubhan, M. Salinas, M. Halik, S. Spallek, B. Butz, E. Spiecker, T. Ameri, N. Li, P. Kubis, D. M. Guldi, G. J. Matt, and C. J. Brabec. *Adv. Energy Mater.*, 3(8):1062–1067, 2013.

[3] Pieter Tans. http://www.esrl.noaa.gov/gmd/ccgg/trends/, October 2013.

[4] Nick Greeves. http://chemtube3d.com/orbitalsethene.htm, October 2013.

[5] W. Cai, X. Gong, and Y. Cao. *Sol. Energy Mater. Sol. Cells*, 94(2):114–127, 2010.

[6] H. Hoppe and N. S. Sariciftci. Polymer Solar Cells. In Seth R. Marder and Kwang-Sup Lee, editors, *Photoresponsive Polym. II SE - 121*, volume 214 of *Advances in Polymer Science*, pages 1–86. Springer Berlin Heidelberg, 2008.

[7] C. Waldauf, M. C. Scharber, P. Schilinsky, J. A. Hauch, and C. J. Brabec. *J. Appl. Phys.*, 99(10):104503–104506, 2006.

[8] C. J. Brabec, A. Cravino, D. Meissner, N. S. Sariciftci, T. Fromherz, M. T. Rispens, L. Sanchez, and J. C. Hummelen. *Adv. Funct. Mater.*, 11(5):374–380, 2001.

[9] S. Braun, W. R. Salaneck, and M. Fahlman. *Adv. Mater.*, 21(14-15):1450–1472, 2009.

[10] W. Tress, K. Leo, and M. Riede. *Adv. Funct. Mater.*, 21(11):2140–2149, 2011.

[11] S.K.M Jönsson, J. Birgerson, X. Crispin, G. Greczynski, W. Osikowicz, A. W. Denier van der Gon, W. R. Salaneck, and M. Fahlman. *Synth. Met.*, 139(1):1–10, 2003.

[12] J. Huang, G. Li, and Y. Yang. *Adv. Mater.*, 20(3):415–419, 2008.

[13] T. Ameri, J. Min, N. Li, F. Machui, D. Baran, M. Forster, K. J. Schottler, D. Dolfen, U. Scherf, and C. J. Brabec. *Adv. Energy Mater.*, 2(10):1198–1202, 2012.

[14] M. Rydzek, M. Reidinger, M. Arduini-Schuster, and J. Manara. *Thin Solid Films*, 520(12):4114–4118, 2012.

[15] F. C Krebs. *Sol. Energy Mater. Sol. Cells*, 93(4):394–412, 2009.

[16] T. Stubhan, I. Litzov, N. Li, M. Salinas, M. Steidl, G. Sauer, K. Forberich, G. J. Matt, M. Halik, and C. J. Brabec. *J. Mater. Chem. A*, 1(19):6004, 2013.

[17] T. Stubhan, H. Oh, L. Pinna, J. Krantz, I. Litzov, and C. J. Brabec. *Org. Electron.*, 12(9):1539–1543, 2011.

[18] T. Stubhan, M. Salinas, A. Ebel, F. C. Krebs, A. Hirsch, M. Halik, and C. J. Brabec. *Adv. Energy Mater.*, 2:532–535, 2012.

[19] T. Stubhan, J. Krantz, N. Li, F. Guo, I. Litzov, M. Steidl, M. Richter, G. J. Matt, and C. J. Brabec. *Sol. Energy Mater. Sol. Cells*, 107:248–251, 2012.

[20] T. Stubhan, T. Ameri, M. Salinas, J. Krantz, F. Machui, M. Halik, and C. J. Brabec. *Appl. Phys. Lett.*, 98(25):253308, 2011.

[21] T. Stubhan, N. Li, N. A. Luechinger, S. C. Halim, G. J. Matt, and C. J. Brabec. *Adv. Energy Mater.*, 2(12):1433–1438, 2012.

[22] R. Nave. http://hyperphysics.phy-astr.gsu.edu/hbase/tables/elabund.html, October, 2013.

[23] NREL. http://www.nrel.gov/ncpv/images/efficiency_chart.jpg, October, 2013.

[24] Wolfgang Brütting and W. Rieß. *Phys. J.*, 5(7):33, 2008.

[25] Alan J Heeger. *Rev. Mod. Phys.*, 73:681–700, 2001.

[26] I.G. Hill, A. Kahn, Z. G. Soos, and R. A. Pascal, Jr. *Chem. Phys. Lett.*, 327(3-4):181–188, 2000.

[27] Carsten Deibel and Vladimir Dyakonov. *Phys. J.*, 7(5):51, 2008.

[28] C. W. Tang. *Appl. Phys. Lett.*, 48(2):183, 1986.

[29] S. H. Park, A. Roy, S. Beaupre, S. Cho, N. Coates, J. S. Moon, D. Moses, M. Leclerc, K. Lee, and A. J. Heeger. *Nat Phot.*, 3(5):297–302, 2009.

[30] T. Ameri, G. Dennler, C. Lungenschmied, and C. J. Brabec. *Energy Environ. Sci.*, 2(4):347–363, 2009.

[31] P. Würfel. *Physics of Solar Cells*. Wiley-VCH Verlag GmbH, Weinheim, Germany, 2005.

[32] R. Steim, F. R. Kogler, and C. J. Brabec. *J. Mater. Chem.*, 20(13):2499, 2010.

[33] V. D. Mihailetchi, P. W. M. Blom, J. C. Hummelen, and M. T. Rispens. *J. Appl. Phys.*, 94(10):6849, 2003.

[34] M. C. Scharber, D. Mühlbacher, M. Koppe, P. Denk, C. Waldauf, A. J. Heeger, and C. J. Brabec. *Adv. Mater.*, 18(6):789–794, 2006.

[35] K. Walzer, B. Maennig, M. Pfeiffer, and K. Leo. *Chem. Rev.*, 107(4):1233–71, 2007.

[36] H. Ma, H.-L. Yip, F. Huang, and A. K.-Y. Jen. *Adv. Funct. Mater.*, 20(9):1371–1388, 2010.

[37] H.-L. Yip and A. K.-Y. Jen. *Energy Environ. Sci.*, 5(3):5994, 2012.

[38] S. E. Shaheen, C. J. Brabec, N. S. Sariciftci, F. Padinger, T. Fromherz, and J. C. Hummelen. *Appl. Phys. Lett.*, 78(6):841, 2001.

[39] Y. Cao, G. Yu, C. Zhang, R. Menon, and A. J. Heeger. *Synth. Met.*, 87(2):171–174, 1997.

[40] S. A. Carter, M. Angelopoulos, S. Karg, P. J. Brock, and J. C. Scott. *Appl. Phys. Lett.*, 70(16):2067, 1997.

[41] J. C. Carter, I. Grizzi, S. K. Heeks, D. J. Lacey, S. G. Latham, P. G. May, O. Ruiz de los Panos, K. Pichler, C. R. Towns, and H. F. Wittmann. *Appl. Phys. Lett.*, 71(1):34, 1997.

[42] E. Voroshazi, B. Verreet, A. Buri, R. T. Müller, D. Di Nuzzo, and P. Heremans. *Org. Electron.*, 12(5):736–744, 2011.

[43] M. Jø rgensen, K. Norrman, and F. C. Krebs. *Sol. Energy Mater. Sol. Cells*, 92(7):686–714, 2008.

[44] F. Zhang, M. Ceder, and O. Inganäs. *Adv. Mater.*, 19(14):1835–1838, 2007.

[45] S.-I. Na, T.-S. Kim, S.-H. Oh, J. Kim, S.-S. Kim, and D.-Y. Kim. *Appl. Phys. Lett.*, 97(22):223305, 2010.

[46] R. Steim, S. A. Choulis, P. Schilinsky, and C. J. Brabec. *Appl. Phys. Lett.*, 92(9):093303, 2008.

[47] C. Waldauf, M. Morana, P. Denk, P. Schilinsky, K. Coakley, S. A. Choulis, and C. J. Brabec. *Appl. Phys. Lett.*, 89(23):233517, 2006.

[48] H. Oh, J. Krantz, I. Litzov, T. Stubhan, L. Pinna, and C. J. Brabec. *Sol. Energy Mater. Sol. Cells*, 95(8):2194–2199, 2011.

[49] J. Y. Kim, S. H. Kim, H.-H. Lee, K. Lee, W. Ma, X. Gong, and A. J. Heeger. *Adv. Mater.*, 18(5):572–576, 2006.

[50] K.-L. Ou, D. Tadytin, K. X. Steirer, D. Placencia, M. Nguyen, P. Lee, and N. R. Armstrong. *J. Mater. Chem. A*, 1(23):6794, 2013.

[51] H.-L. Yip, S. K. Hau, N. S. Baek, A. K.-Y. Jen, J. Zou, and K. O'Malley. *Appl. Phys. Lett.*, 92(25):253301–253303, 2008.

[52] H.-L. Yip, S. K. Hau, N. S. Baek, H. Ma, and A. K.-Y. Jen. *Adv. Mater.*, 20(12):2376–2382, 2008.

[53] J. Gilot, M. M. Wienk, and R. A. J. Janssen. *Appl. Phys. Lett.*, 90(14):143512–143513, 2007.

[54] S. K. Hau, H.-L. Yip, H. Ma, and A. K.-Y. Jen. *Appl. Phys. Lett.*, 93(23):233304, 2008.

[55] M. S. White, D. C. Olson, S. E. Shaheen, N. Kopidakis, and D. S. Ginley. *Appl. Phys. Lett.*, 89(14):143513–143517, 2006.

[56] Y. Sun, J. H. Seo, C. J. Takacs, J. Seifter, and A. J. Heeger. *Adv. Mater.*, 23(14):1679–83, 2011.

[57] A. Puetz, T. Stubhan, M. Reinhard, O. Loesch, E. Hammarberg, S. Wolf, C. Feldmann, H. Kalt, A. Colsmann, and U. Lemmer. *Sol. Energy Mater. Sol. Cells*, 95(2):579–585, 2011.

[58] R. Sø ndergaard, M. Helgesen, M. Jø rgensen, and F. C. Krebs. *Adv. Energy Mater.*, 1(1):68–71, 2011.

[59] A. K. K. Kyaw, X. W. Sun, C. Y. Jiang, G. Q. Lo, D. W. Zhao, and D. L. Kwong. *Appl. Phys. Lett.*, 93(22):83305, 2008.

[60] V. Shrotriya, G. Li, Y. Yao, C.-W. Chu, and Y. Yang. *Appl. Phys. Lett.*, 88(7):073508, 2006.

[61] C. Tao, S. Ruan, G. Xie, X. Kong, L. Shen, F. Meng, C. Liu, X. Zhang, W. Dong, and W. Chen. *Appl. Phys. Lett.*, 94(4):43311–43313, 2009.

[62] M. Y. Chan, C. S. Lee, S. L. Lai, M. K. Fung, F. L. Wong, H. Y. Sun, K. M. Lau, and S. T. Lee. *J. Appl. Phys.*, 100(9):094506, 2006.

[63] J. Meyer, R. Khalandovsky, P. Görrn, and A. Kahn. *Adv. Mater.*, 23(1):70–73, 2011.

[64] F. Liu, S. Shao, X. Guo, Y. Zhao, and Z. Xie. *Sol. Energy Mater. Sol. Cells*, 94(5):842–845, 2010.

[65] C. Girotto, E. Voroshazi, D. Cheyns, P. Heremans, and B. P. Rand. *ACS Appl. Mater. Interfaces*, 3(9):3244–7, 2011.

[66] K. Zilberberg, H. Gharbi, A. Behrendt, S. Trost, and T. Riedl. *ACS Appl. Mater. Interfaces*, 4(3):1164–8, 2012.

[67] K. X. Steirer, P. F. Ndione, N. E. Widjonarko, M. T. Lloyd, J. Meyer, E. L. Ratcliff, A. Kahn, N. R. Armstrong, C. J. Curtis, D. S. Ginley, J. J. Berry, and D. C. Olson. *Adv. Energy Mater.*, 1(5):813–820, 2011.

[68] E. L. Ratcliff, J. Meyer, K. X. Steirer, A. Garcia, J. J. Berry, D. S. Ginley, D. C. Olson, A. Kahn, and N. R. Armstrong. *Chem. Mater.*, 23(22):4988–5000, 2011.

[69] K. X. Steirer, J. P. Chesin, N. E. Widjonarko, J. J. Berry, A. Miedaner, D. S. Ginley, and D. C. Olson. *Org. Electron.*, 11(8):1414–1418, 2010.

[70] N. Espinosa, H. F. Dam, D. M. Tanenbaum, J. W. Andreasen, M. Jø rgensen, and F. C. Krebs. *Materials*, 4(12):169–182, 2011.

[71] J.-S Huang, C.-Y. Chou, and C.-F. Lin. *IEEE Electron Device Lett.*, 31(4):332–334, 2010.

[72] H. Choi, B. S. Kim, M. J. Ko, D.-K. Lee, H. Kim, S. H. Kim, and K. Kim. *Org. Electron.*, 13(6):959–968, 2012.

[73] Z. Tan, L. Li, C. Cui, Y. Ding, Q. Xu, S. Li, D. Qian, and Y. Li. *J. Phys. Chem. C*, 116(35):18626–18632, 2012.

[74] S. K. Hau, Y.-J. Cheng, H.-L. Yip, Y. Zhang, H. Ma, and A. K.-Y. Jen. *ACS Appl. Mater. Interfaces*, 2(7):1892–1902, 2010.

[75] H. Choi, J. S. Park, E. Jeong, G.-H. Kim, B. R. Lee, S. O. Kim, M. H. Song, H. Y. Woo, and J. Y. Kim. *Adv. Mater.*, 23(24):2759–63, 2011.

[76] J. Min, H. Zhang, T. Stubhan, Y. N. Luponosov, M. Kraft, S. A. Ponomarenko, T. Ameri, U. Scherf, and C. J. Brabec. *J. Mater. Chem. A*, 1(37):11306, 2013.

[77] J. H. Seo, E. B. Namdas, A. Gutacker, A. J. Heeger, and G. C. Bazan. *Adv. Funct. Mater.*, 21(19):3667–3672, 2011.

[78] J. H. Seo, A. Gutacker, B. Walker, S. Cho, A. Garcia, R. Yang, T.-Q. Nguyen, A. J. Heeger, and G. C. Bazan. *J. Am. Chem. Soc.*, 131(51):18220–1, 2009.

[79] J. H. Seo, A. Gutacker, Y. Sun, H. Wu, F. Huang, Y. Cao, U. Scherf, A. J. Heeger, and G. C. Bazan. *J. Am. Chem. Soc.*, 133(22):8416–9, 2011.

[80] Y. Zhou, C. Fuentes-Hernandez, J. Shim, J. Meyer, A. J. Giordano, H. Li, P. Winget, T. Papadopoulos, H. Cheun, J. Kim, M. Fenoll, A. Dindar, W. Haske, E. Najafabadi, T. M. Khan, H. Sojoudi, S. Barlow, S. Graham, J.-L. Bredas, S. R. Marder, A. Kahn, and B. Kippelen. *Science*, 336(6079):327–332, 2012.

[81] L. P. Lu, D. Kabra, and R. H. Friend. *Adv. Funct. Mater.*, 22(19):4165–4171, 2012.

[82] A. Savva, F. Petraki, P. Elefteriou, L. Sygellou, M. Voigt, M. Giannouli, S. Kennou, J. Nelson, D. D. C. Bradley, C. J. Brabec, and S. A. Choulis. *Adv. Energy Mater.*, 3(3):391–398, 2013.

[83] S. Khodabakhsh, B. M. Sanderson, J. Nelson, and T. S. Jones. *Adv. Funct. Mater.*, 16(1):95–100, 2006.

[84] J. You, L. Dou, K. Yoshimura, T. Kato, K. Ohya, T. Moriarty, K. Emery, C.-C. Chen, J. Gao, G. Li, and Y. Yang. *Nat. Commun.*, 4:1446, 2013.

[85] Y. Liang and L. Yu. *Acc. Chem. Res.*, 43(9):1227–36, 2010.

[86] T.-Y. Chu, J. Lu, S. Beaupré, Y. Zhang, J.-R. Pouliot, S. Wakim, J. Zhou, M. Leclerc, Z. Li, J. Ding, and Y. Tao. *J. Am. Chem. Soc.*, 133(12):4250–3, 2011.

[87] J. Peet, L. Wen, P. Byrne, S. Rodman, K. Forberich, Y. Shao, N. Drolet, R. Gaudiana, G. Dennler, and D. Waller. *Appl. Phys. Lett.*, 98(4):043301, 2011.

[88] K. Zilberberg, S. Trost, J. Meyer, A. Kahn, A. Behrendt, D. Lützenkirchen-Hecht, R. Frahm, and T. Riedl. *Adv. Funct. Mater.*, 21(24):4776–4783, 2011.

[89] U. Ozgur, Ya. I. Alivov, C. Liu, A. Teke, M. A. Reshchikov, S. Dogan, V. Avrutin, S.-J. Cho, and H. Morkoc. *J. Appl. Phys.*, 98(4):41103–41301, 2005.

[90] M. Kröger, S. Hamwi, J. Meyer, T. Riedl, W. Kowalsky, and A. Kahn. *Appl. Phys. Lett.*, 95(12):123301, 2009.

[91] H. Zheng, J. Z. Ou, M. S. Strano, R. B. Kaner, A. Mitchell, and K. Kalantar-zadeh. *Adv. Funct. Mater.*, 21(12):2175–2196, 2011.

[92] PC1D, http://www.pv.unsw.edu.au/info-about/our-school/products-services/pc1d, October 2013.

[93] M. Vafaee and M. S. Ghamsari. *Mater. Lett.*, 61(14-15):3265–3268, 2007.

[94] S. H. Yoon, D. Liu, D. Shen, M. Park, and D.-J. Kim. *J. Mater. Sci.*, 43(18):6177–6181, 2008.

[95] N. Li, T. Stubhan, D. Baran, J. Min, H. Wang, T. Ameri, and C. J. Brabec. *Adv. Energy Mater.*, 3(3):301–307, 2013.

[96] S. Sista, M.-H. Park, Z. Hong, Y. Wu, J. Hou, W. L. Kwan, G. Li, and Y. Yang. *Adv. Mater.*, 22(3):380–383, 2010.

[97] P. J. Hotchkiss, M. Malicki, A. J. Giordano, N. R. Armstrong, and S. R. Marder. *J. Mater. Chem.*, 21(9):3107, 2011.

[98] M. Novak, A. Ebel, T. Meyer-Friedrichsen, A. Jedaa, B. F. Vieweg, G. Yang, K. Voitchovsky, F. Stellacci, E. Spiecker, A. Hirsch, and M. Halik. *Nano Lett.*, 11(1):156–9, 2011.

[99] M. Burkhardt, A. Jedaa, M. Novak, A. Ebel, K. Voïtchovsky, F. Stellacci, A. Hirsch, and M. Halik. *Adv. Mater.*, 22(23):2525–8, 2010.

[100] A. Wagenpfahl, D. Rauh, M. Binder, C. Deibel, and V. Dyakonov. *Phys. Rev. B*, 82(11):115306, 2010.

[101] M. Voigt, M. Klaumunzer, A. Ebel, F. Werner, G. Yang, R. Marczak, E. Spiecker, D. M. Guldi, A. Hirsch, and W. Peukert. *J. Phys. Chem. C*, 115(13):5561–5565, 2011.

[102] D. S. Hecht, L. Hu, and G. Irvin. *Adv. Mater.*, 23(13):1482–513, 2011.

[103] K. S. Kim, Y. Zhao, H. Jang, S. Y. Lee, J. M. Kim, K. S. Kim, J.-H. Ahn, P. Kim, J.-Y. Choi, and B. H. Hong. *Nature*, 457(7230):706–10, 2009.

[104] G. Eda and M. Chhowalla. *Adv. Mater.*, 22(22):2392–415, 2010.

[105] P. H. Wöbkenberg, G. Eda, D.-S. Leem, J. C. de Mello, D. D. C. Bradley, M. Chhowalla, and T. D. Anthopoulos. *Adv. Mater.*, 23(13):1558–62, 2011.

[106] E. M. Doherty, S. De, P. E. Lyons, A. Shmeliov, P. N. Nirmalraj, V. Scardaci, J. Joimel, W. J. Blau, J. J. Boland, and J. N. Coleman. *Carbon N. Y.*, 47(10):2466–2473, 2009.

[107] D.-S. Leem, S. Kim, J. W. Kim, J. I. Sohn, A. Edwards, J. Huang, X. Wang, J.-J. Kim, D. D. C. Bradley, and J. C. DeMello. *Small*, 6(22):2530–2534, 2010.

[108] S. Kim, J. Yim, X. Wang, D. D. C. Bradley, S. Lee, and J. C. DeMello. *Adv. Funct. Mater.*, 20(14):2310–2316, 2010.

[109] S. Yodyingyong, Q. Zhang, K. Park, C. S. Dandeneau, X. Zhou, D. Triampo, and G. Cao. *Appl. Phys. Lett.*, 96(7):073115, 2010.

[110] P. A. Levermore, R. Jin, X. Wang, L. Chen, D. D. C. Bradley, and J. C. de Mello. *J. Mater. Chem.*, 18(37):4414, 2008.

[111] J. Huang, X. Wang, a. J. DeMello, J. C. DeMello, and D. D. C. Bradley. *J. Mater. Chem.*, 17(33):3551, 2007.

[112] S.-I. Na, S.-S. Kim, J. Jo, and D.-Y. Kim. *Adv. Mater.*, 20(21):4061–4067, 2008.

[113] J. Perelaer, B.-J. deGans, and U.S. Schubert. *Adv. Mater.*, 18(16):2101–2104, 2006.

[114] F. S. F. Morgenstern, D. Kabra, S. Massip, T. J. K. Brenner, P. E. Lyons, J. N. Coleman, and R. H. Friend. *Appl. Phys. Lett.*, 99(18):183307, 2011.

[115] R. Zhu, C.-H. Chung, K. Cha, W. Yang, Y. B. Zheng, H. Zhou, T.-B. Song, C.-C. Chen, P. S. Weiss, G. Li, and Y. Yang. *ACS Nano*, 2011.

[116] Z. Yu, L. Li, Q. Zhang, W. Hu, and Q. Pei. *Adv. Mater.*, 23(38):4453–7, 2011.

[117] M. Krantz, J.and Richter, S. Spallek, E. Spiecker, and C. J. Brabec. *Adv. Funct. Mater.*, 21(24):4784–4787, 2011.

[118] D.-S. Leem, A. Edwards, M. Faist, J. Nelson, D. D. C. Bradley, and J. C. de Mello. *Adv. Mater.*, 23(38):4371–5, 2011.

[119] T. Tokuno, M. Nogi, M. Karakawa, J. Jiu, T. T. Nge, Y. Aso, and K. Suganuma. *Nano Res.*, 4(12):1215–1222, 2011.

[120] H.-Y. Chen, J. Hou, S. Zhang, Y. Liang, G. Yang, Y. Yang, L. Yu, Y. Wu, and G. Li. *Nat Phot.*, 3(11):649–653, 2009.

[121] C. E. Small, S. Chen, J. Subbiah, C. M. Amb, S. Tsang, T. Lai, J. R. Reynolds, and F. So. *Nat. Photonics*, 6(2):115–120, 2011.

[122] J. Subbiah, C. M. Amb, I. Irfan, Y. Gao, J. R. Reynolds, and F. So. *ACS Appl. Mater. Interfaces*, 4(2):866–70, 2012.

[123] A. Graff, D. Wagner, H. Ditlbacher, and U. Kreibig. *Eur. Phys. J. D*, 34(1-3):263–269, 2005.

[124] A. Purwanto, W.-N. Wang, and K Okuyama. Flame Spray Pyrolysis. In Nasser Ashgriz, editor, *Handb. At. Sprays SE - 39*, pages 869–879. Springer US, 2011.

[125] K. Kawano, R. Pacios, D. Poplavskyy, J. Nelson, D. D. C. Bradley, and J. R. Durrant. *Sol. Energy Mater. Sol. Cells*, 90(20):3520–3530, 2006.

[126] M. P. de Jong, L. J. van IJzendoorn, and M. J. A. de Voigt. *Appl. Phys. Lett.*, 77(14):2255–2257, 2000.

[127] H. Yan, P. Lee, N. R. Armstrong, A. Graham, G. A. Evmenenko, P. Dutta, and T. J. Marks. *J. Am. Chem. Soc.*, 127(9):3172–83, 2005.

[128] K. Norrman, S. A. Gevorgyan, and F. C. Krebs. *ACS Appl. Mater. Interfaces*, 1(1):102–112, 2009.

[129] W. Cai, X. Gong, and Y. Cao. *Sol. Energy Mater. Sol. Cells*, 94(2):114–127, 2010.

[130] M. S. Ryu and J. Jang. *Sol. Energy Mater. Sol. Cells*, 95(10):2893–2896, 2011.

[131] C. Waldauf, P. Schilinsky, J. Hauch, and C. J. Brabec. *Thin Solid Films*, 451-452:503–507, 2004.

[132] J. Hou, H.-Y. Chen, S. Zhang, G. Li, and Y. Yang. *J. Am. Chem. Soc.*, 130(48):16144–16145, 2008.

[133] Y. Zou, A. Najari, P. Berrouard, S. Beaupr, B. Rda Aich, Y. Tao, and M. Leclerc. *J. Am. Chem. Soc.*, 132(15):5330–5331, 2010.

[134] Y. Liang, Z. Xu, J. Xia, S.-T. Tsai, Y. Wu, G. Li, C. Ray, and L. Yu. *Adv. Mater.*, 22(20):E135–E138, 2010.

[135] J. Peet, J. Y. Kim, N. E. Coates, W. L. Ma, D. Moses, A. J. Heeger, and G. C. Bazan. *Nat Mater*, 6(7):497–500, 2007.

[136] E. Wang, L. Wang, L. Lan, C. Luo, W. Zhuang, J. Peng, and Y. Cao. *Appl. Phys. Lett.*, 92(3):33303–33307, 2008.

[137] R. Steim, T. Ameri, P. Schilinsky, C. Waldauf, G. Dennler, M. Scharber, and C. J. Brabec. *Sol. Energy Mater. Sol. Cells*, 95(12):3256–3261, 2011.

[138] S. Budavari. *The Merck Index - An Encyclopedia of Chemicals, Drugs, and Biologicals.* 1996.

[139] Sigma Aldrich, http://www.sigmaaldrich.com/, October, 2013.

[140] J. Meyer, S. Hamwi, T. Bulow, H.-H. Johannes, T. Riedl, and W. Kowalsky. *Appl. Phys. Lett.*, 91(11):113506, 2007.

[141] V. Makarov and M. Tronteljb. *J. Eur. Ceram. Soc.*, 2219(95):791–794, 1996.

[142] F. Li, S. Ruan, Y. Xu, F. Meng, J. Wang, W. Chen, and L. Shen. *Sol. Energy Mater. Sol. Cells*, 95(3):877–880, 2011.

[143] N. Li, T. Stubhan, N. A. Luechinger, S. C. Halim, G. J. Matt, T. Ameri, and C. J. Brabec. *Org. Electron.*, 13(11):2479–2484, 2012.

[144] O. Harnack, C. Pacholski, H. Weller, A. Yasuda, and J. M. Wessels. *Nano Lett.*, 3(8):1097–1101, 2003.

[145] M. J. Alam and D. C. Cameron. *J. Vac. Sci. Technol. A Vacuum, Surfaces, Film.*, 19(4):1642, 2001.